# 5 Electron, lattice and spin dynamics on Gd(0001)/W(110)

This chapter is devoted to the static and dynamic nonlinear magneto-optical investigations of the ferromagnetic Gd(0001) system. In the first part the static properties of the system as measured by MSHG are detailed while the following part of the chapter is focused on the time-resolved response of the system. Here the ultrafast magnetization dynamics encountered at the Gd surface and the newly discovered phenomenon of the coupled coherent phonon-magnon mode, that evolves in the THz frequency range, are described.

## 5.1 MSHG on Gd(0001): static properties

Before starting any time-resolved investigation of a certain system, a detailed knowledge about its characteristic static properties is necessary. With respect to the MSHG investigation of ferromagnetic materials, precise information regarding the polarization dependence of the SHG yield and magnetic contrast as well as the behavior of the relative phase between the even $E_{even}(2\omega)$ and odd $E_{odd}(2\omega)$ second-harmonic fields are required. For instance, information about the origin of the SHG response can be retrieved from polarization dependent measurements of the SHG intensity since this quantity is sensitive to *e.g.* surface symmetry, electronic structure and photon energy [129]. Furthermore, the magnetic contrast defined in eq. 3.34 renders the magnitude of the magnetic effects in the investigated region. The relative phase $\phi$ between the SHG fields is of utmost importance since together with the SHG intensity (see formula 3.33) provides a complete characterization of the nonlinear response of the system. By investigating the photon energy dependence of the phase $\phi$, the presence of a resonance in the SHG process can be detected [102, 106].

In this section, the quantities characterizing the MSHG static response (*i.e.* polarization dependence, magnetic contrast and the relative phase $\phi$ ), measured on the Gd(0001) surface under an UHV environment, will be presented.
As a reminder, all the measurements presented in this chapter are performed *in situ* on 20 nm Gd films grown epitaxially on W(110) substrate, in a transversal configuration at 45° incidence angle with the external magnetic field oriented along magnetization easy axis, unless otherwise specified.

### 5.1.1 Polarization dependent MSHG response

The first issue one should investigate when working with magneto-optics on ferromagnetic materials is the existence of a measurable magnetic contrast. This can be done simply by measuring the magnetization hysteresis that renders not only the value of the magnetic

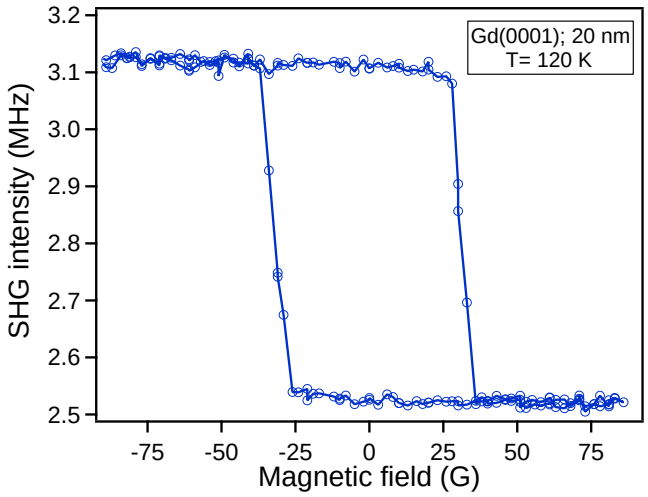


**Figure 5.1:** MSHG hysteresis loop measured in a p-T (p-polarized input, total SHG output *i.e.* no analyzer ) geometry from a 20 nm Gd(0001) film at a temperature of 120 K. Note the hysteresis square shape that indicates that the measurement is performed along magnetization easy axis.

contrast but also information about magnetic anisotropy, magnetization orientation [114] etc. In the case of Gd(0001) thin films, we have been primarily interested in the orientation of the magnetization easy axis direction. At the employed film thickness of 20 nm, the easy axis of magnetization is oriented in the film plane [130] its direction being determined by the higher demagnetization energy compared to the magnetocrystalline anisotropy. As a check for this, a MSHG hysteresis has been recorded by measuring the SH intensity as a function of the applied external magnetic field. The MSHG measurements has been performed in the transversal geometry (with magnetic field in the plane of the sample) in a p-T polarization configuration (p-polarized input fundamental, SHG detected without preferential polarization). One such example is presented in figure 5.1 where one notices immediately the square shape of the hysteresis that indicates a measurement performed along easy axis, and thus the orientation of magnetization in the plane of the sample.

After this initial check one can proceed to the polarization dependent MSHG measurements. One information that can be retrieved from polarization dependence of the SHG response is related with the structural symmetry of the surface. Also valuable information can be deduced regarding the optimal experimental geometry in terms of SHG intensity, magnetic contrast, the particular susceptibility $\chi^{(2)}$ tensor elements involved etc. In the following the polarization dependent MSHG measurements performed on Gd(0001) are presented.

The measurements described in this section are performed at a sample temperature of 110 K (well below Curie point of 293 K) and with the femtosecond laser running in the oscillator regime (see chapter 4). Although in this regime the laser pulse energy is smaller (≈6 nJ) than for the cavity dumper (≈42 nJ) due to the higher repetition rate (76 MHz) the produced SHG yield is higher[1]. This is required since one can encounter certain polarization configurations where the SHG efficiency is low and therefore a higher incident power is useful. For the polarization measurements a combination of $\lambda/2$ plate and a Glan-Thompson polarizer is used, that are inserted in the fundamental (laser beam

[1] According to eq. 3.24 the SHG signal scales proportionally with the incident laser pulse energy and inverse proportionally with the laser beam diameter and pulse duration.

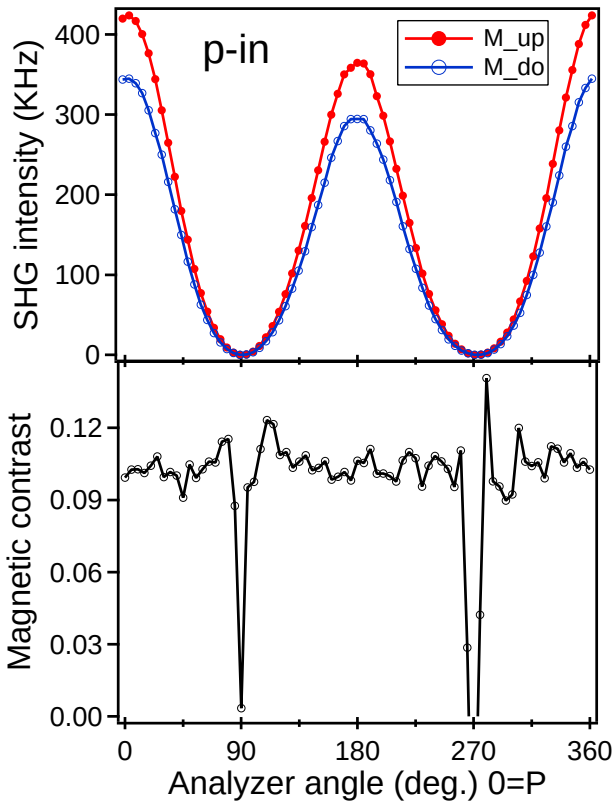


**Figure 5.2:** Variation of the SHG signal (upper panel) and magnetic contrast (lower panel) as a function of analyzer angle for a p-polarized fundamental measured on a 20 nm Gd(0001) film at a temperature of 110 K. The solid lines are guide for the eye.

of $\omega$ photon frequency) and the SH beam, respectively. The $\lambda/2$ plate is used to rotate the polarization of the incident laser beam whereas the Glan-Thompson polarizer is analyzing the polarization of the output SH signal. The measurements are done either by varying the polarization of the fundamental and detecting the SHG signal at a fixed polarization orientation (P or S polarized output)[2] or the opposite way. The azimuthal dependence of the SHG yield *i.e.* as a function of sample rotation, could not be investigated since the sample mounting system in the UHV chamber does not offer such a capability. In principle one can circumvent this drawback, by simultaneous variation of the polarization and analyzer angle for fundamental and SH beam, respectively, and thus obtaining the same information as measuring the SHG azimuthal dependence.

In figure 5.2 the behavior of the SHG intensity and of the magnetic contrast as a function of analyzer angle is depicted for an incident p-polarized fundamental laser beam. In the upper part of the figure the SHG yield for opposite magnetization direction is shown. In the p-P geometry the contribution of the susceptibility tensor components (see table 3.2)

[2]The capital letters denote the SHG polarization orientation whereas small letters are used for fundamental beam polarization.

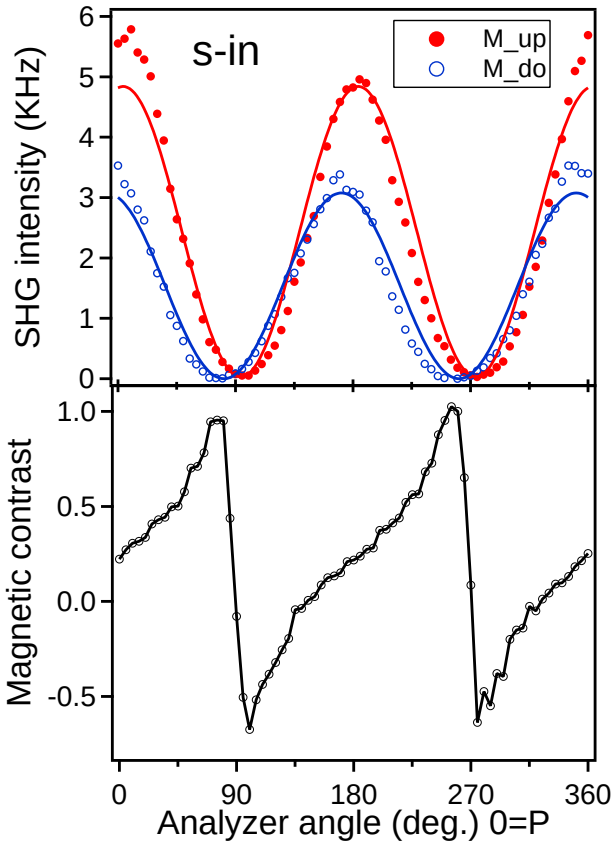


**Figure 5.3:** Variation of the SHG signal (upper panel) and of the magnetic contrast (lower panel) as a function of analyzer angle for a s-polarized fundamental beam. The solid lines in the top panel represent the fitting curves according to eq. 5.1.

to the SH signal interfere constructively that together with the bigger amplitudes of the Fresnel factors (eq. 3.21) for p-polarized fundamental and SH light produces a high SHG yield. As expected, for p-P polarization geometry the highest SHG signal is obtained. The magnetic contrast displayed in the lower panel is around 10% for p-P, a value that stays almost constant (within scattering of the data points) for all SHG polarization directions. The exception is the p-S geometry where the SHG signal and the magnetic contrast become zero since in this configuration no SHG tensor component is allowed (see table 3.2) *i.e.* due to symmetry constrains for this particular polarization combination.

The situation for a s-polarized input is presented in the figure 5.3. In comparison to the case of p-polarized input, the SHG intensity is one order of magnitude lower while the magnetic contrast is increased by at least a factor of two. Another difference compared with the previous case relies on the appearance of a shift between the curves for up and down magnetization direction. This shift represents the nonlinear Kerr rotation (analogous to linear MOKE) that is evaluated to $7\pm1$ degrees. For the p-polarized input no Kerr rotation can appear since the even and odd tensor components give a P-polarized component (see

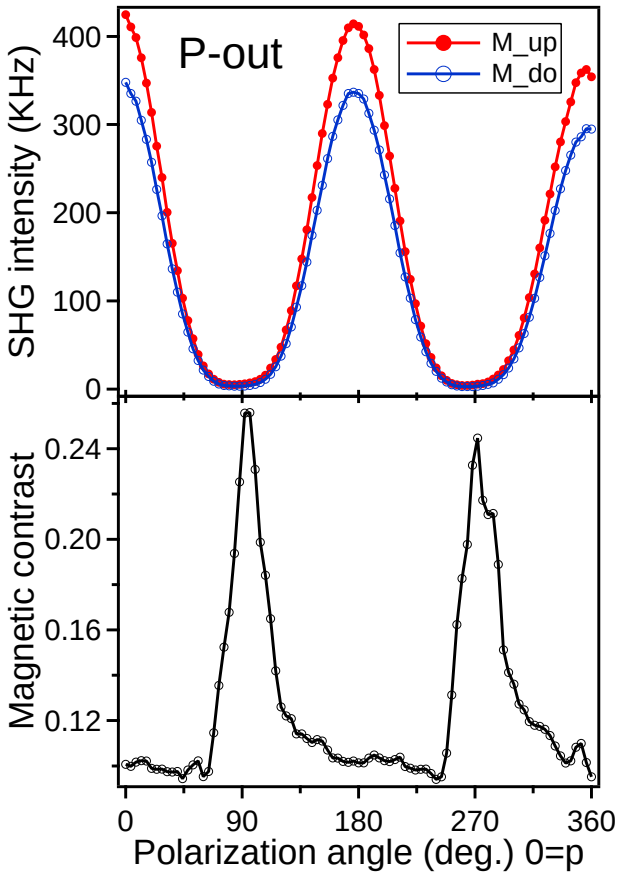


**Figure 5.4:** Variation of the P-polarized SHG signal (upper panel) and of the magnetic contrast (lower panel) as a function of polarizer angle measured from a clean Gd(0001) film. The solid lines are guide for the eye.

table 3.2) to the total SHG signal. The value of the Kerr rotation is deduced from fitting the data with the expression (deduced from eq. 3.21):

$$I_\alpha(2\omega, \pm M) = F_1 \cdot [cos^2(\alpha \pm \delta) \cdot \pi/180] + F_2 \tag{5.1}$$

that renders the SHG signal amplitude through $F_1$ and the Kerr angle $\delta$. In the argument of the cosine function $\alpha$ is the analyzer angle and while $F_2$ is an offset included for a better fitting.

Summarizing this part, the p-P polarization combination gives the highest contribution to the SH signal with a relatively high magnetic contrast. Although the magnetic contrast is larger in the s-P configuration the SHG efficiency is low and therefore this geometry is not reliable for further pump-probe measurements. Since we are primarily interested in a high SHG intensity, the p-P configuration has been chosen as the experimental geometry for all the following static and time-resolved experiments performed in this work.

Generally, owing to its sensitivity, SHG is used to study the symmetry of the surface

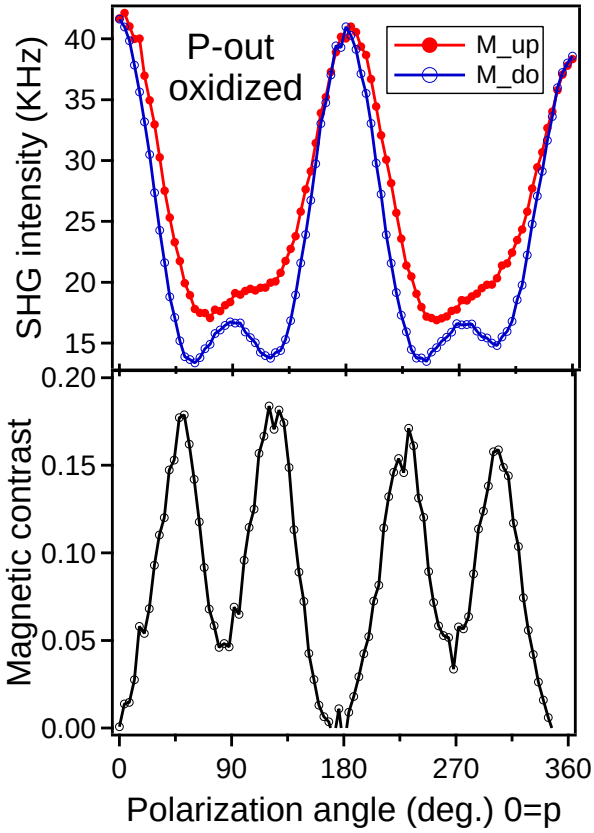


**Figure 5.5:** Variation of the P-polarized SHG signal (upper panel) and of the magnetic contrast (lower panel) as a function of polarizer angle measured from an oxidized (1 L $O_2$) Gd(0001) film. The solid lines are guide for the eye.

electronic structure [129, 108, 106, 102]. Here we want to investigate in which way is the surface electronic structure reflected in the polarization sensitive SHG measurements. More detailed, the purpose is to investigate whether or not the exchange-split surface state present on Gd(0001) [33, 29] is involved in the SHG process (see figure **??**) and if such, a resonance enhancement of the SHG yield is expected. In this context, one indication of the resonance enhancement is the SHG yield that can vary largely as the electronic structure is modified or the incident photon energy is varied. Complemented by measurements of the phase $\phi$, presented in the next section, one can get a complete picture of the optical resonance process. Here, we restrict ourselves to the investigation of a modified surface electronic structure by adsorbates on the SHG process. The phase measurements are presented later in this section.

For this type of measurements, a clean and an oxygen-covered Gd(0001) surface have been investigated. The idea is that upon oxidation the exchange-split surface state is shifted in energy below Fermi level (both components are occupied) but remaining exchange-split [31, 124]. Consequently the possible resonance in the SH generation pro-

cess will be lost. The Gd(0001) surface is oxidized upon exposing it to a nominally 1 Langmuir (1L=$10^{-6} torr \cdot s$) of oxygen at a sample temperature of 300 K. The oxidation of Gd(0001) surface results in a dramatic adsorbate-induced change of the surface electronic structure that affects the energetic position of the surface state. Therefore, the totally different electronic surface configuration obtained after oxidation might be used as a check for the SHG resonance enhancement. The results obtained for a clean and $O_2$ covered Gd(0001) surface for a P-polarized SHG output are depicted in figure 5.4 and 5.5, respectively. First, one notices the 10-times higher SHG signal generated from the clean Gd film in comparison to the oxygen-covered surface. Furthermore, two small additional peaks appear with the maximum centered the s-P orientation, that shows a 4-fold symmetry of the oxidized surface region which generates the SH signal. Regarding the magnetic contrast, a decrease of ≈35% is observed upon oxidation with the appearance of additional maxima. This value is in a good agreement[3] with the measurements of the surface oxide layer magnetization performed with magnetic circular dichroism in photoemission [124], that gives a reduction of ≈50% of magnetization relative to the clean Gd(0001) surface.

A general conclusion that can be drawn is related with the sensitivity of the SHG process to the surface electronic structure. After the formation of the oxide layer, the surface state is shifted below Fermi level [27, 124] with the majority and minority components positioned (for T=80 K.) at -0.8 eV and -0.35 eV binding energies, respectively [124]. The used photon energy (1.55 eV) does not match the energetic separation between the oxygen-formed surface state and the unoccupied $d$ band positioned ≈1.5 eV above $E_F$ (see figure 5.11). Therefore, the SHG optical transitions evolve non-resonant in this case and consequently the SHG efficiency is low. Thus, one can suggest that for the case of a clean Gd surface the SHG process evolve resonantly enhanced. In order to prove this proposal the MSHG phase measurements are required, which is the topic of the next section.

### 5.1.2 Phase-sensitive MSHG measurements

As mentioned earlier in this chapter, the relative phase $\phi$ between the even $E_{even}(2\omega)$ and odd $E_{odd}(2\omega)$ SH fields constitutes an important parameter that together with the SHG intensity provides a complete description of the MSHG response from a ferromagnetic sample (see eq. 3.33). Therefore, a simultaneous measurement of the SH intensity and phase is a prerequisite for the identification of a resonance in the SHG process and for a detailed understanding of the investigated system. In this section, the MSHG phase measurements performed on epitaxially grown Gd(0001)/W(110) thin films under UHV conditions are presented. The first part gives a short introduction regarding the phase concept in a SHG experiment and the practical modalities of measuring it. Thereafter, the actual phase measurements on Gd(0001) and the data analysis are presented in a step-by-step manner. Based on the combined measurements of the SH yield, relative phase and magnetic contrast we will show how one can conclude about the presence of a resonance in the SHG process.

We have seen in chapter 3, that the SHG response from a magnetized sample consists of even $\chi^{(2)}_{even}$ and odd $\chi^{(2)}_{odd}$ contributions *i.e.* which behave symmetric and anti-symmetric

[3] Accounting for the different depth sensitivity of the SHG and the photoemission techniques.

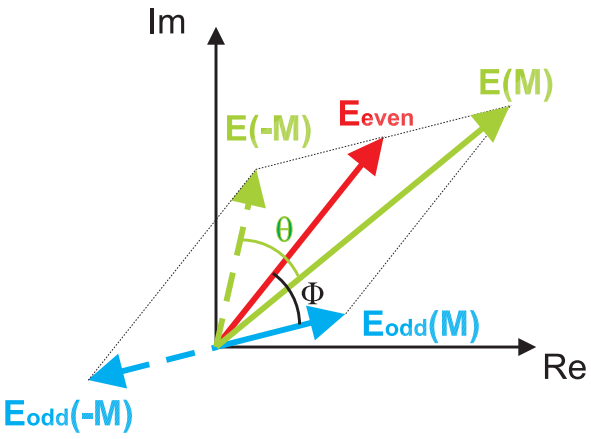


**Figure 5.6:** The representation of the even $E_{even}$ and odd $E_{odd}$ SH fields as well as the total SH field E(M) in the complex plane. Upon magnetization reversal a phase shift $\theta$ appears that determines the relative phase $\phi$ between even and odd SH fields.

with respect to magnetization reversal, respectively. In other words, the $\chi^{(2)}_{odd}$ exhibits a phase shift of 180° upon magnetization reversal *i.e.* it changes the sign, whereas $\chi^{(2)}_{even}$ is unaffected. These *effective* susceptibility tensors (see eq. 3.18) are linear combinations of tensor components multiplied by the corresponding Fresnel factors $f_{ijk}$ (see eq 3.21). They determine the SH field that can be written as:

$$E(2\omega) \propto \sum_{i,j,k} f_{ijk}\chi_{ijk} \equiv \chi_{eff} \tag{5.2}$$

Since the emitted SH field is a complex quantity (the Fresnel coefficients and the susceptibility tensors are complex numbers) one can write its expression in terms of amplitude and phase as:

$$E(2\omega) = |E(2\omega)|e^{i\varphi} \tag{5.3}$$

with the phase $\varphi$ being the sum of phases of all the complex numbers involved in eq 5.2. Now one can see that measuring the SH intensity $I(2\omega) \propto |E(2\omega)|^2$ the phase content is lost. However, employing interferometric techniques the phase information can be retrieved [131, 132, 133].

In a MSHG experiment the measured observable is the magnitude of the SHG signal for opposite magnetization directions. For sake of clarity we write again the expression of the SHG intensity as:

$$I^{\uparrow\downarrow}_{2\omega} \propto |E_{even}(2\omega)|^2 + |E_{odd}(2\omega)|^2 \pm 2|E_{even}(2\omega)||E_{odd}(2\omega)| \cos\phi$$

where $I^{\uparrow\downarrow}$ denotes the SHG intensity for up and down magnetization directions and $\phi$ is the relative phase between the even and odd SH fields. It is immediately obvious that the phase information can not be obtained directly by measuring only the SH intensity, since we do not have an independent information about the $E_{even}$ and $E_{even}$. Therefore, one has to employ the interference between the SHG light generated from the sample and from a reference source (usually a nonlinear crystal) in order to recover the phase information. For understanding of the *relative phase* concept in the framework of a MSHG experiment

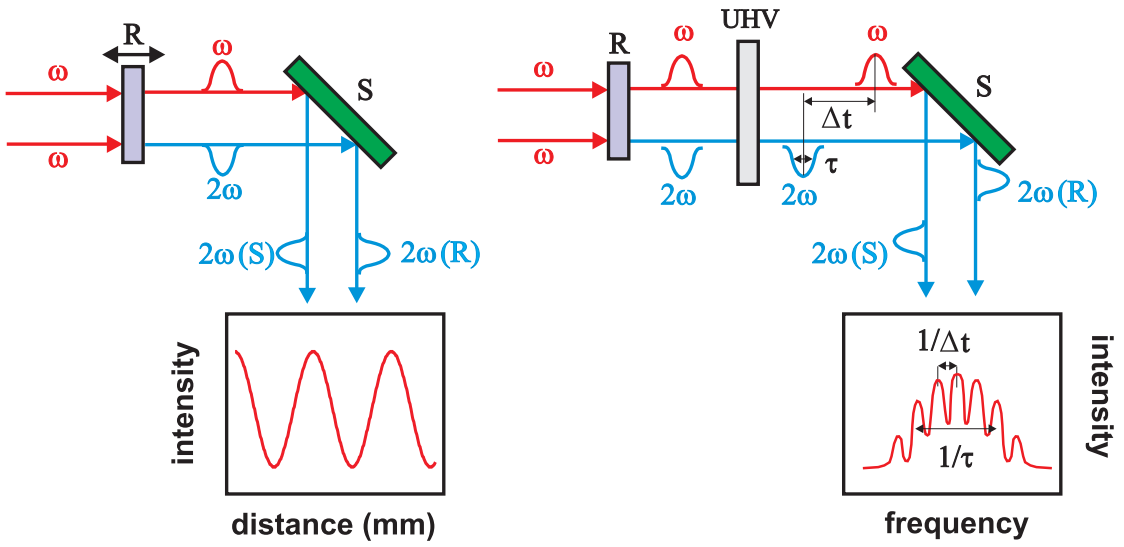


**Figure 5.7:** Schematic description of the time-domain (left) and frequency-domain (right) phase measurements. For time-domain measurements the pulses at $\omega$ and $2\omega$ are temporally overlapped (also spatially overlapped on the sample S) and the interference pattern (due to the dispersion of air between S and R) is obtained by translating the reference crystal (R). Frequency-domain phase measurements are necessary due to the presence of the UHV window that produces a time delay $\Delta t$ between the pulses of duration $\tau$. The frequency-domain interference pattern has a width $\approx 1/\tau$ and a period of modulation $\approx 1/\Delta t$. The reference crystal is fixed.

let us have a look at the *figure* 5.6. Here the even $\mathbf{E}_{even}$ and odd $\mathbf{E}_{odd}$ SH fields are plotted as vectors in the complex plane together with their sum $\mathbf{E}(\mathbf{M}) = \mathbf{E}_{even} + \mathbf{E}_{odd}$ that determines the measured signal. Upon magnetization reversal the odd component changes the sign $-\mathbf{E}_{odd}(-\mathbf{M})$ and consequently a *phase shift* $\theta$ between $\mathbf{E}(\mathbf{M})$ and $\mathbf{E}(-\mathbf{M})$ will appear. The relationship between phase shift $\theta$ that is measured in an interferometric MSHG investigation and the *relative phase* $\phi$ between $\mathbf{E}_{even}$ and $\mathbf{E}_{odd}$ is given by:

$$cos\phi = \frac{1 - I^{\uparrow}/I^{\downarrow}}{[(1 + I^{\uparrow}/I^{\downarrow})^2 - 4(I^{\uparrow}/I^{\downarrow})cos^2\theta]^{1/2}} \tag{5.4}$$

Another quantity of interest here is the magnetic contrast that can be directly obtain by measuring the SHG intensity for opposite magnetization directions. In connection with the relative phase $\phi$ it caries useful information regarding the relative contributions of the even and odd SH fields to the total SHG response, that can be deduced from the formula:

$$\rho = \frac{I^{\uparrow}(2\omega) - I^{\downarrow}(2\omega)}{I^{\uparrow}(2\omega) + I^{\downarrow}(2\omega)} = 2\frac{E_{odd}/E_{even}}{1 + (E_{odd}/E_{even})^2}cos\phi \approx 2\frac{E_{odd}}{E_{even}}cos\phi \tag{5.5}$$

where the assumption $(E_{odd}/E_{even})^2 \ll 1$ (see chapter 3) has been used. This assumption is demonstrated later in this section. Therefore, knowing the phase and contrast one can evaluate the ratio between the magnetic and nonmagnetic components $E_{odd}/E_{even}$ of the SHG response. Moreover, once the ratio $\frac{E_{odd}}{E_{even}}$ is deduced we can *disentangle the*

*values of the $E_{even}$ and $E_{odd}$ second-harmonic fields*, since $E_{even}$ is easily obtained from $E_{even} \approx \frac{I^{\uparrow}+I^{\downarrow}}{2}$. In the following the measured data will be presented in terms of the relative phase $\phi$ and the ratio $E_{odd}/E_{even}$.

**How to measure the relative phase $\phi$ ?**

As has been discussed in the beginning of this section, by measuring the intensity alone the phase $\phi$ content of the SHG response is lost. However, it can be detected in an interferometric manner [131, 133] using the SHG signal produced by a nonlinear reference source. As shown schematically in the figure 5.7 left, by superimposing the SHG signal from the sample and from the reference source, an interference pattern is observed when the optical phase delay between the pulses is varied. The optical phase delay[4] arises from the different phase-velocity dispersions of the medium (air in this case) for the propagating fundamental and SH light. Alteration of the optical phase delay can be done either by changing the refractive index of the medium or by varying the reference source-sample distance [131] (as in the figure 5.7). Such a time-domain measurement is conditioned by the time-overlap of SH pulses. This condition is not fulfilled when a strong dispersive element is involved in the experimental scheme *e.g.* when the phase measurement is performed under UHV conditions (see figure 5.7 right). Due to the different group-velocity ($v_g$) dispersion in the UHV window for the fundamental and the second-harmonic beam, a time delay $\Delta t = d(v_g^{-1}(2\omega) - v_g^{-1}(\omega))$ appears between the pulses. Such a time delay[5] is usually much bigger than the width $\tau$ of the laser pulses and consequently the time-domain interference is lost. Nevertheless, for measurements performed under UHV conditions the interferometric phase detection can be done in the frequency domain.

As was first demonstrated by Veenstra *et al.* [133], one can use the fact that in the frequency domain the femtosecond pulses have a broad bandwidth. Thus, a time delay $\Delta t$ between the laser pulses (of width $\tau$) is equivalent in the frequency domain to a spectral interference pattern of $1/\tau$ width, modulated at $1/\Delta t$ frequency (see figures 5.7 right and 5.8 middle). The phase of the modulation can be retrieved without the need to translate the reference source. In the measurements presented here a $z$-cut quartz crystal (0.25 mm thick) is used as a reference source, providing a large enough SHG intensity in order to match the level of SHG signal arising from the sample.

An example of spectral interferogram measured on Gd(0001) surface at T=100 K for up and down magnetization directions is displayed in the figure 5.8 middle. For this particular measurement the wavelength of the fundamental pulse is centered at 815 nm. One observes the interferogram peaks separated by an interval of 1.02 nm that corresponds to a time delay $\Delta t$ of 0.5 ps superimposed on spectral envelope of 6.32 nm HWHM (half-width half-maximum). The phase shift $\theta$ is obtained in the following way: the measured interferometric pattern is Fourier transformed and the so-called *autocorrelation function* [133] is obtained that exhibits a central peak with two satellites situated at $\pm\Delta t$ as displayed in the inset of figure 5.8. The central peak reflects the envelope of the laser pulse in

[4]Optical phase delay is given [133] $P(d) = \frac{4\pi\Delta n_{air} d}{\lambda}$ where $\Delta n_{air}$ is the difference in the refractive index for fundamental and SH beams, $d$ is the beams travelling distance, $\lambda$ the fundamental wavelength.

[5]For a fused silica window of 3 mm thickness and a pulse duration of 35 fs of the fundamental beam, the resulting delay $\Delta t$ is around 0.5 ps.

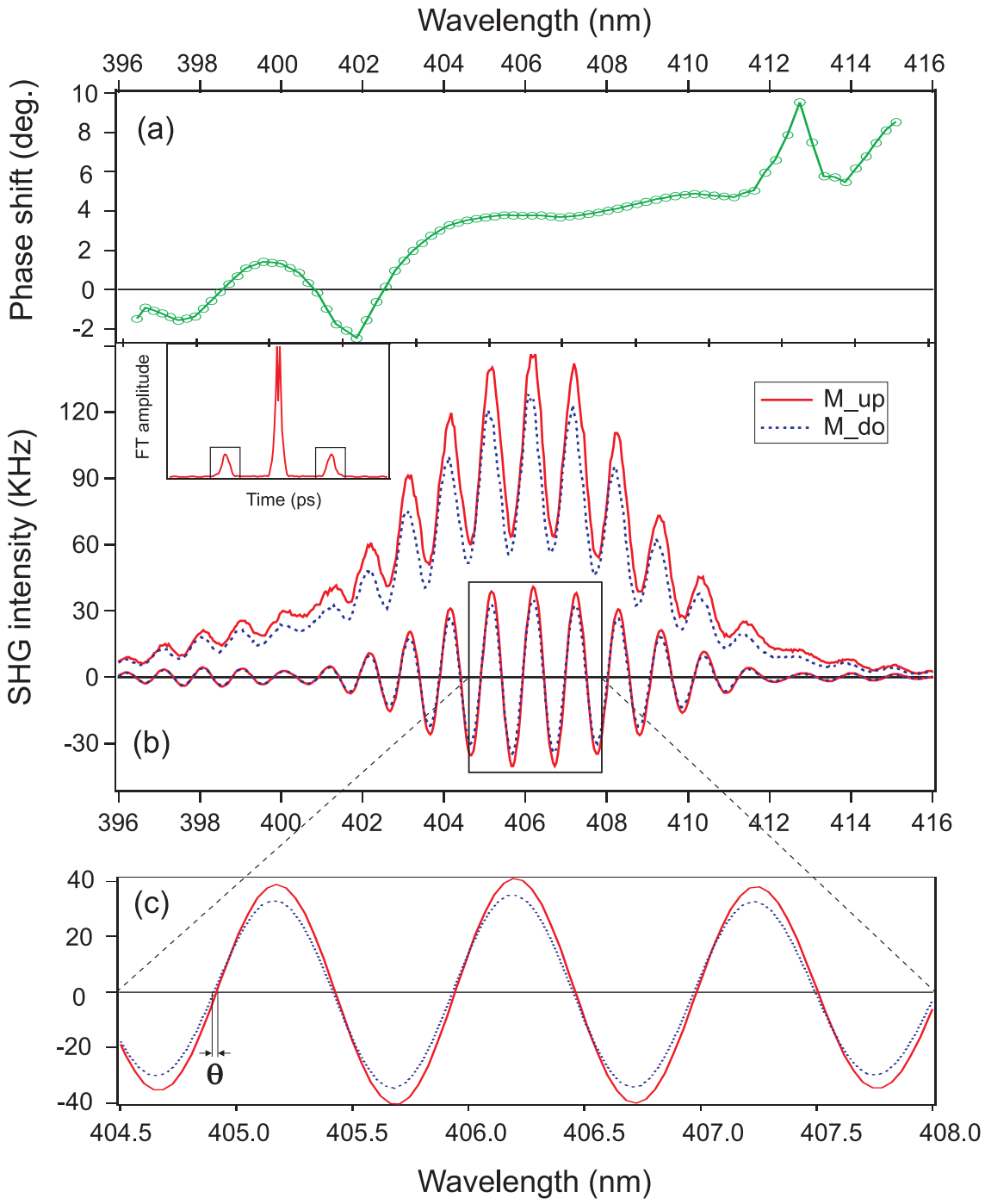


**Figure 5.8:** Example of interferometric pattern (middle panel) as measured on Gd(0001) surface for up (solid curve) and down (dotted curve) magnetization directions. The inset shows the Fourier transform of the modulated interference spectrum. The pure oscillatory component (middle panel) of the raw data results from the back Fourier transform of the satellite peaks displayed (framed) in the inset. The resulting phase shift $\theta$, displayed in the top panel, is extracted by making the difference of the oscillatory data obtained for opposite magnetization direction at their zero point. For clarity, a zoom in the framed region of the oscillatory component is depicted in the lower panel.

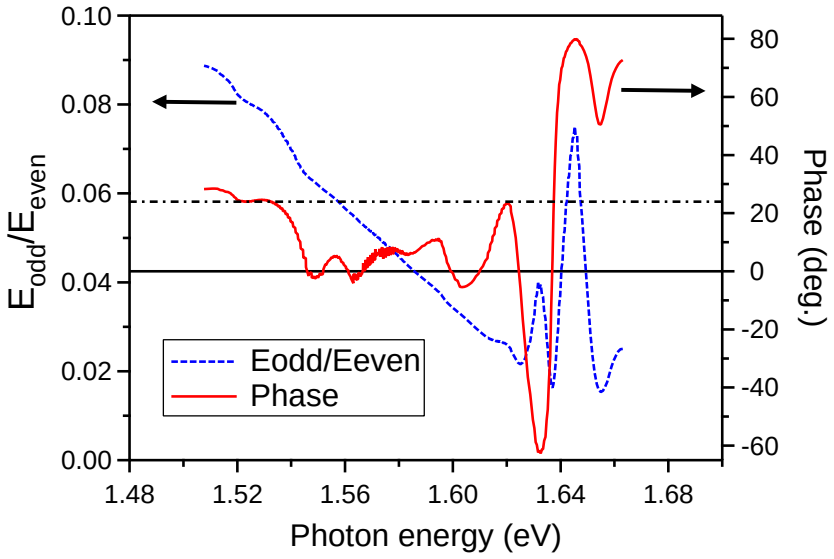


**Figure 5.9:** The spectral dependence of the relative phase $\phi$ (solid line) and of the amplitude ratio $E_{odd}/E_{even}$ measured on Gd(0001) at 90K.

the spectral domain while the satellites represent the modulations with $1/\Delta t$ periodicity. Performing the back Fourier transform only for the satellites the oscillatory component of the raw data is separated. The obtained band-pass filtered interferograms are shown in the middle panel of the figure 5.8. From here the phase shift $\theta$ can be derived by measuring the difference between the interference patterns obtained for opposite magnetization directions at their zero line crossing, as plotted in the lower panel of figure 5.8. The resulting phase shift along the measured spectrum is displayed in upper panel of the figure 5.8. In order to cover the whole available spectral range (here 740nm-860nm), the procedure is repeated (here six times) each time when the central wavelength of the laser pulse is tuned. The resulting phase shift $\theta$ is used to evaluate the the relative phase $\phi$ according to eq. 5.4.

### Results

The measured values of the relative phase $\phi$ between 1.48 eV and 1.68 eV fundamental photon energy, determined as described above, are plotted in the figure 5.9. From the magnetic contrast, that is measured simultaneously with the relative phase (deduced from the SHG yield), the $E_{odd}/E_{even}$ ratio is calculated according to eq. 5.5. Hence, we plot together with the relative phase also the dependence of the $E_{odd}/E_{even}$ ratio on the photon energy. The spectral dependence of the magnetic contrast and of the SHG intensity are displayed separately in the figure 5.10.

The main purpose of the spectral investigation of the relative phase and SHG yield is to determine whether or not the SHG process evolves resonantly at the Gd(0001) surface. As was shown in chapter 3, the presence of a resonance in the SHG optical transitions

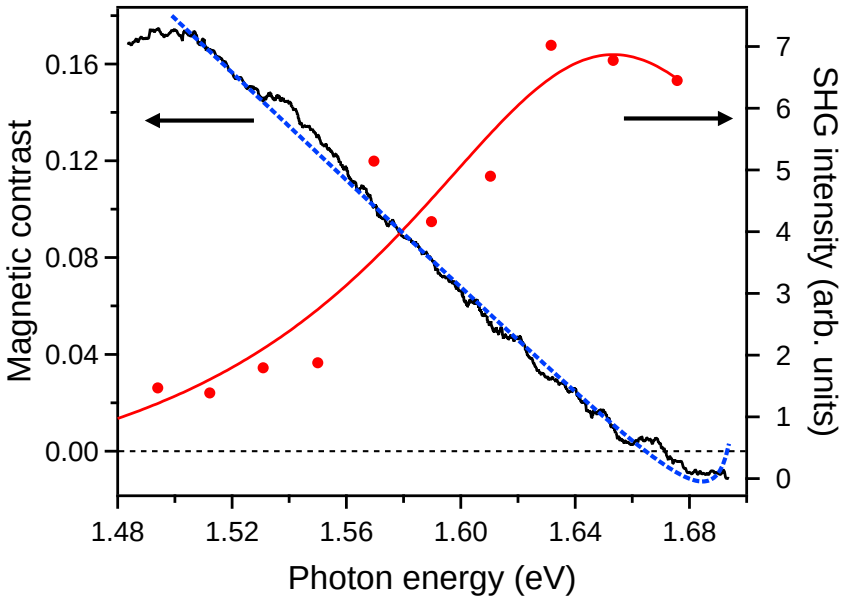


**Figure 5.10:** Magnetic contrast and the SHG intensity dependence on the fundamental photon energy. The dashed curve represents the fit of the magnetic contrast dependence according to expression 5.6. The solid line represents a lorentzian fit of the SHG intensity data.

results in an increased magnitude of the susceptibility tensor and a phase change of 180°, as the optical transitions crossed the resonance (see figure 3.2). The magnitude of $\chi^{(2)}$ is reflected in the SHG intensity and therefore one expects an increased SH signal at the resonance. In a real experiment, the increased SHG yield, solely, can not be considered as an indication for the presence of a resonance since it can be influenced by many factors *e.g.* morphology, adsorbates etc. However, the simultaneous observations of a phase change and an increased SHG signal as the incident photon energy is varied, it is considered as an evidence for the resonance [106, 102].

Such a behavior is observed for the SH signal on the Gd(0001) surface, as shown in the figure 5.10. Over the investigated photon energy range, the SHG intensity increases gradually by almost one order of magnitude, from 1.48 eV with a maximum around 1.67 eV. Simultaneously, the relative phase, displayed in figure 5.9, varies within an interval of 150°. The dependence of the relative phase $\phi$ on the photon energy exhibits a complex structure by changing its sign several times and showing pronounced modulations between 1.62-1.66 eV. Such phase changes are difficult to interpret as a resonance signature. However, the magnetic contrast varies strongly with the photon energy showing a sign change, that is a typical signature at the resonance [102, 106], in the region of maximum SHG intensity. Accounting for the behavior of the SHG signal and magnetic contrast (see fig. 5.10) we deduce that the resonance maximum is around 1.7 eV which is also confirmed by the DOS structure in fig. 5.11.

Although the spectral dependence of the phase is within 150°, does not show a gradual variation as has been measured for longitudinal geometry [102]. This behavior might arise

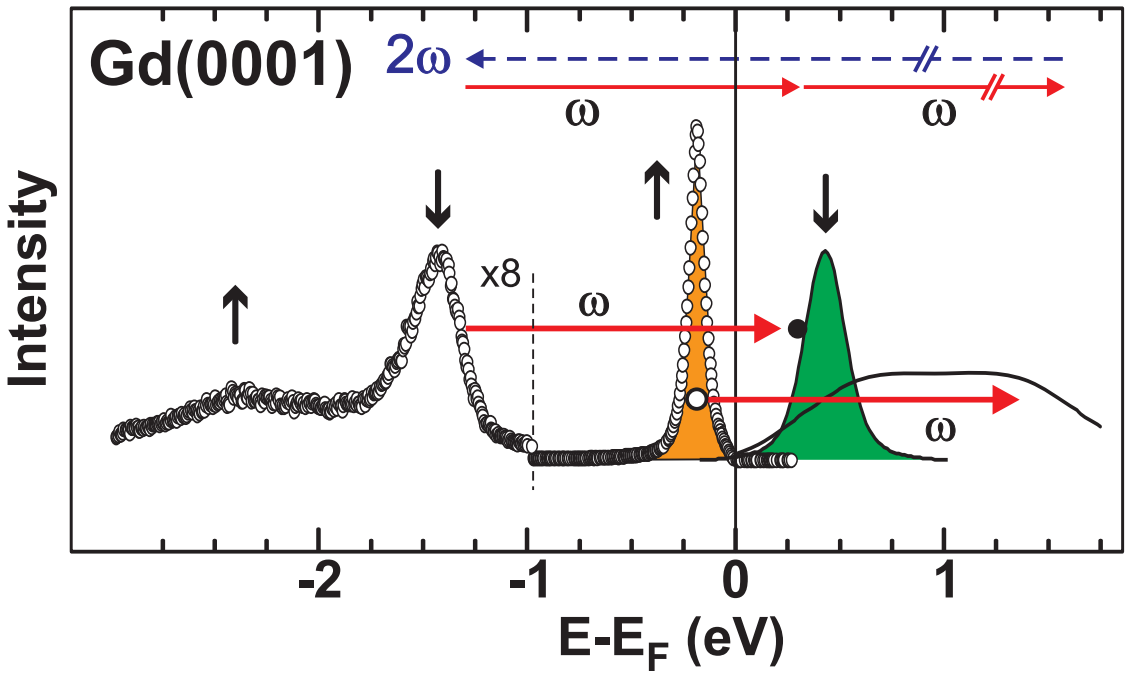


**Figure 5.11:** The valence electronic structure of Gd(0001) at $\overline{\Gamma}$ as measured by photoemission [17], inverse photoemission [32] and scanning tunnelling spectroscopy [48]. The arrows involving the exchange-split bulk state and the surface state close to $E_F$ depict the fundamental optical transitions at a photon energy of 1.5 eV that define the spin-up and spin-down contributions to the SHG response (see text). For clarity, the other optical transitions of the SHG process are not shown here. The resonant SHG process, enhanced by the unoccupied $S^{\downarrow}$ surface state component as an intermediated state, is displayed in the upper part of the figure.

from the higher number of allowed tensor components (each carrying a phase content) in the transversal geometry, that can lead to a complex interplay of their phases as the photon energy is varied, which eventually gives the observed relative phase behavior. However, the combined observation of the SHG intensity, of the magnetic contrast spectral dependence as well as the dramatic SHG yield decrease upon surface oxidation (see preceding section) lead us to conclude that the SHG process encounter a resonance at the Gd(0001) surface. Our conclusion corroborates earlier MSHG measurements [102] of the Gd(0001) surface performed in the longitudinal geometry, that have shown the presence of the SHG resonance.

In order to understand how the resonance process can explain the presented results let us have a closer look at the valence electronic structure of Gd(0001) depicted in the figure 5.11. Here one sees that the optical transitions at fundamental frequency (in this case 1.5 eV) are nearly matching the energetic separation between the *5d* bulk state and the unoccupied surface state for the spin-down channel. For the spin-up channel the optical transitions evolve between the surface state and the broad unoccupied bulk state, that is rather flat in this spectral region. Thus, the unoccupied minority surface state and majority bulk state can be considered as intermediate states for the SHG process.

Inspecting the spin-up optical transitions at the Gd(0001) surface, one notices that the final state is a broad (≈1.2 eV) and flat bulk state. On the other hand, the optical transitions in the spin-down channel evolves via a narrow surface state component (linewidth of ≈100 meV at 100 K [33]). Hence, as the photon energy is increased, one can consider the spin-up transitions to have a rather constant contribution to the total SHG response in comparison to the transitions in the spin-down channel. This is due to the specificity of the Gd(0001) electronic structure within the employed photon energy.Based on these considerations, we can ascribe the strong variations in all the measured SHG quantities with the laser photon energy to the relative weight of the spin-up and spin-down optical transitions to the SHG response, with the latter ones having the dominant contribution.

This point is supported by the observed dependence of the magnetic contrast and SH signal on the photon energy. Both quantities plotted in the figure 5.10 exhibit initially a constant level between 1.48 and 1.52 eV range. Starting with 1.52 eV, that coincides with the onset of the spin-down transitions, pronounced variations in $\rho$ and $I(2\omega)$ set in, that reach a minimum respectively a maximum at 1.67 eV. The interpretation of the SHG signal dependence is based on the magnitude of the susceptibility tensor (see fig. 3.2) as the electronic transitions approach the resonance. This is described as follows. In the low photon energy range the spin-down transitions evolve off-resonant while the spin-up give a constant contribution. Increasing the photon energy, the energy separation between spin-down bulk and surface state is gradually better matched, the resonance condition is better fulfilled, that explains the SHG signal increase. Also one can interpret the SHG intensity behavior in the view of equation 3.33. Here the absolute values of the even and odd fields contribute to the SH signal while the $cos(\phi) \approx 1$ throughout the investigated energy interval (except the oscillatory feature). A simple estimation of the the contributions of the even and odd field to the total SHG intensity shows that even component prevails (is a factor of 10 to 100 higher along the investigated spectral range). Thus, the SHG intensity is mainly determined by the $E_{even}$, whose value increases with the photon energy due to the resonance presence. The variations in odd field add up to the even field and produce the observed monotonous increase of the SHG yield. But how can we explain the magnetic contrast dependence?

The variation of the SHG magnetic contrast has been shown [102, 119, 106] to be determined by the relative contributions of the spin-up and spin-down optical transitions that have different signs. Thus, the spin-up channel provides a nearly constant (due to the broad final state) and positive contribution whereas the spin-down channel contribution is negative and increases with photon energy. Starting with 1.52 eV (the onset of transition see fig. 5.11) the contribution increases considerably and eventually overcomes the positive one at 1.67 eV (see the contrast sign change in figure 5.9). The constant level of $\rho$ at 1.48 eV is also explained since for the spin-down channel, off-resonant transitions take place below 1.52 eV while the spin-up contribution is nearly constant (due to the small variations with photon energy). Consequently, we show that the balance between optical transitions involving electrons with opposite spin orientations via the surface state describes the magnetic contrast behavior. Therefore, the magnetic contrast is a measure of the spin polarization of the surface state on the Gd(0001) surface, in agreement with literature [17, 119].

The behavior of the magnetic contrast can be simulated in the framework of a simple model that describes a double resonance condition and accounts for the relative contributions of the optical transitions in the spin-up and spin-down channels. The expression used in the model reads:

$$\rho = f_0 + \frac{f_{up}}{\hbar\omega - E_{up} + i\hbar\Gamma_{up}} + \frac{f_{down}}{\hbar\omega - E_{down} + i\hbar\Gamma_{down}} \tag{5.6}$$

where $\hbar\omega$ is the photon energy, $E_{up}$ and $E_{down}$ are the energetic separations in the spin-up (surface state-unoccupied bulk state) and spin-down (occupied bulk state-unoccupied surface state) channel at a temperature of 100 K (see figure 5.11), $\Gamma_{up}$ and $\Gamma_{down}$ represent the linewidth of the optical transitions determined by the convolution of the linewidth of the initial and final state with the experimental resolution (given by the laser pulse). The $f_{up}$ and $f_{down}$ are the factors that describe the matrix elements for the majority and minority electrons, respectively, whereas the non-resonant contribution is given by $f_0$. The non-resonant contribution contains the contributions from all possible optical transitions over the bandstructure. The resulting fit curve is plotted in upper panel of the figure 5.9. As discussed above, if the dependence of the contrast is determined by contributions from optical transitions involving electrons with opposite spin than the matrix elements would have also opposite signs. This result is found by fitting the contrast with the model formula. The input fixed parameters are: $E_{up}$=1.7 eV, $E_{down}$=1.8 eV. The output fit values are $\Gamma_{up}$=2.182±0.1 eV and $\Gamma_{down}$=1.072±0.05 eV, $f_{up} = 0.00337 \pm 1 \cdot 10^{-5}$, $f_{down} = -2.312 \pm 0.006$ and $f_0 = 2.3772 \pm 0.006$. Despite of the simplicity of the model we see that gives a good description of the measured magnetic contrast (see fig. 5.10) reproducing even the sign change around 1.67 eV. Moreover, it confirms our assumption of positive and negative signs of the matrix elements for the spin-up and spin-down optical transitions, respectively, that determine the spectral behavior of the magnetic contrast.

Finally, we address the modulation observed in the phase and the amplitude ratio of the SH fields. This modulation appears in the spectral range where the strength of the spin-down transitions reaches a maximum, as judged from the behavior of the SHG signal and magnetic contrast. The peak-to-peak splitting amounts to 13 meV that represents a frequency of 3.1 THz. This value is in a good agreement with the observed (reported in section 5.3 and [17]) phonon-magnon mode at the Gd(0001) surface that oscillates at a frequency of 2.9 THz in time domain. Thus, one might consider [119] the oscillatory feature of the phase and $\frac{E_{odd}}{E_{even}}$ measured in the frequency-domain to be related to the oscillation of the surface state peaks due to the surface phonon mode. However, this issue requires further detailed investigations for a clear identification of the modulation source.

### 5.1.3 Conclusions

The polarization-dependent measurements performed on Gd(0001) revealed the p-P polarization geometry to be optimal in terms of SHG efficiency and the magnitude of the magnetic contrast. From now on this will be the experimental geometry of choice for all static and time-resolved MSHG measurements. For the case of a s-polarized incident fundamental beam, a Kerr rotation is detected that amounts to approximately 7°. The high surface sensitivity exhibited by the SHG process has been demonstrated by measuring the

nonlinear response of a clean and oxygen-covered Gd surface. The dramatic decrease of the SHG signal after the oxidation of the Gd surface has been considered as an indication for the resonant character of the SHG process that evolves via the surface state components. This suggestion has been proved by the spectral dependence of the SHG intensity and of the magnetic contrast. The relative phase varies over a large interval ($\approx$150°) showing a complex structure with a pronounced oscillatory feature in the high photon energy range.

## 5.2 Laser-induced magnetization dynamics on Gd(0001)

With the provided detailed knowledge about the static properties of the ferromagnetic Gd(0001) from the previous section, one can proceed in investigation of the dynamic properties of the system. That means the time-dependent behavior of the constituent sub-systems: electrons, lattice and spins after a femtosecond laser pulse excitation. These properties are investigated employing the *pump-probe technique* in which the system is excited by an intense pump pulse. The temporal evolution after excitation is monitored by a weaker, time-delayed probe pulse that takes actually "snapshots" *i.e.* frozen pictures in the time-domain of system's behavior after excitation. The time delay is realized by varying the optical path length between pump and probe pulses.

Here, the pump-probe magnetization-induced second harmonic generation MSHG is employed. The Gd(0001) surface is excited by a pump pulse with a wavelength of *e.g.* $\lambda$=800 nm and the pump-induced variations are detected by a probe pulse at the second-harmonic photon frequency *i.e.* $\lambda$=400 nm. This technique possesses the advantage of simultaneous detection of the electrons/phonons as well as the magnetic system behavior (see chapter 3).

The time-resolved MSHG is used in order to investigate the photoinduced changes in the magnetization of the ferromagnetic Gd(0001) surface. The main goal is to determine and disentangle the elementary spin-dependent scattering processes that drive the laser-induced demagnetization and their characteristic time scales. The nonlinear magneto-optical investigations, which have been considered within the present thesis, are complemented by time-resolved photoemission spectroscopy (TRPE) performed under comparable experimental conditions by Martin Lisowski and Panos Loukakos in our lab. The latter investigation tool is used to acquire additional information about the transient evolution of the electronic system after laser excitation.

This section is organized as follows: in the first part the photoinduced femtosecond demagnetization dynamics is presented whereas the magnetization relaxation evolving on several 100 ps time scale covers the second part.

### 5.2.1 Femtosecond demagnetization dynamics

As a starting point to our discussion regarding the laser-induced magnetization dynamics on Gd, a short remainder concerning the previous work done in the field and the magnetic properties of Gd in equilibrium, is considered. As detailed in section 2.5, the common believe in the community is that photoinduced demagnetization takes place within the first several 100 fs after the laser excitation [14]. Although various spin-scattering processes like

spin-orbit, electron-magnon, phonon-magnon have been invoked in order to explain this ultrafast demagnetization, an unambiguous identification of the responsible microscopic mechanism is still missing. For a better understanding a more systematic approach is necessary namely involving different investigation techniques on the same system. Thus, the combined insights gained from different experimental approaches provide a much clearer picture. Such an experimental strategy has been followed here in the case of ferromagnetic Gd(0001) surface using MSHG and TRPE as complementary investigation techniques.

Of central interest in our combined investigation is the exchange-split surface state present at the Gd(0001) surface [29, 33]. This can be considered as a model system due to the fact that reflects the degree of magnetic ordering[6] on Gd(0001), due to its localization (spatially and energetically) and large exchange splitting that amounts *e.g.* $\Delta_{ex}$=0.6 eV at 100 K [33, 34]. Therefore, the effect of laser excitation on the magnetization behavior is monitored by measuring the transient spin polarization (with MSHG) and the $\Delta_{ex}$ (with TRPE) of the surface state.

It is important at this point to clarify in how far one can make the connection between the spin polarization of the surface state and the surface magnetization. As shown in chapter 3, with MSHG one can measure the transient magnetization dynamics accompanied by a spectroscopic factor (see eq 3.44), that gives the optical response of the system within the involved photon energy range. For an exchange-split band structure one measures the spin polarization of the probed electronic states. This is valid for any magneto-optical investigation technique *e.g.* time-resolved MOKE. The Gd(0001) surface state is energetically localized in the band gap of the bulk band structure and is exclusively probed by SHG due to the resonance condition. Thus the spin polarization of the surface state is measured with MSHG. Spatially the surface state is localized in the upper surface layer with a radial charge distribution localized on the atomic site. Hence, the surface state is sensitive to a local magnetic moment (gives the local quantization axis) or local magnetic ordering that does not vanish even above Curie point, being responsible for the observed residual exchange splitting. Within our spatial resolution (laser beam diameter) we average over these local magnetic ordering areas which give the overall spin orientation in the probed area and thus the magnetization. In conclusion, with MSHG we probe the surface magnetization via the spin polarization of the surface state within the spectral range[7] given by the employed photon energy and with a spatial extent given by the damping of the surface state wavefunction.

These characteristic attributes of the surface state have been measured before under equilibrium conditions in order to clarify the origin of magnetic ordering on Gd(0001) at finite temperatures. It has been shown [36, 33] that neither of the invoked models, Stoner and spin-mixing (see chapter 2), is reliable to explain the experimental observations since these models are idealized pictures of itinerant and localized spins, respectively. The present understanding relies on a combination of these models *i.e.* the exchange splitting and spin polarization decrease with temperature down to Curie point where the $\Delta_{ex}$ remains finite while the spin polarization vanishes. It will be interesting to see

[6] It was shown [31] for magnetic lanthanides that the exchange splitting of the surface state scales with the magnitude of the 4f moments which governs the magnetism of these elements.

[7] Employing much higher photon energies (≈9 eV) one could measure the 4f moments that give 90% of the total magnetic moment in Gd.

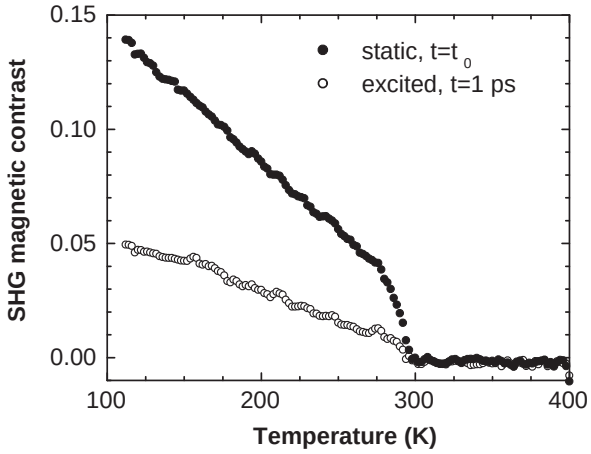


**Figure 5.12:** The evolution of SHG magnetic contrast as a function of temperature at the Gd(0001) surface. The filled and open circles represent the magnetic contrast measured in the static case (in absence of the pump pulse) and at a pump-probe delay of 1 ps, respectively. Note that both curves have been measured simultaneously by opening and blocking the pump beam that correspond to an excited and unexcited sample, respectively. From [134].

which of these models prevail under high non-equilibrium conditions provoked by the laser excitation.

In the previous section we have shown that the SHG process at the Gd(0001) surface evolves resonantly enhanced via the surface state components [102, 119]. Hence, apart from its intrinsic surface sensitivity based on symmetry considerations, the SHG is particularly sensitive to the exchange-split surface state present at the Gd(0001) surface. From the spectroscopic investigation of the SH response, presented in the preceding section, we have concluded that MSHG measures the magnetization at the surface via the spin polarization of the surface state [17].

An illustrative example of how sensitive is the MSHG to magnetic ordering at the surface is presented figure 5.12. Here the variation of the SHG magnetic contrast $\rho$ (defined in eq. 3.34) with the temperature resembles clearly the well-known M(T) Curie-Weiss law dependence [135]. The dependence of $\rho$ on temperature is quasi-linear until it is approaching the critical region in the vicinity of Curie temperature. This quasi-linear behavior in M(T) is usually ascribed to the reduced dimensionality of the magnetic thin films [37]. This is most likely also the case here, since the probed region is restricted to the upper two layers of Gd(0001) (see chapter 3). Such a behavior has been reported for Gd(0001) thin films investigated with surface sensitive techniques [35]. The bulk Curie point of $T_c$=293 K is well reproduced[8] while above $T_c$ the magnetic contrast is vanishing. These results are evidence for the absence of an enhanced surface $T_C$, which also confirm earlier investigation [35] regarding this issue.
The second curve in the figure displays the magnetic contrast measured at 1 ps delay after pump pulse excitation. Both curves, measured in equilibrium and non-equilibrium conditions, show a similar temperature dependence but for the excited case a decrease of ≈60% from the equilibrium value is observed. From here one can conclude that the laser excitation produces a partial demagnetization of Gd(0001) sample within 1 ps. Such

[8]The Curie temperatures of a 20 nm thick Gd(0001) film is 293 K, which is identical to bulk $T_C$ [136].

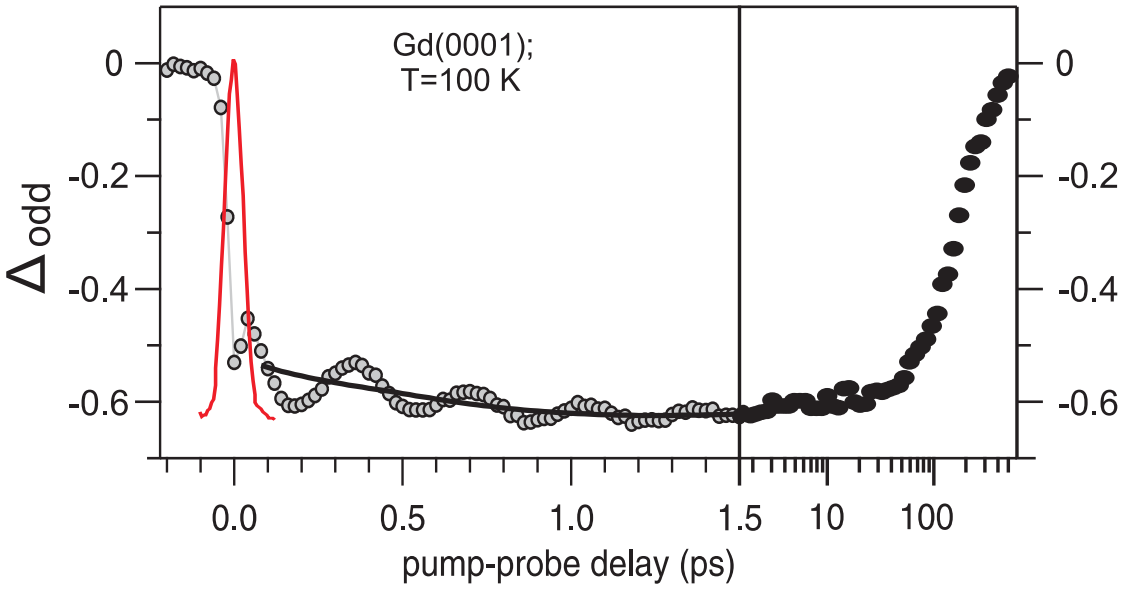


**Figure 5.13:** The pump-induced variations in the odd SH field, that measures the dynamics of the spin-polarization at Gd(0001) surface after excitation with a 35 fs pump pulse (the curve centered at zero delay scaled to $\Delta_{odd}$). The sudden breakdown of $\Delta_{odd}$ take place within pulse duration, reaches the minimum at 1.5 ps and comes to the initial level at 500 ps (right panel). The line denotes the incoherent (non-oscillatory) contribution to the signal after subtraction of the oscillatory part (see text).

an interesting observation gives us a flavor about the ultrafast demagnetization dynamics encountered on Gd, that will be the topic of the following part.

We further proceed in presenting the time-resolved MSHG data measured on Gd(0001). From the detected second-harmonic intensities for opposite magnetization directions and as a function of pump-probe delay, the normalized intensities $R(t)^{\pm} = \frac{I^{\uparrow}(t) \pm I^{\downarrow}(t)}{I^{\uparrow}(t_0) \pm I^{\downarrow}(t_0)}$ are computed, where $t_0$ denotes negative time delays. The measured data are presented as pump-induced variations in the even and odd SH fields, that are denoted by (see for details chapter 3): $\Delta_{even} = \frac{E_{even}(t)}{E_{even}(t_0)} - 1$ and $\Delta_{odd} = \frac{E_{odd}(t)}{E_{odd}(t_0)} - 1$, respectively.

The pump-induced variations in the odd SH field, which reflect the transient spin polarization of the surface state, are displayed in the figure 5.13. In the first place we notice (for a pump fluence of $\approx 1 mJ/cm^2$) a sudden drop that amounts to 50% from the equilibrium spin polarization value (at negative delays). Second, this abrupt decrease takes place within laser pulse duration depicted in the figure by the curve centered at zero delay. The minimum (60% decrease) in the transient odd field is reached around 1.5 ps and remains at this value up to 40 ps delay time. The spin polarization recovers on a 500 ps time scale (the right panel of the figure 5.13) and it will be discussed in the next section.

The pronounced oscillations with a period of 340 fs that are superimposed on the incoherent (non-oscillatory) background have been ascribed to a coherent phonon-magnon mode [17] excited at the Gd(0001) surface. A detailed investigation of their excitation and relaxation will be presented in the next section. For the discussion of the incoherent

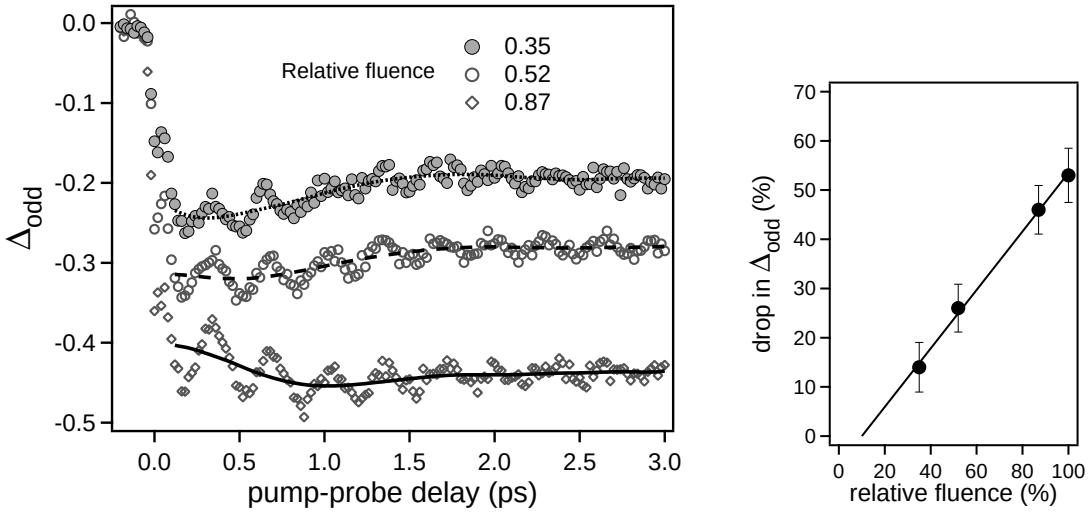


**Figure 5.14:** Pump-induced variations in the odd SH field as a function of laser fluence. **Left**: The measured $\Delta_{odd}$ dynamics for various relative laser fluences. The solid, dashed and dotted lines denote the incoherent part of $\Delta_{odd}$, that reflect the transient spin polarization after excitation. **Right**: The measured drop in $\Delta_{odd}$ close to zero delay as a function of laser fluence, where 100% represents $1mJ/cm^2$. The 100% data point is from figure 5.13. The solid line is a linear fit to the data.

ultrafast drop in $\Delta_{odd}$ the coherent oscillations are not of interest and their contribution is subtracted[9] from the measured signal. The remaining incoherent component of $\Delta_{odd}$ (the full, dashed, dotted lines) is displayed in figure 5.14 left, for different pump fluences. As plotted in the figure 5.14 right, the breakdown in $\Delta_{odd}$ scales linearly with the pump fluence which indicates an ultrafast loss of spin polarization mediated by the photoexcited electron population. Note that the state-filling or bleaching effects [85] (see chapter 2 for details) can not be invoked here since the drop in the spin polarization persists up to 40 ps while the excited electron population is already relaxed to the lattice on 1 ps time scale (see fig. 5.16 upper panel and fig. 2.7).

As pointed out earlier, the spin polarization and the exchange splitting of the surface state are the two main ingredients that offer a rather complete picture about the magnetism-electronic structure interplay on Gd(0001) under equilibrium conditions. Hence, apart from the transient spin polarization at the surface measured with MSHG we want to investigate also the time evolution of the surface state exchange splitting upon laser excitation. For this purpose the time-resolved photoemission TRPE technique has been employed.

The TRPE provides a direct measurement of the electronic structure of the system under investigation in a time, energy, and angle-resolved manner. The technique relies on the detection the photoemitted electrons after laser pulse absorption via photo-electric effect. The measurement principle of the TRPE is schematically shown in figure 5.15 for

[9]The separation of the coherent and incoherent components of the MSHG response as well as the fitting procedure of the oscillations are presented in detailed in appendix B.

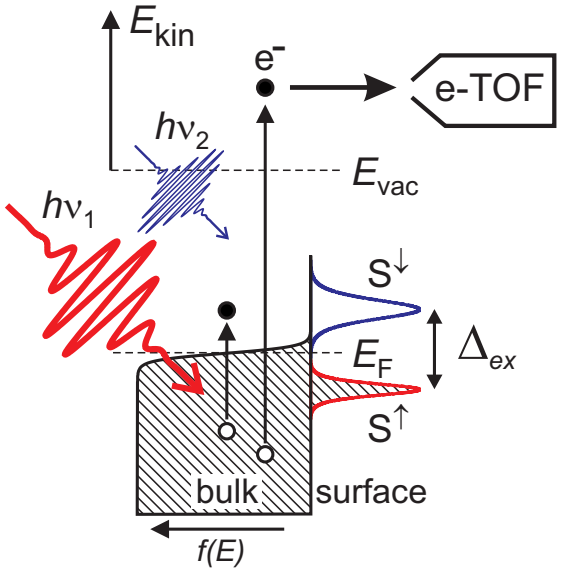


**Figure 5.15:** A schematic sketch of the TRPE experiment on Gd(0001). The pump pulse of 1.5 eV photon energy excites electrons from the bulk that populates the unoccupied part of the surface state $S^{\downarrow}$. The probe beam of 6 eV can excite electrons above vacuum level $E_{vac}$ from the bulk and from the surface state where their kinetic energy is detected with a time-of-flight spectrometer (e-TOF).

the case of Gd(0001) electronic structure in the vicinity of $E_F$. An intense laser pulse (the pump) of energy $h\nu_1$ (here 1.5 eV) excites electrons from the bulk states and the occupied surface state component $S^{\uparrow}$, which are photo-ejected above vacuum level $E_{vac}$ by a less-intense, time-delayed probe pulse $h\nu_2$ (here 6 eV) (when $h\nu_2$ is above the work function $\Phi = E_{vac} - E_F$). The kinetic energy $E_{kin}$ of the emitted electrons is detected by a time-of-flight spectrometer (TOF). Due to the limited escape depth of electrons that amounts to several Å in the used photon energy range, the PE is also a surface sensitive technique. Considering the energy conservation of the entire process, one can obtain the energetic positions $E_i$ of the initial states (binding energies) of the detected electrons:

$$E_i - E_F = E_{kin} + \Phi - h\nu_2 \tag{5.7}$$

The resulting time evolution of the energetic positions for surface state components, upon laser excitation, is depicted in the figure 5.16. The binding energy of the $S^{\uparrow}$ varies gradually in a time interval of 2 ps by an amount of 45 meV towards $E_F$. Such a small energy gradient could not be detected in the case of the $S^{\downarrow}$ component due to its low intensity and larger linewidth. However, computing the sum between the measured binding energy transients for $E(S^{\uparrow})$ and $E(S^{\downarrow})$ one obtains the surface state exchange splitting $\Delta_{ex} = E(S^{\uparrow}) + E(S^{\downarrow})$ as plotted in the inset of figure 5.16. The resulting observation is that $\Delta_{ex}$ stays constant within error bars 0.6±0.06 eV in the investigated time range of 1 ps.

Another information that can be retrieved from the TRPE spectra is the photo-injected excitation strength of the electronic system that is described by the transient energy density $\varepsilon_{el}(t)$. According to the reference [56] the electronic energy density can be calculated as $\varepsilon_{el}(t) = 2\int_0^{2eV} N(E,t)|E|dE$, where $N(E,t)$ is the electronic population measured in the photoemission spectra and the factor 2 before integral accounts for equal contribution from electrons and holes. The computed $\varepsilon_{el}(t)$ is shown in the lower part of the figure 5.16 together with the transient population of the $S^{\uparrow}$ state (inset). One can observe that the

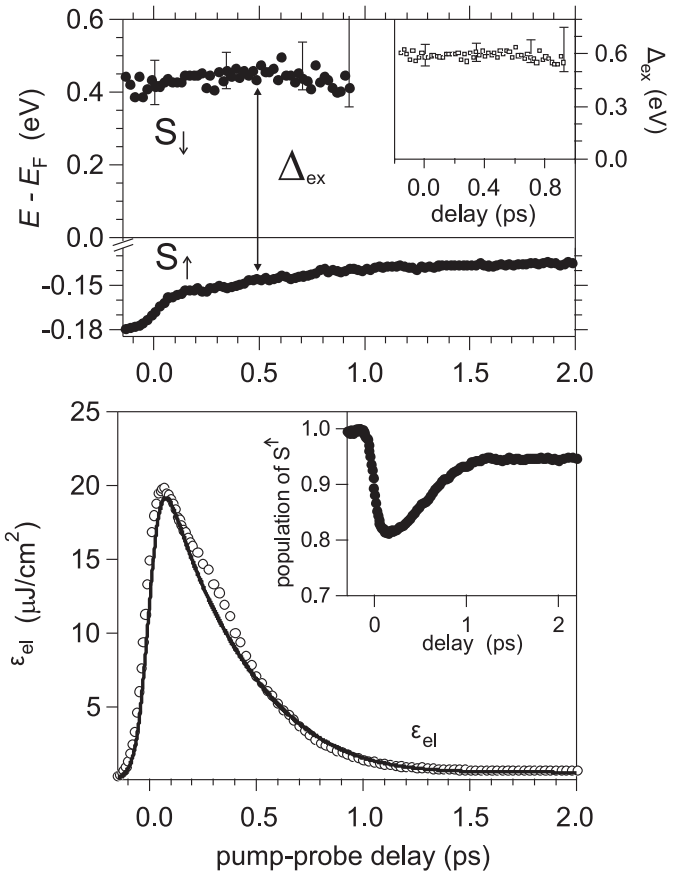


**Figure 5.16:** Upper panel: the transient binding energy for the $S^{\uparrow}$ and $S^{\downarrow}$ surface state components. The inset displays the resulting surface state exchange splitting $\Delta_{ex}$. Lower panel: the time evolution of the energy density $\varepsilon_{el}(t)$ (dots) and the fit according to the 2TM (solid line). The inset shows the change in the $S^{\uparrow}$ surface state population after excitation. From [13].

maximum in $\varepsilon_{el}(t)$ is reached around 100 fs and it decays in 1 ps time interval, usually via *e-e*, *e-p* and ballistic as well as diffusive transport [44, 56]. On the same time scale of 100 fs, a drop of 19% in the population of majority surface state is detected that levels out to a constant value close to 1 ps delay. A simple estimation of the excited electronic temperature gives a value of $\varepsilon_{el}/k_B$=1900 K, that quantifies the high excitation regime.

Summarizing the experimental observations, we notice that upon an intense laser excitation the spin polarization of the surface state decreases with 50% while its exchange splitting remains constant. This happens on the time scale when the electronic system is in a highly non-equilibrated state and *e-e* scattering dominates, as deduced from the transient energy density and the estimated value of the electronic temperature. Based on these observations, we can rule-out a demagnetization mechanism based on the Stoner model *i.e.* $\Delta_{ex}$ scales with M(T), and conclude that for the Gd(0001) surface, on the femtosecond time scale, the spin-mixing behavior dominates.

In order to develop a microscopic understanding of the observed phenomena one can

start by considering some potential spin-scattering processes responsible for laser-induced demagnetization in Gd, having in mind the particularities (localized magnetic moment, strong electron-magnon coupling) of this ferromagnetic system:

- the phonon-magnon scattering or the spin-lattice interaction has been shown ([79, 80] and the next section) to evolve on a 100 ps time scale in case of Gd(0001) and therefore can not be considered here
- the spin-orbit interaction, that is considered the main mechanism responsible for angular momentum transfer between the spin and orbital degrees of freedom, it is small for Gd [137] and thus of minor importance here
- secondary electron effects combined with transport processes
- electronic spin-flip scattering among spin-mixed states

In the following we will focus on the last two listed processes that will be discussed within the framework of figure 5.17. The upper part of the figure displays the optical excitation and the subsequent secondary electrons generation in the spin-resolved Gd(0001) band structure (calculated by Kurz *et al.* [26]). In panel (a) of the figure 5.17 the two channels of pump-induced optical transition are shown for a photon energy of 1.5 eV. There are transitions between the bulk bands as well as transition involving the surface state (also introduced earlier in the figure 5.11). The latter ones promote majority electrons from the surface state to bulk state whereas minority electrons are excited from the occupied bulk state into the $S^{\downarrow}$ surface state. As a result the spin polarization[10] of the surface state is reduced after excitation while for the bulk states it should be increased. The higher spin-polarization of the bulk states might be relaxed by transport into the bulk of the sample through ballistic and diffusive transport, that are taking place on this early time range after excitation.

Generally, the highly excited electron-hole pairs relax through inelastic *e*-*e* scattering that produces secondary electron cascades (see chapter 2). As plotted in panel (b), the generated secondary electrons might preserve the spin orientation (processes 1 and 2) or not (processes 1 and 3). The latter case accounts for Stoner excitations *i.e.* excited electron-hole pair with opposite spin orientation. Both type of processes lower the spin polarization of the surface state on the time scale of *e*-*e* scattering *i.e.* <100 fs but do not influence the spin polarization of the bulk states. Taking into account the linewidth $\Gamma$ of the surface state components that amounts to ≈100 meV at 100 K [48], one obtains a scattering rate of 0.1 $fs^{-1}$ and a short carriers lifetime ($\tau = \hbar/\Gamma$ of ≈10 fs). Therefore, frequent scattering events are taking place between the surface state and bulk electrons which will restore the electronic spin polarization to the equilibrium value before excitation. Such a process will evolve on the hot electrons relaxation time scale *i.e.* within the first 100 fs. We do not observe such a rapid recovery of spin polarization since the drop in the $\Delta_{odd}$ signal persists up to 50 ps. Therefore, the spatially redistribution of the spin polarization between the surface and bulk and the secondary electrons effects are not explaining the observed ultrafast loss of spin polarization.

[10] By spin polarization of the surface state is meant the difference between the majority and minority spin population of the surface state components

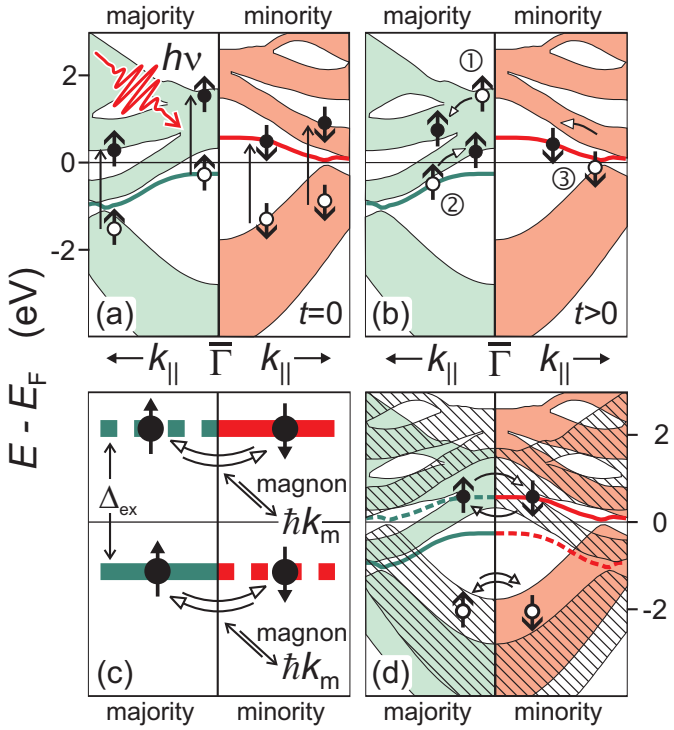


**Figure 5.17:** The description of the laser-induced ultrafast demagnetization scenario in the spin-resolved band structure of Gd(0001), calculated by Kurz *et al.* [26]. The green and the red filled areas are the majority and minority bulk states, respectively, while the thick lines close to Fermi level depicts the position of the exchange-split surface state. The panels display: (a) laser excitation of electron-hole pairs; (b) the *e-e* scattering; (c)(d) the spin-flip scattering among spin-mixed states involving surface state components(panel c) and bulk states (panel d). The dashed lines in panel (c) and the hatched areas in panel (d) represent the opposite spin states that together with the full lines and filled areas, respectively, generate the surface and the bulk spin-mixed states. From [13].

The remaining mechanism is the spin-flip scattering of hot electrons among spin-mixed states, that is discussed in the following. As pointed out earlier, the presence of a constant exchange splitting unaffected by the high electronic photoexcitation led us to the conclusion that spin-mixing behavior prevails on this ultrashort time scale. This is equivalent to the existence of degenerate spin-mixed electronic states as displayed in the panel (c) and (d) of figure 5.17, for the case of surface and bulk states, respectively. Hence, an electron in the majority surface state can scatter quasi-elastically with a minority electron situated at the same energetic position (dashed line), flip its spin, and consequently lower the surface state spin polarization. The conservation of angular momentum requires that the reduced momentum through the spin-flip event to be compensated by the absorption of magnon of energy $\hbar k_m$. The absorption and emission of magnons take place in the conduction band but might involve also the $4f$ moments via $4f - 5d$ exchange interaction. The calculated [138] exchange coupling between $4f - 5d$ electrons amounts to ≈100

meV that corresponds to ≈ 5 fs and thus in agreement with the observed drop of spin-polarization within the laser pulse duration. The probability of the electronic spin-flip with emission/absorption of magnons is governed by the strength of the electron-magnon coupling, that was shown to be comparable with the *e-p* coupling or even higher [57, 58] for Gd. Thus, the occurrence of this process will be also on the femtosecond time scale.

The spin-mixing behavior was encountered under equilibrium conditions also for the $5d$ bulk states on Gd(0001) [36]. Therefore we can extend this scenario for the bulk states and expect that spin-flip scattering is active also here as depicted in panel (d) which will lead to a spin polarization lowering in the bulk. To check this point a bulk sensitive technique is required, like time-resolved MOKE, that will be integrated soon in the actual MSHG setup.

Summarizing, we have identified the spin-flip scattering of hot electrons among spin-mixed states facilitated by a strong *e-m* interaction, as the responsible mechanism for the ultrafast loss of spin-polarization of the surface state on Gd(0001). The proposed demagnetization mechanism might be extended to even shorter time scales of the highly non-equilibrated electron bath since the measured spin polarization breakdown by MSHG takes place within the pulse duration of 35 fs (see figure 5.13).

### 5.2.2 Remagnetization dynamics on Gd(0001)

In the preceding section we have focused on the early time dynamics of the magnetization upon femtosecond laser excitation. The observed loss of magnetization (see figure 5.13) as measured by MSHG was on the 100 fs range. This partial (60 %) demagnetization of the system persists on a 40 ps time scale and it recovers the equilibrium magnetization value around 500 ps. The observed remagnetization process is studied in detail in this section.

Figure 5.18 illustrates the time evolution of the odd field together with the transients of even field $\Delta_{even}$ and the linear reflectivity $\Delta R/R$. The latter two quantities monitor the surface and bulk electron dynamics [44, 17, 70], respectively, and offer additional information that helps the interpretation of the observed transients. Upon laser excitation one observes rapid changes in all measured quantities. The sudden increase in the $\Delta_{even}$ and $\Delta R/R$ reflects the elevated electronic temperature reached after excitation through *e-e* scattering processes (see chapter 2). The hot electron population cools down to the lattice on a sub-picosecond time scale and a common temperature will be reached on a few picosecond range. The thermal gradient in the excited region will be spatially redistributed via thermal diffusion to the bulk of the sample and the substrate. Thus, the transients in $\Delta_{even}$ and $\Delta R/R$ during the 0.5 ns delay interval shown in figure 5.18, reflect the dynamics of lattice cooling in the laser spot region. One notices the difference between $\Delta_{even}$ and $\Delta R/R$ with the former one showing higher pump-induced variations and a quicker relaxation (steeper slope). This can be explained by the higher temperature reached in the surface layer (measured exclusively by $\Delta_{even}$) in comparison to deeper region of the excitation profile (measured by $\Delta R/R$). The more rapid cooling observed in nonlinear signal might also be ascribed to a different *e-ph* coupling at the surface than in the bulk. These points are not further develop here since they require more detailed investigations and are in the context of long-time magnetization behavior of minor importance.

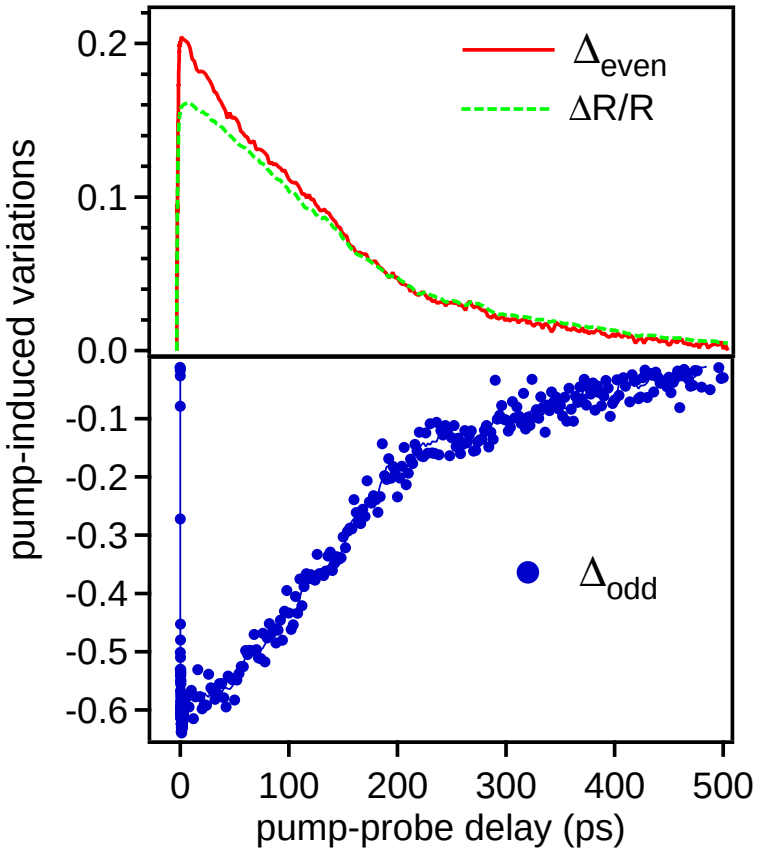


**Figure 5.18:** The pump-induced variations in the linear reflectivity (dashed curve), even (solid curve) and odd (dots) SH fields measured on a 20 nm Gd film at T=100 K.

Inspecting closely the odd field behavior in figure 5.18, one notice mainly three time scales: the one where the quasi-instantaneous breakdown is taking place (see preceding section), an intermediate one between 2-40 ps where $\Delta_{odd}$ levels-out to a constant value and a delayed, much slower one on hundreds of ps time interval, on which the equilibrium magnetization recovers.

On the last time scale 40-500 ps, we observe the remagnetization of the sample after the sudden photoexcitation. This process corresponds to the thermalization of the spin population and proceeds via coupling to the lattice [1, 81, 79]. This can be seen in the figure 5.19 where the transients in $\Delta_{even}$ and the scaled $\Delta_{odd}$ coincide starting to ≈150 ps. Since the even field monitors here the lattice cooling dynamics[11] and the odd field the magnetization of the system, one can conclude that at 150 ps the lattice and the spin systems reach a common temperature. The characteristic time of the energy transfer between the lattice and the spin system defines the so-called *spin-lattice relaxation* time

[11] As shown previously (see fig. 5.16 and fig. 2.7 ), around 1 ps the electrons and the lattice are equilibrated and the later dynamics represents the lattice cooling through thermal diffusion.

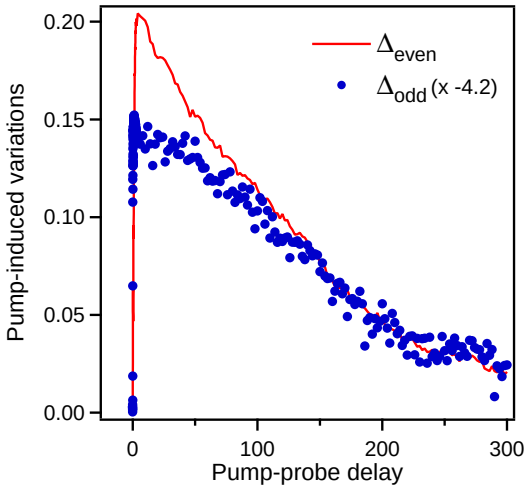


**Figure 5.19:** The same as in figure 5.18 but with $\Delta_{odd}$ (dots) inverted and normalized to $\Delta_{even}$ (solid line). From the crossing point of the measured transients a spin-lattice relaxation time $\tau_{s-l}$ of 150 ps is retrieved.

$\tau_{s-l}$, which is determined by the coupling strength between these baths. Hence, the measured spin-lattice relaxation time for Gd is ≈150 ps and it is in a good agreement with the earlier reported [79] $\tau_{s-l}$ of 100±80 ps measured with spin-polarized photoemission. Below 150 ps the magnetization recovery shows a slower dynamics than the lattice cooling, thus does not follow the classical M(T) behavior.
A possible interpretation might be as follows: in 100 fs after the excitation the spin-flip scattering of hot electrons produces magnons that introduces disordering of the $4f$ moments; after thermalization of the hot "source" of magnons (≈1 ps) the $4f$ moments remain in a disordered state and due to their localization *i.e.* less interaction with the surrounding energy baths, a slow relaxation[12] is encountered.

The spin-lattice relaxation process has been shown [1, 81, 91] to scale mainly with the magnetic anisotropy of the system and therefore to be mediated by the spin-orbit coupling. Such a process can be understood in the following picture: the electronic spin transfers energy and momentum to the orbit via spin-orbit coupling and the change in the orbital part of the wavefunction will be "see" it by the lattice via the produced fluctuation of the crystal field. For temperatures $T \geq 0.1 \cdot \Theta_D$ ($\Theta_D$ is the Debye temperature), the spin-lattice relaxation evolves via Raman-like scattering processes [1, 81, 135] between spin and phonons, where the spin is flipped by phonons and thereby accompanied by absorption and emission of phonons (like in the inelastic Raman scattering process).
Accounting for the measured magnetocrystalline anisotropy of 34.5 $\mu eV$ [139, 137] for bulk Gd and the extrapolated value [130] from thin films measurements that lies in the $\mu eV$ range, one obtains a spin-lattice relaxation value $\tau_{s-l} \sim E^{-1}_{anisotropy}$ around 2 ns. This time interval is one order of magnitude bigger than the measured relaxation time, which ask for an additional relaxation mechanism beside spin-orbit coupling. This last fact is not completely understood and further measurements are required. On a speculative level, one can involve the electron-magnon interaction which is specifically strong in gadolinium.

[12] The values of the exchange interaction constants $J_{4f-5d}$=94 meV, $J_{5d-5d}$=531 meV [138] and $J_{4f-4f}$=3 meV [105] give coupling times in the fs time range and thus can not be invoked here to explain such a slow dynamics.

In summary, from the remagnetization behavior on ferromagnetic Gd(0001) after laser excitation we could retrieve a spin-lattice relaxation time of $\tau_{s-l}$ of 150 ps, with the initial equilibrium magnetization of the surface being totally recovered after 500 ps. The slower magnetization relaxation than the lattice cooling below 150 ps has been ascribed to the localization of the $4f$ moments.

### 5.2.3 Conclusions

We have employed time-resolved magnetization-induced second-harmonic generation and photoemission measurements on the ferromagnetic Gd(0001) surface, in order to investigate the laser-induced demagnetization behavior of this material.

The main observations are that upon laser excitation an ultrafast breakdown (<100 fs) in the spin polarization of the surface state is taking place while its exchange splitting remains constant (in the investigated interval from 0–1 ps). Accounting for transient behavior of the surface state spin polarization and exchange splitting upon laser excitation, we could conclude that the Stoner model is inadequate for the ultrafast, non-equilibrium conditions and the measured data are well described in the framework of the spin-mixing model.

Based on these observations, we have identified the spin-flip scattering of hot electrons among spin-mixed states accompanied by magnons emission as the elementary spin-scattering process responsible for the ultrafast loss of magnetization on Gd(0001) surface. The suggested demagnetization mechanism is particularly efficient in Gd owing to its strong electron-magnon interaction.

On a longer time scale, we assist at the remagnetization of the system with a time constant of ≈150 ps that has been attributed to the spin-lattice relaxation. This has been concluded from the similarity between the transients of even SHG field and linear reflectivity (measures the electron/lattice dynamics) with the odd SHG field starting with this delay time.

## 5.3 Coherent optical phonons and magnons on Gd(0001) surface

This section presents the novel phenomenon of a coupled coherent phonon-magnon mode [17] measured at the ferromagnetic Gd(0001) surface by means of time-resolved MSHG. This coupled quasiparticle constitutes itself in new type of phonon-magnon interaction whose coupling is mediated by the exchange interaction. Moreover, the present study reports the first time observation of a *coherent optical phonon* on a metal surface.

### 5.3.1 Phonon-magnon coupling in equilibrium

The interaction between lattice and spins or between their quasiparticle excitations *i.e.* phonons and magnons is typically ascribed to spin-orbit coupling [81, 140]. Through the spin-orbit interaction the spin bath can relax to the surrounding lattice and thus has been considered as a major relaxation channel in ferromagnets since decades [135]. For the magnetic rare-earth elements, the evidence for the phonon-magnon interaction has been considered the appearance of energy gaps (or avoided crossings) in the magnon dispersion curves. These gaps have been observed [141] at the crossing points between the

unperturbed magnon and phonon dispersion curves (see the figure 5.20 for Tb). At this quasiparticle momentum, the eigenmode of the system has a mixed phonon-magnon character derived from the strong hybridization of the normal modes produced by the phonon-magnon interaction [142]. An illustrative case is *e.g.* Terbium which has eight electrons in the $4f$ shell and therefore a L=3 orbital contribution to the total magnetic moment. As it can be seen in the left part of the figure 5.20, along ΓA direction in the Brillouin zone, two gaps (denoted by $\Delta_1$ and $\Delta_2$ in the figure) show up in the magnon dispersion curve. Similar behaviors have been encountered also for dysprosium and $Tb_{0.9}Ho_{0.1}$ alloy [140]. No such an effect has been observed for Gd (see figure 5.20 right), which has L=0 and thus a weak spin-orbit coupling [137] coming from the valence electrons. By comparison of the dispersion curves for Gd and Tb, it has been concluded [141, 140, 142] that the observed energy gaps in the magnon dispersion curves ascribed to the phonon-magnon interaction are the effect of the spin-orbit coupling.

### 5.3.2 Coherent lattice and spin excitations

We have seen above that in equilibrated systems the phonon-magnon interaction is considered to be mediated by spin-orbit coupling. Here we propose a different type of magnetoelastic interaction between the phonons and spin waves, that relies on the modulation of exchange coupling strength $J$ with lattice vibrations.

Employing time-resolved magnetization-induced second-harmonic generation on the ferromagnetic Gd(0001) surface, a pronounced oscillatory contribution to the transient SHG signal has been observed [17] upon laser excitation. A typical example of such a measurement is displayed in the figure 5.21a, for a sample temperature of 90 K and a laser wavelength of 815 nm. The upper panel of the figure displays the time evolution of linear reflectivity $\Delta R/R$ and of the even SH field $\Delta_{even}$ while in the lower panel the transient odd SH field $\Delta_{odd}$ is shown. One notices immediately the conspicuous oscillatory component present in the transient SH fields while in the linear reflectivity, at the first glance, is not evident. Since $\Delta R/R$ does not show the oscillatory feature, the presence of the oscillations in the surface sensitive SHG signal points to the surface origin of the oscillatory pattern. Owing to the symmetry of the SH fields with respect to magnetization reversal [11], one has simultaneous access to the electron and lattice dynamics[13] described by the even field and to the surface magnetization monitored by the odd field (see chapter 3, section 5.1 and [17]). Thus, the observed oscillations describe a simultaneous, periodic modulation of the electron/lattice system and of the magnetization at the Gd(0001) surface.

The monotonous increase of the $\Delta R/R$ between 0-3 ps is ascribed to the hot electron temperature formation via *e-e* scattering (within 100 fs) and relaxation to the lattice through *e-p* scattering (up to 3 ps) of the system after laser excitation [17]. Such an incoherent behavior originating from electron and electron-phonon thermalization, is observed also in the $\Delta_{even}$ on which the oscillatory component is superimposed. Based on the similar incoherent contributions in $\Delta_{even}$ and $\Delta R/R$, the former one is also assigned to *e-e* and *e-p* scattering processes. The origin of the initial drop and the subsequent levelling

[13] Since any structural change of the lattice is reflected in the electronic structure of the system, the lattice dynamics is also measured by even SH field.

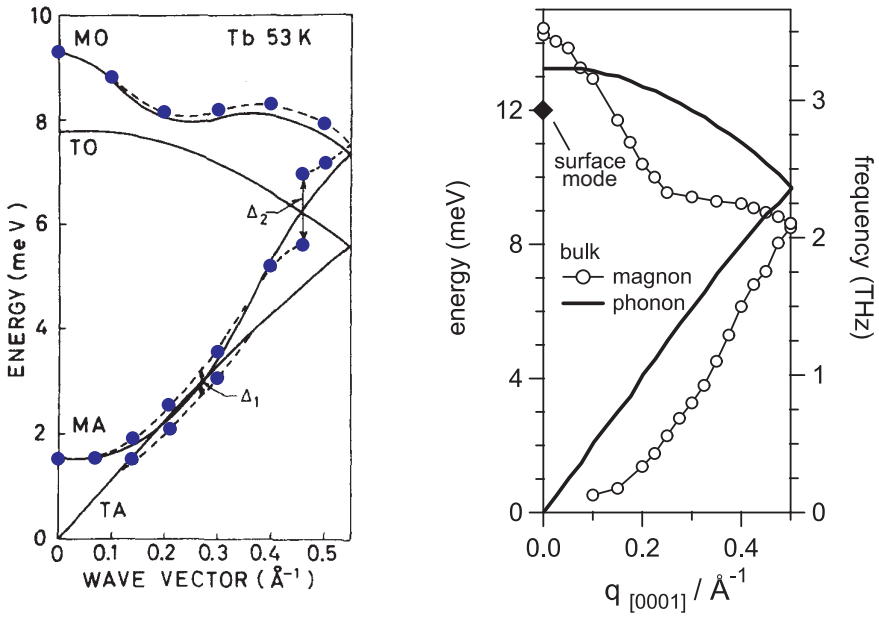


**Figure 5.20:** The dispersion curves for magnons (dots) (measured by neutron scattering) and phonons (lines) in Tb (left) and Gd (right) along $c$ axis. **Left:** The thin lines display the unperturbed dispersion curves by the presence of the phonon-magnon interaction. The latter one produces the splitting of the magnon dispersion curve by $\Delta_1$ and $\Delta_2$ energy intervals at the crossing points with phonon dispersions. MO and MA denote the optical and acoustical branches of magnon dispersion curves, respectively while TO and TA are the equivalents for the phonon branch. Adapted from [141]. **Right:** Dispersion curves for phonons (solid lines) as calculated by Rao and Menon [143], and magnons (dots) as measured by inelastic neutron scattering [144] in bulk Gd. At Γ point (q=0) the predicted phonon and magnon frequencies are 3.15 THz and 3.4 THz, respectively. The measured frequency of the coupled phonon-magnon mode at the Gd surface is depicted by the solid diamond. Note the lack of the energy gaps in the magnon dispersion curves for Gd due to its weak spin-orbit interaction (for details see text).

of the incoherent odd field has been detailed in the preceding section and is attributed to spin-flip scattering of hot electrons among spin-mixed states.

For the separation of the oscillatory and incoherent contributions to both SH fields the following procedure[14] has been used. An initial smoothing is done by fitting the original data with a polynomial function within a certain time window for consecutive time delays. The degree of the polynomial and the width of the time window is optimized by an autocorrelation criterion. The function 5.8, that simulates the oscillatory fraction of the signal, is subtracted from the smoothed data by adjusting $A$, $\tau$, $\Omega$ and $\varphi$ in order to minimize the oscillating component in the incoherent background. The obtained incoherent background $\Delta^{incoh}$ is subsequently smoothed and removed from the smoothed raw data, that renders $\Delta^{coh}$. The resulting oscillatory components $\Delta^{coh}_{even}$ and $\Delta^{coh}_{odd}$ are displayed in figure 5.21b. The frequency of the oscillation is retrieved from the Fourier transformation

[14]The data analysis procedure is presented in detail in appendix B.

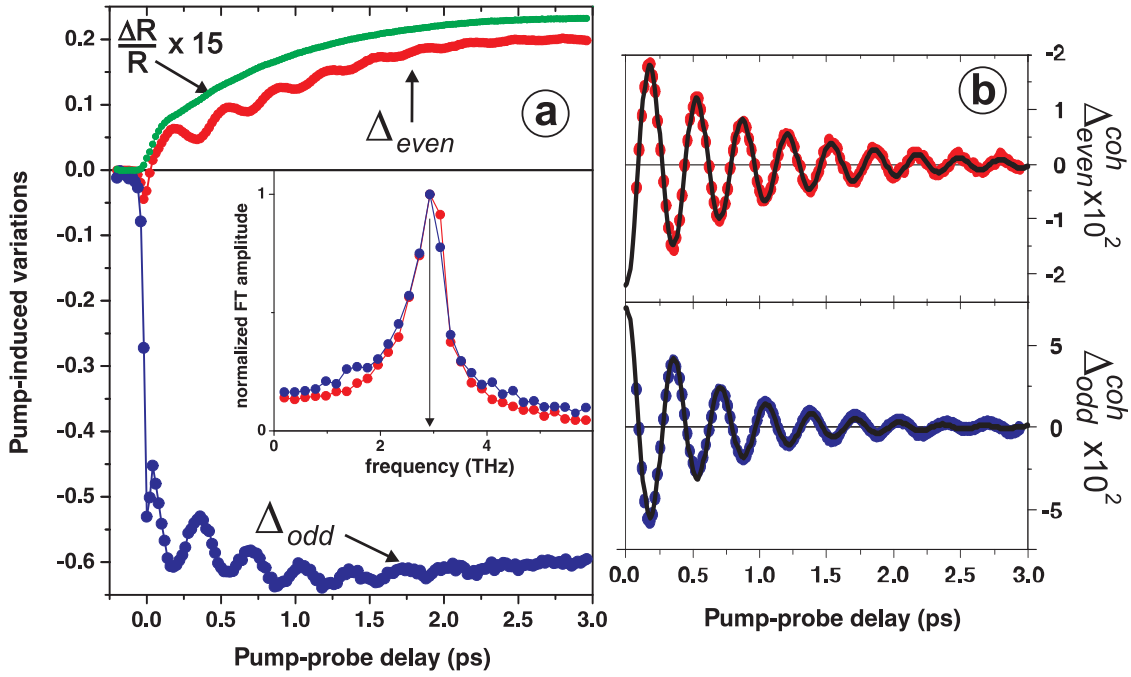


**Figure 5.21:** **(a)** Exemplary data set measured on Gd(0001)/W(110) at T=90 K and a laser wavelength $\lambda$=815 nm, showing the transient even (red curve), odd (blue curve) transient SH fields and linear reflectivity (green curve) behavior after laser excitation. For clarity $\Delta R/R$ is scaled by a factor 15. The pronounced oscillations in the transient SH fields are attributed to a coupled coherent phonon-magnon mode [17]. **(b)** Oscillatory component (dots) of $\Delta_{even}$ and $\Delta_{odd}$ obtained after removing the incoherent background (see text) together with the fitting curves (solid lines) according to eq. 5.8. The inset displays the Fourier transform of the $\Delta^{coh}_{even}$ and $\Delta^{coh}_{odd}$, that gives an identical frequency of 2.9±0.3 THz for both fields, as indicated by the arrow.

of the oscillatory signal, that is plotted in the inset of the figure. From here an identical frequency of 2.9±0.3 THz is observed for both fields, even and odd, that indicates the coupled nature of the oscillations. To analyze the transient oscillatory behavior, a fitting function that models an exponentially damped cosine-like oscillation has been introduced:

$$f(t) = Ae^{-t/\tau} \cdot \cos[2\pi(\Omega \cdot t + c \cdot t^2 + \varphi)] \tag{5.8}$$

where $A$, $\tau$, $\Omega$ and $\varphi$ represent the amplitude, decay time, frequency and the phase, respectively. Also a linear chirp of the frequency $c = \frac{1}{2}\frac{\partial\Omega}{\partial t}$ has been introduced in order to account for a possible frequency change in time. That such a chirp in frequency is indeed observed will be detailed in section 5.4. The fits of the oscillating SH fields according to eq. 5.8 are displayed in figure 5.21b as the solid lines.

In order to develop an understanding of the observed results let us have a look at the dispersion curves for phonons in bulk Gd as plotted in the right panel of figure 5.20. Here, the calculated phonon $E(q)$ spectrum (solid curve) [145, 143] predicts for the longitudinal-optical branch (LO) at $\Gamma$ point ($q$=0) a frequency of 3.15 THz. This value gives a reasonable good agreement with the phonon frequency of 2.9±0.3 measured at the surface in the

time-resolved experiment, since for a surface phonon mode one expects a lower frequency in comparison to the bulk value, due to the reduced coordination number. Consequently, we conclude that the observed modulations in the $\Delta_{even}$ are *coherent optical phonons* excited at the Gd(0001) surface. In the bulk, the LO phonon mode denotes the out-of-phase vibration of two hcp basal planes. By analogy, the longitudinal surface mode represents the vibration along surface normal of the topmost layer against the underlying bulk.

At this point we want to remark that the oscillatory part of $\Delta_{even}$ do not represent the real amplitude of the lattice vibration produced by the coherent phonon, which is measured in a time-resolved x-ray diffraction experiment. Here we measure the modulation of the $\chi^{(2)}$ (see eq. 2.18) determined by the coherent lattice oscillation via the electron-phonon deformational potential (see chapter 2). Therefore, further on, when refer to coherent phonon we understand the oscillatory component of the SH signal that arises from the coherent lattice motion.

The observation of a coherent optical phonon *on a metal* is a remarkable fact since such coherent lattice vibrations have been measured in semiconductors and semimetals only [15, 65, 68, 73, 77]. This can be attributed to the strong screening due to the high density of conduction electrons present in metals, that results in low efficiencies of coherent lattice excitation. The case of ferromagnetic Gd(0001) is special due to the presence of the spatially and energetically localized exchange-split surface state, through which the lattice vibration can be excited efficiently. Only very recently, Hase *et al.* [64] succeeded in detecting coherent optical phonons in hcp metals Zn and Cd employing high sensitivity LR detection.

Before explaining the coherence in the odd field, we focus on the excitation mechanism of the coherent optical phonon on the Gd(0001) surface. As reviewed in chapter 2, for the excitation of coherent phonons in THz frequency range two main mechanisms are invoked: impulsive stimulated Raman scattering (ISRS) and the displacive excitation of coherent phonons (DECP). The former one is mainly the inelastic Raman scattering effect under non-resonant excitation conditions encountered in transparent materials, whereas DECP triggers the coherent lattice dynamics under resonant excitation of the electronic population for opaque (absorbing) media. These two limits can be distinguished by considering the initial phase of the lattice oscillations: cosine-like for DECP and sine-like for ISRS (see figure 2.8).

In order to identify how one can excite coherent phonons on Gd and which is the involved excitation mechanism, we consider the pump-induced optical transitions via the specific electronic structure of Gd(0001) surface plotted in figure 5.11. The presence of the exchange-split surface state offers two excitation channels according to the spin orientation of the excited electrons. The majority channel that promotes an electron from the occupied surface state $S^{\uparrow}$ to unoccupied bulk states leaving behind a hole and the minority channel where the electrons are excited from bulk states to the unoccupied surface state $S^{\downarrow}$. Estimations of the lifetimes of the photoexcited electrons and holes are provided by STS measurements of the surface state components linewidth: at 80 K $\Gamma^{\uparrow}$=70 meV *i.e.* $\tau^{\uparrow} = \hbar/\Gamma^{\uparrow}$=9 fs for the hole and $\Gamma^{\downarrow}$=175 meV *i.e.* $\tau^{\downarrow}$=4 fs for the excited electron. Based on the asymmetric lifetimes of electrons and holes in the surface state one can develop the following scenario: the photoexcited hole in $S^{\uparrow}$ lives longer than the

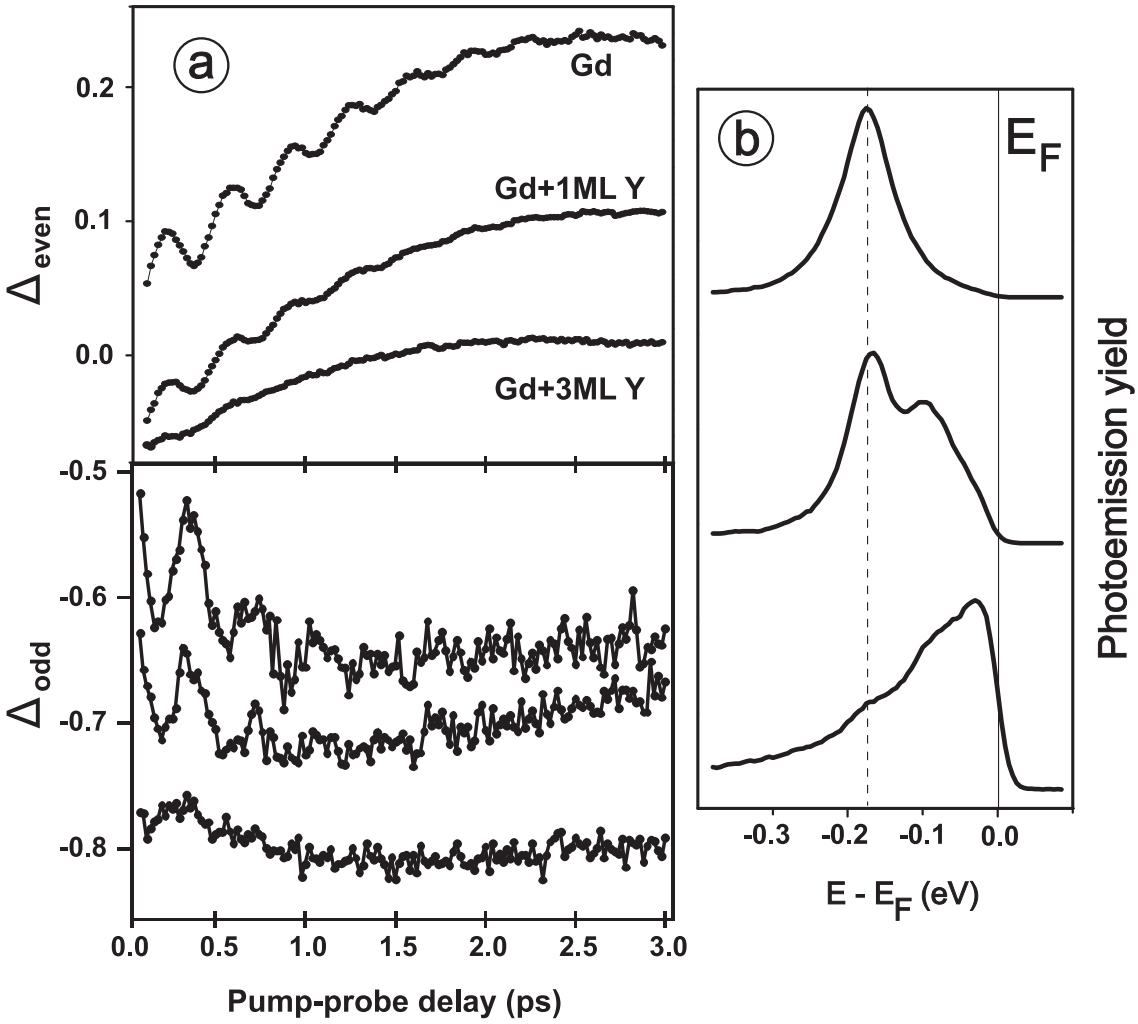


**Figure 5.22:** The influence of the Y adsorption on the coherent phonons dynamics at the Gd(0001) surface, as monitored by $\Delta_{even}$ and $\Delta_{odd}$ (a) and photoemission (b). Upon depositing 1 and 3 ML (nominally) of Y, the oscillation are gradually altered and eventually quenched in both transient SH fields. This behavior corresponds, according to the photoemission data, to an initial broadening of the surface state with an additional shoulder peak from Y surface state for 1 ML of Y, and to a suppression of the Gd surface state for 3 ML of Y. The photoemission measurements have been performed by O. Krupin (within the collaboration with our group [17]) under comparable conditions at BESSY light source with a photon energy of 36 eV at normal incidence. The $\Delta_{odd}$ curves are offset it for clarity.

excited electron in the $S^{\downarrow}$ and therefore an ultrafast charge redistribution take place at the surface in order to screen the photo-hole. This is equivalent with a modification of the equilibrium potential of the surface ions cores, that will try to restore the equilibrated potential by a collective ion movement to a new lattice coordinate. This will establish a new potential energy surface with a changed equilibrium position with respect to the equilibrium case. Due to availability of scattering channels typical for metals, the charge imbalance at the surface decays on a 10 fs time scale leaving the surface ions displaced. Such a sudden lattice displacement is the initial trigger of the coherent lattice oscillations.

From the above considerations we have seen that the presence of the exchange-split surface state plays a major role in the excitation of the coherent lattice motion. As a check of the excitation mechanism, we have performed an overlayer experiment where the 20 nm Gd film was covered with a thin layer of yttrium (Y). The hcp Y metal is non-ferromagnetic, has the same valency and almost the same lattice constant (lattice mismatch 0.5%) as Gd. It exhibits also a $d_{z^2}$-like surface state positioned at the Fermi level that is not exchange-split (see figure 6.6). Thus yttrium is a good candidate for the controlled modification of the Gd surface state. Covering the Gd surface with various Y layer thicknesses the exchange splitting of the Gd(0001) surface state should be affected and eventually quenched, whereas the Y(0001) surface state should remain. The idea is to demonstrate that the existence of an exchange-split surface state is the necessary condition for the coherent phonon excitation. The effect of Y deposition on the lattice vibrations is depicted in figure 5.22. Upon one monolayer (nominally) Y coverage the amplitude of the oscillations in $\Delta_{even}$ is drastically reduced and after three ML the oscillations are barely visible. Similar transients are encountered for the oscillatory $\Delta_{odd}$ behavior with a clear oscillatory signature for pure Gd and a decreasing amplitude upon Y absorption. Photoemission measurements performed with a 36 eV beam energy under comparable conditions [17], show the presence of the surface state for clean Gd(0001), a modified Gd surface state with an additional peak from Y at a coverage of 1 ML of Y, and quenching of Gd surface state at three ML Y coverage. Therefore, we have unambiguously demonstrated that the excitation of the coherent phonons at the Gd(0001) surface is conditioned by the presence of the *exchange-split* surface state. A non-split state at the surface, as is the case for Y(0001), is obviously not leading to excitation of the coherent mode. From this observation we conclude that two excitation channels are required. Later in section 5.5 it will be discussed that different probabilities for excitation of both channels are likely to be responsible for the excitation of the coherent phonon-magnon mode at the Gd(0001) surface.

Coming now to the periodic modulations in the magnetic signal, we see that the Fourier transformation of the oscillatory SH fields (5.21 inset) gives an identical frequency for odd and even fields, whereas in the time-domain a phase shift of $\pi$ is encountered between their oscillatory transients (see figure 5.21b). Furthermore, there is no evidence for the existence of a build-up time in the $\Delta_{odd}^{coh}$ behavior, which means that the coherent spin excitation follows the lattice instantaneously. All these facts give evidence for coupled lattice and spin oscillations with a common origin, that proceed simultaneously after excitation, and thus a strong interaction should mediate their coupling. Now the major question that arises is: what kind of interaction determines the coupling ?.

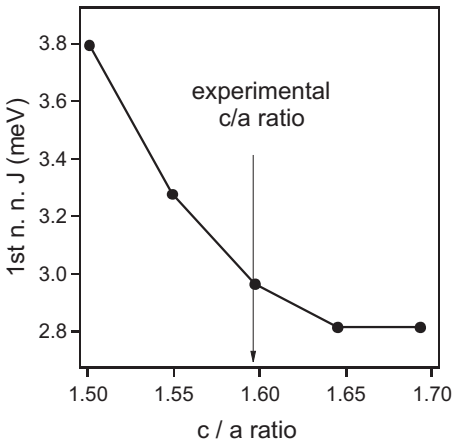


**Figure 5.23:** Density functional theory (DFT) calculations of the exchange interaction strength $J$ between nearest neighbors atoms for bulk gadolinium as a function of $c/a$ ratio, performed by Turek *et al.* [105]. Decreasing and increasing of the $c/a$ ratio (with $c$=2·$d_{12}$) determines an increase and decrease of $J$, respectively. The experimental $c/a$ ratio value in bulk Gd is indicated by the arrow.

One can address this questions starting from the phonon-magnon interaction in equilibrium. As has been described at the beginning of this section, the spin-orbit coupling is considered responsible for the interaction between spin and lattice. Bulk gadolinium exhibits a weak spin-orbit coupling that amounts to 16 $\mu eV$ as calculated by Colarieti *et al.* [137]. Transforming this value in time units one ends up with a time scale of ≈4 ns that is four orders of magnitude slower than the encountered sub-ps lattice and spin dynamics dynamics. Therefore, one can be very confident in excluding the spin-orbit coupling as being responsible for the observed dynamics.

As a possible mechanism that mediates the coupling between the lattice and spins, we propose the exchange interaction $J$. $J$ depends on the wavefunction overlap between nearest neighbor atoms and thus might exhibit also the dependence $J = J(d_{12})$, where $d_{12}$ is the interlayer distance $d_{12}$. The dependence of the exchange interaction on the $c/a$ ratio ($a$ and $c$=2·$d_{12}$ are the hcp lattice constants) and implicitly on the interlayer distance $J = J(d_{12})$ has been calculated for bulk gadolinium, using density functional theory (DFT), by Turek *et al.* [105]. At the surface, due to the $d_{z^2}$ orbital symmetry of the surface state (see figure 2.3), the exchange interaction along $z$ axis will depend sensitively on the variation of the interlayer distance $d_{12}$. Thus any variation $\delta$ in the interlayer distance $d_{12} \pm \delta$ due to the coherent lattice vibration will be reflected in magnitude of the exchange interaction. As illustrated in fig. 5.24, the $J$ will increase or decrease with an amount $\delta J$ as the $d_{12}$ is larger or smaller relative to its value in equilibrium. The variation of the interlayer distance determines the appearance of a lattice strain, that has been shown to strongly affect the energetic position of surface states [146, 147, 148]. Thus, the lattice vibrations will be sensitively monitored by SHG signal since the SHG process evolves resonantly enhanced via the surface state. Another consequence of $J = J(d_{12})$ is the variation of the local magnetic ordering at the surface in parallel with the change in $d_{12}$. This affirmation is based on the Heisenberg model picture (see eq. 2.1) where the relative orientation of two nearest neighbors spins is determined by the sign and magnitude of the exchange interaction $J$. Such a periodic variation of the surface magnetic ordering is detectable with the transient odd SH field. Indeed, we observe periodic oscillations in the $\Delta_{odd}$, which corroborates this scenario. Thus, the exchange interactions seems to be the appropriate lattice-spin coupling mechanism since it is sensitive to changes in both

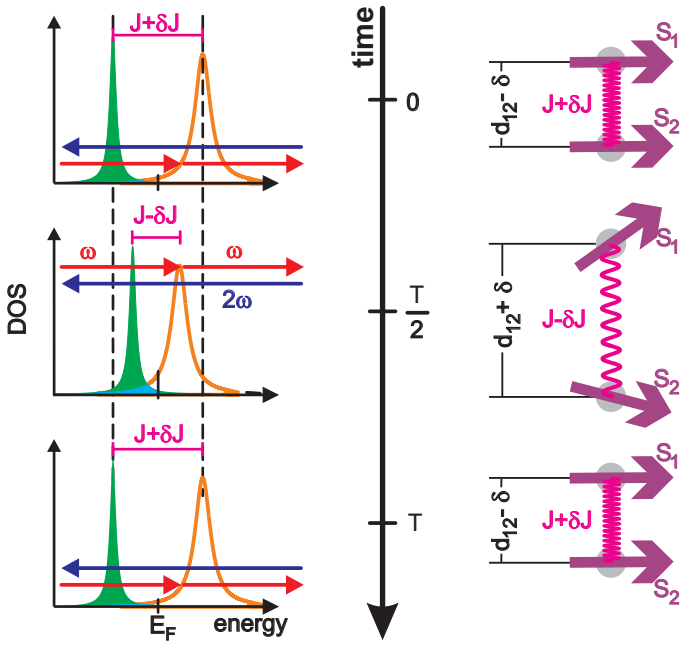


**Figure 5.24:** Schematic illustration of the coupling mechanism between lattice and spins oscillations within one oscillation period. At t=0 the lattice is contracted by an amount $\delta$ that increases the exchange interaction by $\delta J$ (see fig. 5.23), which results in an increased exchange splitting of the surface state and thus the SHG resonance enhancement via the surface state is less fulfilled. This explains the initial phases of the oscillatory lattice and spin coherence that show a minimum and maximum (fig. 5.21b), respectively. At t=T/2 the lattice is expanded, the $J$ is decreased which means that $\Delta_{ex}$ is decreased and the resonance enhancement is better fulfilled *i.e.* the coherent phonon shows a maximum while the spin oscillation shows a minimum. This scenario is repeated until the oscillations are damped.

subsystems. In how far will explain the observed phenomena is described in the following.

From the calculated dependence of $J$ on the $c/a$ ratio plotted in the figure 5.23, we notice an increasing magnitude of $J$ with decreasing interlayer distance due to a better wavefunction overlap. Based on these facts one can suggest the following coupling mechanism. The coherent phonon excited at the surface produces periodical variations of the interlayer distance $d_{12}$, which will modulate the exchange interaction strength according to $J = J(d_{12})$. Hence, the degree of magnetic ordering at the surface (*i.e.* magnetization) determined by the magnitude of $J$, will also oscillate concomitant with the lattice vibration. In the same time, the modulations of $d_{12}$ will build-up a periodically varying lattice strain that will periodically shift the surface state peak positions and implicitly modulates its exchange splitting *i.e.* a 'breathing' surface state. This scenario is depicted in figure 5.24 showing the presumable dynamics of $J$ between two magnetic moments in adjacent layers and of the surface state exchange splitting $\Delta_{ex}$ over one coherent phonon period. From the extrapolated phase to t=0 of the oscillatory component in SH fields (see figure 5.21b), one notices that $\Delta^{coh}_{even}$ starts with a minimum while $\Delta^{coh}_{odd}$ shows a maximum. The maximum in $\Delta^{coh}_{odd}$ reflects a better magnetic ordering and thus an increase of the exchange

coupling $J + \delta J$. The increased $J$ has been ascribed [105] (see fig. 5.23) to a compressive strain of the lattice *i.e.* the interlayer distance is decreased $d_{12} - \delta$. Also, the bigger the magnitude of $J$, the larger is the exchange splitting of the surface state and therefore less fulfillment of the SHG resonance condition, explaining the minimum in the $\Delta^{coh}_{even}$. At the half-period (the second instance in the figure), $\Delta^{coh}_{even}$ is maximum whereas $\Delta^{coh}_{odd}$ exhibits a minimum. Now the lattice suffers a tensile strain *i.e.* the interlayer distance is increased $d_{12} + \delta$ that results in a smaller exchange coupling $J - \delta J$ (produces minimum in $\Delta^{coh}_{odd}$) and thus a smaller exchange splitting of the surface state. The resonance enhancement via the surface state is better fulfilled and therefore one encounters a maximum in $\Delta^{coh}_{even}$. These sequential time-frames are repeated along the oscillatory transient and eventually damped after a time interval of ≈3 ps.

The proposed model connects the lattice vibrations and the modulation of the surface magnetization via the exchange interaction $J$. Since the magnetization follows the lattice instantaneously (no build-up time in $\Delta^{coh}_{odd}$ observed within our time resolution of 35 fs), $J$ should provide a very strong interaction. This is indeed the case, with values for the intra-atomic exchange coupling $J_{4f-5d}$=94 meV and $J_{5d-5d}$=531 meV [138] that are much higher than the 12 meV energy of the coupled phonon-magnon mode, determined from the its measured frequency of 3 THz. The time equivalents of $J_{4f-5d}$ and $J_{5d-5d}$ are 6 fs and 1.2 fs, respectively. These values are smaller than our time resolution of 35 fs (laser pulse duration), which means that they provide a quasi-instantaneous coupling with regard to the experimental time resolution. Therefore, we can explain the quasi-instantaneous excitation of the lattice and spin coherence that proceed simultaneously within the time resolution of our experiment.

In the above considerations we have mentioned the exchange coupling constants between the $4f$ and $5d$ as well as $5d$ and $5d$ electrons. Accounting for their magnitude, both could explain the quasi-instantaneous coupling between lattice and spin excitations. Therefore the following question arises. What represents the periodic modulation of magnetization measured by the odd field – the oscillatory magnetic ordering of the $4f$ or the $5d$ magnetic moments? The MSHG measures the dynamics of the $5d$ valence electrons within the achievable spectral range between 1.48 - 1.7 eV. The $4f$ levels have a binding energy of ≈9 eV [31] and thus are not directly accessible with the available laser photon energy. On the other hand, the dominant contribution to the SHG response on Gd(0001) comes from the exchange-split surface state whose energy splitting reflects the magnitude of the $4f$ moments [31, 30]. An oscillating exchange splitting (see fig. 5.24) will affect the orientation of the $4f$ due to the strong $J_{4f-5d}$ coupling between the surface state ($5d_{z^2}$ character) to the $4f$ electrons. Hence, a very plausible scenario is that the $4f$ moments will also oscillate with the same frequency as the lattice vibrations. Since we measure the dynamics of the $5d$ electrons and we have strong indications that the $4f$ moments are also involved in the observed coherent phenomenon, we conclude that the oscillations in the odd SH field represent the coherent modulation of the total magnetic moment in Gd.

Inelastic neutron scattering that measures directly the magnetic moments (the major contribution coming from the $4f$ moments in Gd case) of a ferromagnetic sample, gives for bulk Gd[15] [144] at Γ point a magnon frequency of 3.4 THz, as can be seen in figure 5.20.

[15]To the best of author's knowledge, there are no reported measurements of the phonon and magnon

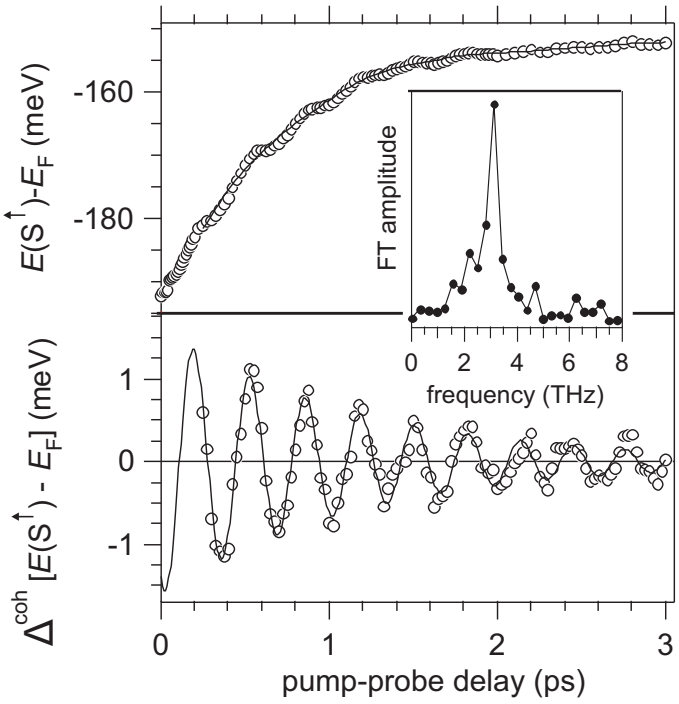


**Figure 5.25:** Time-resolved PE measurement of the $S^{\uparrow}$ surface state binding energy on the Gd(0001) surface at T=40 K. Upper panel: the transient behavior of the $S^{\uparrow}$ binding energy exhibits a continuous shift towards $E_F$ modulated by an oscillatory component. Lower panel: the oscillatory fraction of the binding energy (dots) obtained after subtraction of the incoherent part fitted (solid line) according to eq. 5.8. In the inset the Fourier transformation of the oscillatory signal gives a central frequency of 3.1±0.2 THz. From [150].

Considering the lower coordinate of surface atoms such a value gives a good agreement with the observed frequency of 2.9±0.3 THz. Moreover, we can argue that a lower frequency is required since an overlap of the surface phonon and magnon frequencies is a necessary condition in order to observe a coupled mode. Therefore, the magnon dispersion curves further support the idea of a coherent magnon involving the $4f$ moments.

As mentioned earlier for the coherent phonons, the SHG measures the modulation of the magnetic susceptibility and not the magnons as *e.g.* the neutron scattering does. Therefore, when mentioning coherent magnons we have in mind the oscillatory $\Delta_{odd}$ component.

To unambiguously proof the dynamics of the 4f moments it would be required to measure them directly with femtosecond resolution involving UV or x-ray UV sources from free-electron lasers or high-harmonics in rare-gas cells [149]. Also it would be interesting to perform a time-resolved x-ray magnetic circular dichroism (XMCD) experiment, that would monitor simultaneously the dynamics of the orbital and spin contributions to the total magnetic moment.

An independent experimental check for the proposed coupling mechanism has been done, within our lab, by time-resolved photoemission measurements of the Gd(0001) $S^{\uparrow}$ surface state component. These measurements have been performed by my colleagues P. Loukakos and M. Lisowski [150]. The experimental apparatus and conditions are identical with the one presented in section 5.2.1 except the sample temperature that is lower ≈40 K. Figure 5.25 shows the transient behavior in the binding energy of the majority surface state component. We observe a monotonous shift of the $S^{\uparrow}$ binding energy towards $E_F$ as a function of pump-probe delay, that is modulated by an oscillatory component with a

dispersions at the Gd surface.

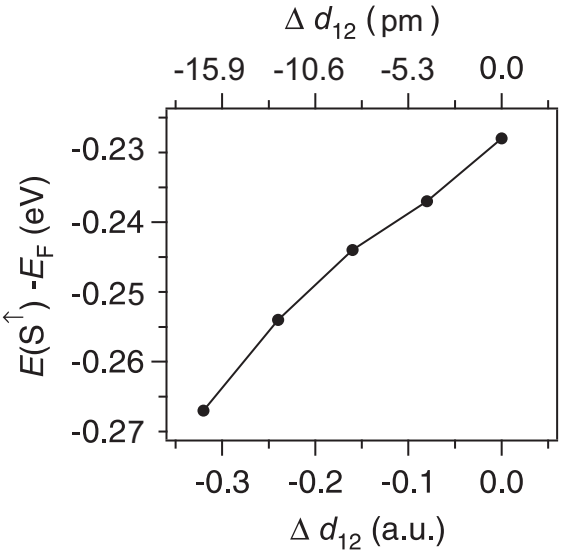


**Figure 5.26:** DFT calculation of the energetic position dependence of the $S^{\uparrow}$ surface state component on the contraction of the interlayer distance $d_{12}$ between two adjacent layers at the Gd surface [151]. Upon compressive strain the $S^{\uparrow}$ binding energy is shifting away from the Fermi level. $\Delta d_{12}$ is given in atomic units and the equivalent in pm (upper scale) with zero value corresponding to equilibrium interlayer distance.

period of ≈ 330 fs. After the substraction of the incoherent background as has been done for the SH fields, one obtains the oscillatory contribution plotted in the lower panel of the figure 5.25. The result of Fourier transformation displayed in the inset of the figure, gives a central frequency of 3.1±0.2 THz that is in a very good agreement with the frequency measured by MSHG. Note that the required energy resolution in binding energy changes is ≈1 meV, which has not been achieved for the unoccupied $S^{\downarrow}$ component. Therefore, the suggested model of oscillating binding energy of the surface state with the lattice vibration, firstly proposed accounting only for the nonlinear optical measurements [17], is confirmed (at least for the $S^{\uparrow}$ component).

A theoretical support of the proposed coupling mechanism comes from the DFT calculations performed by Blügel and coworkers [151]. They computed the change in the binding energy of the surface state due to a compressive lattice strain. The result for the majority surface state component is depicted in the figure 5.26. Upon a lattice contraction the $S^{\uparrow}$ energetic position is shifted to lower binding energies. Based on this calculations one can evaluate the variation in the interlayer distance produced by the coherent phonon oscillation. Fitting the oscillatory binding energy data from figure 5.25 with the eq. 5.8, one obtains an initial amplitude (t=0) of 1.6 meV. According to the figure 5.25 this value corresponds to a contraction of 70 pm that represents 0.24% from the equilibrium $d_{12}$=2.89Å [25] interlayer distance. Thus the observed oscillations represent a modulation of the interlayer distance of less than 1%.

### 5.3.3 Conclusions

Employing the pump-probe MSHG technique on the Gd(0001) surface we have observed coupled coherent lattice and spin excitations evolving with a common frequency of 2.9 THz. This has been deduced from the pronounced oscillatory features present in the SH fields, which measure simultaneously and separates the electron/lattice and spin dynamics owing to the symmetry of these fields with respect to magnetization reversal. A very re-

markable fact is that we measure for *the first time the presence of coherent optical phonon on a metal*. The excitation of the coherent phonon is attributed to the asymmetric excitation of the surface state components which produces an ultrafast charge redistribution at the surface that suddenly displaces the surface ions potential and sets the surface atoms into an oscillatory motion. From the initial cosine-like phase of the coherent phonons and taking into account that is a charge-driven coherent lattice vibration we identify the excitation mechanism as being DECP-like. The coupling between the lattice vibrations and the spin system is determined by a dynamic variation of the exchange interaction strength $J$ with the interlayer distance $d_{12}$. The magnitude of $J$ explains the observed quasi-instantaneous coupling between phonons and magnons. This type of coupling represents a new, dynamical interaction mechanism between phonons and magnons. The proposed excitation mechanism deduced from MSHG data, has been confirmed by TRPE measurements of the surface state binding energy. In time-resolved photoemission, a periodic modulation of the $S^{\uparrow}$ surface state binding energy has been observed having the same frequency as the coupled phonon-magnon mode measured with MSHG.

## 5.4 Coherent surface and bulk lattice vibrations on Gd(0001)

In the preceding section, the *surface* coherent phonon-magnon mode has been studied in detail by investigating its origin, excitation mechanism and the coupling between lattice and spin excitations. Since the coherent phonon mode corresponds to the vibration of the surface layer against the underlying bulk, the question arises whether the bulk phonon modes are also excited. This subject is investigated using the time-resolved linear reflectivity and second-harmonic generation techniques, and is presented in the following section.

### 5.4.1 Results

Inspecting the Gd phonon dispersion curves in the figure 5.20, one observes that the frequency of the measured surface phonon mode of 3 THz is laying in the proximity of the bulk mode with 3.14 THz at q=0. This suggests that the surface mode can, in principle, couple to the adjacent bulk layers and trigger an oscillatory motion of bulk atoms. The existence of bulk phonons in Gd(0001) after photoexcitation has been addressed employing the pump-probe linear reflectivity (LR), that is a bulk sensitive technique within the optical penetration depth[16] (here $\delta \approx$20 nm). Simultaneously, the SHG response has been measured that reflects the surface phonons dynamics. Hence, by the use of both techniques one can measure and separate the bulk and surface behavior.

Such a combined measurement performed at T=90 K is presented in the figure 5.27. In the upper side of the figure the measured transient dynamics of the even SHG ($\Delta^{2\omega}$) and linear reflectivity ($\Delta^{\omega}$) fields is displayed. $\Delta^{\omega}$ is defined as $\sqrt{\frac{I^{\omega}(t)}{I^{\omega}(t_0)}} - 1 \approx \frac{1}{2}\frac{I^{\omega}(t)-I^{\omega}(t_0)}{I^{\omega}(t_0)}$ where $I^{\omega}(t)$ and $I^{\omega}(t_0)$ denote the reflected intensities for positive and negative pump-probe delays, respectively. In the SHG signal pronounced oscillations are present while

[16] The literature data regarding the imaginary part of the refractive index $k$ at $\lambda$=800 nm are very scattered, ranging from 1.55 to 3.46 that give optical penetration depths $\delta = \frac{\lambda}{4\pi k}$ from 41 nm to 18 nm. [152]

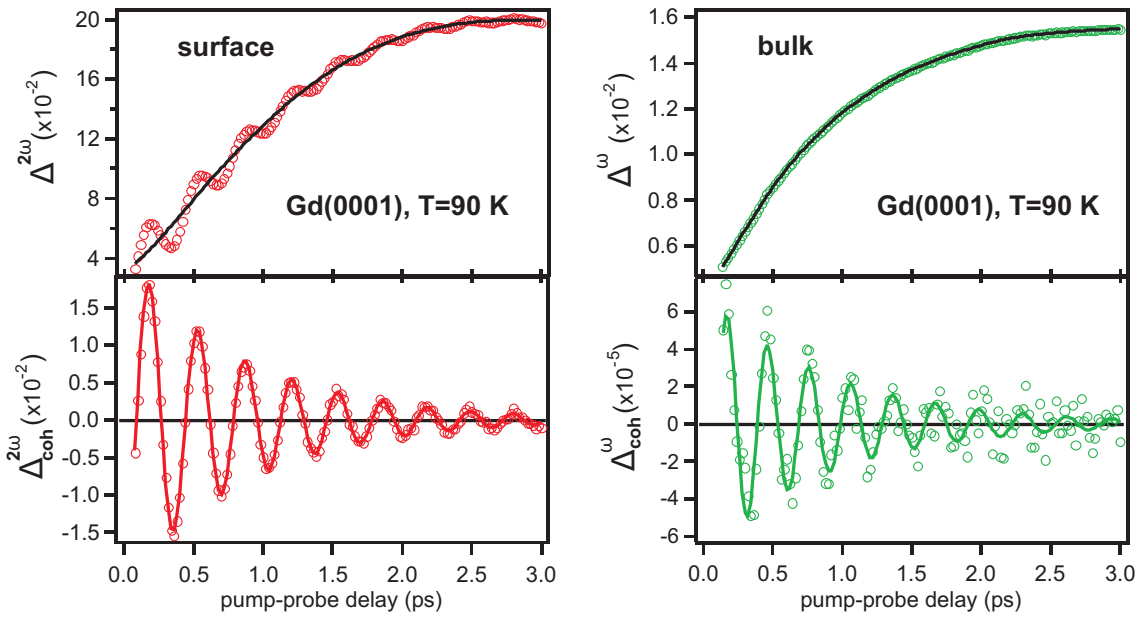


**Figure 5.27:** Laser-induced dynamics on the Gd(0001) sample at T=90 K as measured with second-harmonic generation (left) and linear reflectivity (right). After removing the incoherent contributions (black solid lines) to the raw signal in both data sets, the coherent oscillatory fraction is obtained as displayed in the lower part of the figure. Note the three orders of magnitude difference between the amplitude of the oscillatory SH and linear reflectivity signals, that explains the less evident modulations in the LR raw signal.

in the pump-induced variations of LR, although weak, are also visible. After removing the incoherent background (the solid lines) as has been described earlier (section 5.3), the oscillatory fraction is obtained, which is plotted in the lower part of the figure 5.27. Now one can clearly notice the existence of an oscillatory component in the linear reflectivity, whose amplitude is in the $10^{-5}$ range *i.e.* three orders of magnitude smaller than the oscillations $\Delta^{2\omega}_{coh}$ in the SH signal. This explains why its presence is not so evident in the raw LR signal. Based on the bulk sensitivity of the linear reflectivity, we ascribe the oscillatory signal measured by LR to *coherent bulk phonons* in the Gd(0001) sample.

Performing the Fourier transform of the oscillatory signals displayed in figure 5.28, one obtains two different central frequencies of 3.3±0.1 THz and 2.9±0.1 THz for bulk and surface phonons, respectively. First, the dissimilar frequencies of the phonon modes indicate that they originate from different environments *i.e.* bulk and surface. Hence, one can assign the measured frequency difference to the different coordinate number encountered at the surface (9) with respect to bulk (12) *i.e.* the chemical bonding is stronger in the bulk than at the surface, that yields a higher frequency for the latter one. The Fourier spectra in the figure 5.28 exhibit asymmetric peak shapes towards higher and lower frequency for the bulk and surface phonon mode, respectively. As will be shown in the following, this asymmetry can be related to a dynamical change of the frequency *i.e.* a frequency chirp. Such a behavior has been reported in literature [153, 154, 155, 156] for bulk coherent phonons in semimetals and semiconductors. This has been ascribed to anharmonic

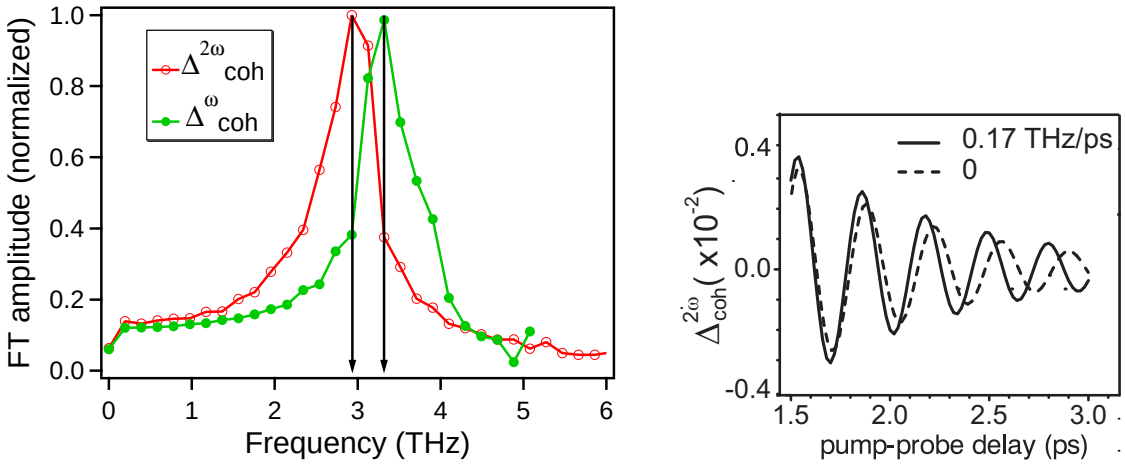


**Figure 5.28: Left** The Fourier transformation of the oscillatory signals measured in SHG ($\Delta^{2\omega}_{coh}$) and LR ($\Delta^{\omega}_{coh}$) that give a frequency of 2.9 THz and 3.3 THz for surface and bulk phonons, respectively. The measured frequencies are indicated by the arrows. Note the asymmetric peak shapes which indicate a time-dependent frequency change. **Right** The oscillatory SH field plotted with and without a linear frequency shift. The measured data could be fitted properly only incorporating a frequency chirp, in this case of 0.17 THz/ps.

effects of the vibrational potential and/or to electronic softening of the inter-atomic bond strength under the effect of excited carriers [157].

In order to clarify the origin of the asymmetric shape of the Fourier spectra and of the opposite broadening for bulk and surface phonons, we have employed two methods to analyze the frequency evolution in the time domain. The first one is based on the phenomenological model of an exponentially damped oscillator defined in the eq. 5.8. In this expression the term $c = \frac{1}{2}\frac{\partial\Omega}{\partial t}$ describes a linear chirp of the frequency, which was necessary to be introduced in order to describe the oscillatory data for time delays $> 1.5$ ps. A comparison between the data with and without chirp for the $\Delta^{2\omega}_{coh}$ is plotted in figure 5.28. The fitting curves of the oscillatory signal according to 5.8 are plotted as solid lines in the lower part of the figure 5.27. The obtained values for the frequency, chirp and delay time from the fit are $\Omega_s$=2.8±0.05 THz, $c_s$=0.17±0.01 THz/ps, $\tau_s$=0.86±0.02 ps for the surface mode while for the bulk phonons $\Omega_b$=3.44±0.05 THz, $c_b$=-0.12±0.05 THz/ps, $\tau_b$=0.9±0.01 ps. The values and the signs of the chirp parameters give a quantitative evaluation of the observed asymmetric Fourier spectra, and confirm also their opposite broadening tendency. Plotting the time-dependence of the frequency chirp, as shown in the figure 5.29, we note that they cross each other around 2 ps delay time. This interesting feature will be detailed in the following.

The second analysis method has been employed in order to obtain further insight in the phonon dynamics, and evaluates the instantaneous values of frequency and amplitudes. For this purpose the following fit function has been used:

$$\Delta_{coh}(t') = \left[A(t) + \frac{\partial A(t)}{\partial t}(t - t')\right] cos[2\pi(\Omega(t)t' + \varphi(t))] \tag{5.9}$$

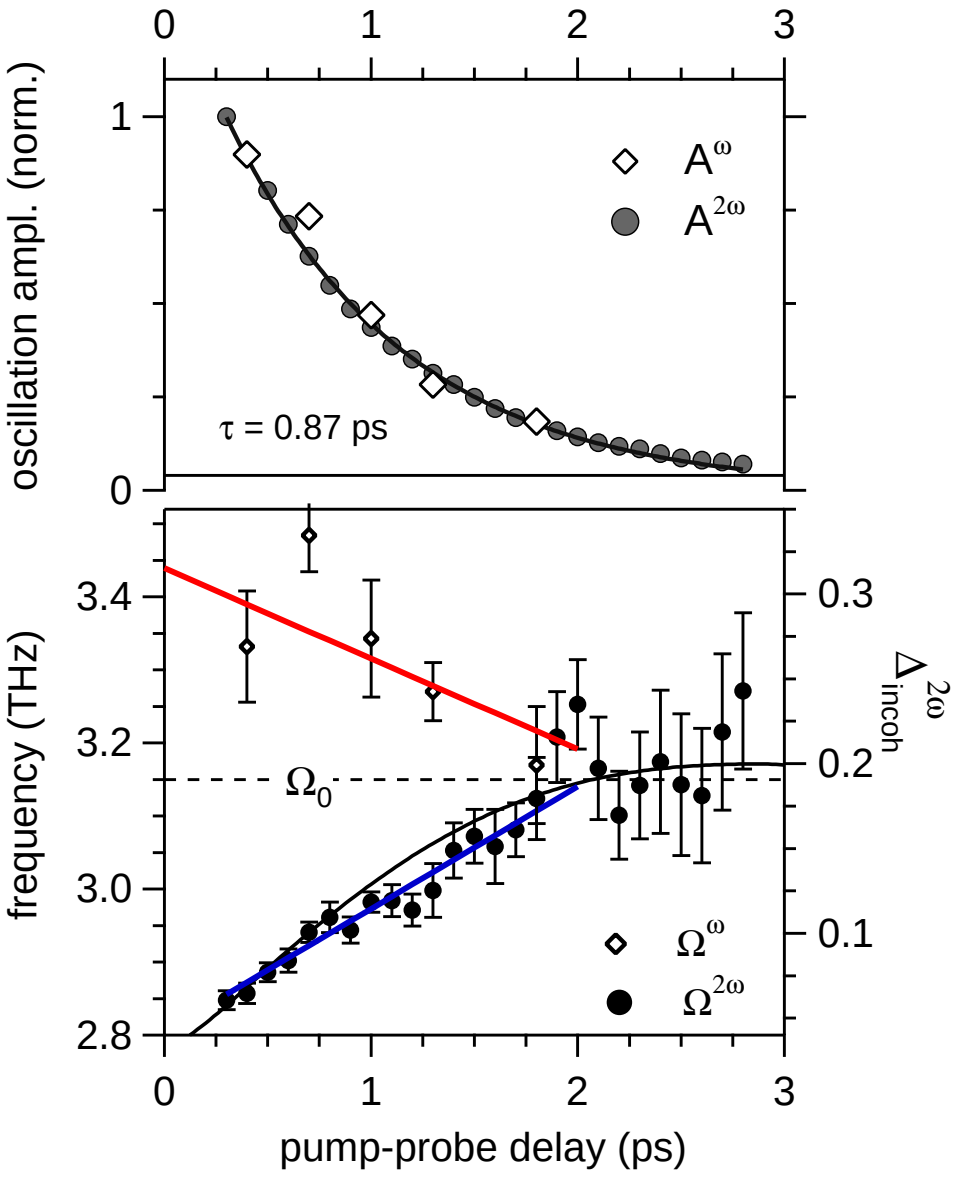


**Figure 5.29:** The time evolution of the instantaneous amplitudes (top) and frequencies (bottom) of the bulk and surface coherent phonons obtained by fitting the oscillatory components of LR and SHG with the expression 5.9. **Top** The bulk and surface coherent phonons amplitudes denoted by $A^{\omega}$ and $A^{2\omega}$, respectively, decay exponentially with the same time constant $\tau$=0.87 ps. **Bottom** The transient frequency values of the bulk and surface phonon modes exhibit an opposite frequency chirp showed by the red and the blue lines: redshift for bulk phonons and blueshift for surface phonons. The frequency change of both modes reach a common level, denoted by the dashed line, at a frequency value $\Omega_0$=3.15 THz and around 2 ps delay time. This delay coincides with the *e-p* equilibration as deduced from the saturation of the incoherent SHG signal (solid line) $\Delta^{2\omega}_{incoh}$.

The analysis procedure has been carried out as follows. Within a time window of 0.4 ps centered at time $t$, that is shifted in steps of 0.1 ps along the pump-probe delay, the oscillatory signal is fitted with $A$ and $\Omega$ as adjustable parameters. The values of $\frac{\partial A}{\partial t}$ and $\varphi$ are determined by the $A$ and $\Omega$ from the previous and actual fitting frame. The resulting values for the instantaneous frequency and amplitude are displayed in figure 5.29. The frequency of the *surface* mode shows a monotonous increase with time *i.e. blueshift*, that goes along the extrapolated values of the linear chirp obtained from the previous fitting procedure. For the *bulk* mode, despite of the lower statistics, we observe a clear decrease in the frequency *i.e. redshift*, following the linear chirp values. Both data sets are merging to a common point around 2 ps, that corresponds to a frequency value of 3.15 THz, indicated in the figure 5.29 by the dashed line. This value agrees well with the calculated [143] frequency of the bulk LO phonon mode $\Gamma_{3^+}$ in gadolinium at the $\Gamma$ point.

Summarizing the experimental data, we measure the presence of oscillatory components in the pump-induced variations of the SHG and LR signals whose relative magnitude is in the $10^{-2}$ and $10^{-5}$ range, respectively. They exhibit different initial frequencies that amounts to 3.4 THz for bulk and 2.8 THz for the surface mode. We observe a changing in time of the instantaneous frequencies, that shows opposite trends. The bulk frequency decreases *i.e.* red frequency shift whereas the surface frequency increases *i.e.* blue frequency shift. This trend reaches a common level around 2 ps. A very interesting fact is that we observe a redshift in the bulk frequency while literature reports [153, 155] regarding bulk coherent phonons, encounter an opposite frequency shift *i.e.* a blueshift.

### 5.4.2 Discussion

We start the discussion of the experimental results with the incoherent dynamics presented in upper panel of figure 5.27. Here, the linear reflectivity data could be fitted (solid line) by an exponential increase which gives a time constant of 0.88±0.02 ps. The monotonous increase of the LR and SHG signals reflects the bulk and surface electron dynamics, respectively, after laser excitation. The laser-induced electron dynamics[17] is shortly described in the following. Initially the laser energy is deposited in the electronic system which through inelastic *e-e* scattering events establishes a hot Fermi-Dirac distribution (here within 100 fs). Subsequently, the energy stored in the electron bath is transferred to the lattice via *e-p* scattering, that increase the temperature of the latter one. Within few ps after excitation, the electron and phonon baths reach a common temperature within few ps. The observed saturation of the LR and SHG signal around 3 ps, is thus determined by the equilibration of electrons and phonons temperature. Therefore, for Gd (at the employed laser fluence) the photoexcited hot electrons equilibrate with the lattice at a time constant of 0.88 ps.

At this point, it is worth discussing more detailed the origin of the oscillatory signal measured by linear reflectivity. We have ascribed the LR oscillations to bulk coherent phonons based, first, on the bulk sensitivity considerations of the LR technique. Secondly, the surface coherent mode measured by SHG has a different frequency that excludes measuring of the same phonon mode by both techniques. The coherent phonon excited at the surface represents the modulation of the interlayer distance between two adjacent

[17] The reader is referred to chapter 2 for a detailed discussion regarding the laser-induced electron dynamics.

(0001) planes *i.e.* along *c*-axis. The initial amplitude of the surface mode represents 10% from the total pump-induced dynamics (see fig. 5.21), which means that a considerable amount of excitation energy resides in the surface vibrational mode. Based on this, it is reasonable to assume that the strong surface oscillatory motion couples to the underlaying atomic layers down to a certain depth. Therefore, we ascribe the oscillatory LR signal as arising from the near-surface bulk layers that are set in motion by the strongly excited coherent surface mode. This conclusion is supported by the fact that in bulk, one can photoexcite totally symmetric $A_{1g}$ coherent phonon modes exclusively [158]. For Gd, the predicted [143] frequency of the symmetric $A_1$ mode is 2.3 THz, which is obviously smaller than the measured value of 3.3 THz (deduced from Fourier spectrum). Since the frequency of 3.3 THz observed in LR is close to the value of bulk $\Gamma_{3^+}$ mode (asymmetric) of 3.15 THz, we draw the conclusion that the observed bulk phonon mode is excited in the near-surface region by the surface coherent phonon mode.

Regarding the surface and bulk coherent oscillations, we observe initially two different frequencies whose difference amounts to ≈18%. The higher bulk phonon frequency is explained by the higher atomic coordinate and by the effectively stronger bonding in the bulk with respect to the surface. Breaking of the translation symmetry along $z$ axis (normal to the surface) in the surface region results in different bonding strengths acting on the topmost layer and the atomic layers underneath. Accordingly the interlayer distances are relaxed, their calculated [159] values and signs being: ≈-3.5% from the bulk equilibrium distance, for the distance between the surface and the subsurface layer and ≈+1% for the next, subsequent interlayer distance. Hence, the different initial frequencies for the surface and bulk modes are well conceivable from the arguments of different surface and bulk environments and the corresponding bonding strengths.

In the following we address the transient frequency evolution and the opposite frequency shift determined for the coherent surface and bulk phonons. From figure 5.29 we have seen that the bulk mode exhibits a transient blueshift of the frequency of ≈9% within the first 3 ps. In the literature [153, 155] the opposite trend *i.e.* redshift in the time evolution of coherent phonons is reported and has been explained by third-order anharmonic effects of the vibrational potential [153]. We have checked if higher order terms of the vibrational potential could account for the observed behavior of bulk and surface phonons. The approximation of a harmonic vibrational potential is valid for small atomic displacements, which in general is not true for the high non-equilibrium conditions produced by femtosecond lasers. Thus, one has to take into account higher order terms in atomic displacements for the potential energy expression: $U(x) = k_2x^2 + k_3x^3 + k_4x^4 + ..$ where $k_i$ represent the force constants of the oscillator and $x$ the atomic displacement. Solving the equation of motion for such an anharmonic oscillator one obtains [160] the oscillator frequency:

$$\omega = \omega_0 + \left(\frac{3k_4}{8\omega_0} - \frac{5k_3^2}{12\omega_0^3}\right) \cdot A^2 \tag{5.10}$$

where $\Omega_0$ is the frequency of the harmonic oscillator and $A$ is the amplitude of motion. In the right-hand side of the equation we have the fourth and cubic orders corrections of the frequency that scale with the amplitude in square. According to 5.10 we expect an increase or a decrease of the initial phonon frequency accounting for fourth or cubic

anharmonicities, respectively. In bulk gadolinium, third anharmonic terms are not allowed due to the lattice symmetry[18] for vibrations along *c*-axis. According to eq. 5.10 the remaining fourth order would increase the phonon frequency that is the opposite of the encountered trend for bulk phonon mode. At the surface the cubic anharmonic terms are allowed, that would decrease the phonon frequency. Again we observe the reversed behavior for the surface mode. Therefore, we can exclude the anharmonic effects as being the source of the transient frequency shift measured for bulk and surface coherent phonons. As will be shown in the following, we suggest that the transient photoexcited population is responsible for the observed frequency chirp.

As shown in figure 5.29, the initial frequency difference between $\Omega_s$ and $\Omega_b$ gradually decreases to zero, where both frequencies reach an asymptotic value of 3.15 THz around a delay time of 2 ps. This frequency reproduces the calculated *equilibrium* value $\Omega_0$ [143] of the bulk $\Gamma_{3^+}$ mode at $\Gamma$ point in Gd. Although the error bars increase in $\Omega_s$ around 2 ps due to the increased damping and it makes difficult to retrieve the bulk frequency at later delays. However, the frequency convergence of the phonon modes is well distinguished. Simultaneously, inelastic electron-phonon scattering transfers the excess energy from the electron to the phonon bath. This process is reflected in the transient incoherent variations of the SH field $\Delta^{2\omega}_{incoh}$ plotted also in the figure. Interestingly, its time-dependence shows a good agreement with the transient frequency chirp in $\Omega_s$. This parallelism between $\Delta^{2\omega}_{incoh}$ and the transient $\Omega_s$ suggests that the incoherent electron dynamics is responsible for the frequency chirp of the surface mode. Regarding the bulk electron dynamics, we have obtained from the incoherent part of the LR signal an electron-phonon equilibration time of 0.88 ps (see above). The instantaneous amplitudes of the bulk and surface phonons plotted in fig. 5.29, decay exponentially with a time constant of 0.87 ps. Also the decay times for surface and bulk phonons deduced from fitting the oscillatory data with relation 5.8 have comparable values of $\tau_s$=0.86 ps and $\tau_b$=0.9 ps, respectively. Based on the good agreement of these values, we can conclude that the transient electron dynamics determines the decay time of both surface and bulk coherent phonon modes. This fact identifies the inelastic electron-phonon scattering as an efficient decay channel for the coherent lattice vibrations in case of Gd(0001).

We have shown above that both, the bulk and surface coherent phonons, live as long as a non-equilibrium exists between electrons and lattice. The question that arises is how can the electron-phonon interaction explain the change in the frequency of the coherent phonon modes. The excitation mechanism of the surface coherent vibration has been attributed (see section 5.3) to an asymmetric photoexcitation of the surface state that leads to an ultrafast charge redistribution at the surface which triggers the initial ion displacement. The changed surface potential on which the atoms start to oscillate thus depends on the photoexcitation strength of the electronic population. The electron-phonon interaction redistribute continuously the excess energy residing in the electronic system and therefore the shape of the surface potential will evolve accordingly. Eventually the electron and phonon baths reach a common temperature *i.e.* are in equilibrium, that determines the surface potential to reach its equilibrated state before excitation. This is corroborated

[18] The inversion symmetry of the hcp lattice should be fulfilled. Thus, just even order anharmonicities are allowed in the hcp bulk.

by the coherent phonon frequency which reaches the equilibrium frequency of $\Omega_0$=3.15 THz when the electrons are in equilibrium with the lattice. The same argument holds also for the bulk phonons dynamics namely the shape of the bulk vibrational potential is determined by the relaxing electron population, that explains the transient frequency shift and eventually levelling to $\Omega_0$. But how the opposite frequency shift for surface and bulk phonons can be explained?

The initially excited electron-hole pairs thermalizes to a hot electron population within 100 fs. Due to the energetic positions of the surface state components with respect to $E_F$, the effect of an excited electron temperature is a stronger decrease of the electron population in the majority state (-0.2 eV binding energy) than the population increase of the minority component (0.4 eV binding energy). Thus, a hot electron temperature results in a lower electron density at the surface with respect to bulk. The excited surface and bulk electron densities are relaxed by incoherent *e-p* scattering, that changes gradually the shape of the vibrational potential and implicitly the oscillation frequency. Due to the different electron densities in the surface and bulk their behavior is opposite as they relax to the lattice: the bulk electron density gradually decreases while the opposite holds for the surface. This explains the observed opposite frequency shift for bulk and surface phonons.

Summarizing, the observed time-dependent shift in the frequency of the phonon modes could not be explained by anharmonic corrections of the harmonic potential but through the influence of the transient excited electron population on the shape of the vibrational potential. Thus the frequency change of both coherent modes has a pure electronic origin.

### 5.4.3 Conclusions

The coherent optical phonon excited at the Gd(0001) surface couples to the underlying atomic layers which leads to a coherent oscillatory motion of the latter ones. Employing simultaneously surface (SHG) and bulk (LR) sensitive techniques we could distinguish and analyze the dynamics of the coherent phonon modes at the surface and in the bulk.The initial frequencies amount to 3.4 THz and 2.8 THz for the bulk and surface phonon mode, respectively. As a function of pump-probe delay we observe a frequency *redshift* (decrease) for the *bulk* mode and a *blueshift* (increase) for the *surface* mode that goes in parallel with the incoherent *e-p* dynamics. The interesting feature of the frequency redshift of the bulk mode, that is opposite trend compared to the results reported in literature, could not be explained by anharmonicity effects. Instead, the transient frequency shift of both coherent modes have been ascribed to the time-evolution of the surface and bulk vibrational potentials under the effect of a relaxing photoexcited electronic population. The electron-phonon scattering has been identified as an efficient decay channel for bulk and surface coherent phonons since they live as long as a non-equilibrium exists between electrons and lattice.

## 5.5 Coupled coherent phonon-magnon mode: excitation and relaxation

The scope of the present section is to investigate in detail the proposed excitation mechanism of the coherent phonon-magnon mode and to identify the available decay channels. For this purpose, the systematic variation of the laser photon energy and temperature of the sample has been employed. Varying the laser wavelength and accounting for the specific electronic structure of the Gd(0001) surface, different levels of photoexcited carriers are produced in the surface state. Thus, the charge-driven character of the excitation mechanism proposed for the coupled phonon-magnon mode can be tested. Based on the temperature dependence of the surface state exchange splitting, we perform a further check for the excitation of the coupled lattice-spin quasiparticle. Moreover, rising the temperature, the thermal (incoherent) electron, phonon and magnon population is increased that can scatter with the coherent mode and may represent an efficient decay channel of the coherence in the lattice and spin system.

### 5.5.1 Spectral dependence

First we study the spectral dependence of the transient linear and nonlinear optical response from Gd(0001) surface after laser excitation. For these investigations, the laser photon energy has been varied simultaneously for the pump and probe beams in the available tunability range of the cavity-dumped Ti:Sa oscillator between 1.44 and 1.68 eV. The measured time-resolved dependencies of the SHG signal are plotted in the figure 5.30 together with the transient linear reflectivity (the solid line). The first observation is that despite of the relatively narrow spectral range we see a strong variation of the nonlinear optical response with the laser wavelength. The behavior of the linear reflectivity signal recorded simultaneously with the SHG signal, is wavelength-independent in this spectral range since is not sensitive to the surface state but rather to the bulk states. The showed $\Delta R/R$ data set represents an average over all used wavelengths since no change in the time-dependent profile is observed by varying the laser wavelength, just in the magnitude of the variations. These observations confirm the key role of the exchange-split surface state in the SHG process whose optical transitions evolve resonantly (see figure 5.11) via the surface state.

In order to analyze the rather complex behavior of the even SH field plotted in the upper panel of figure 5.30, its dynamics is separated in coherent and incoherent contributions, that are evaluated here at 80 fs delay time [119]. This delay has been chosen since we are interested on the effect of the excited electron population on the coherent mode. The response at 80 fs pump-probe delay[19] reflects the initial excitation strength injected into the system upon absorption of the fs laser pulse. At this delay the electronic system is internally thermalized as deduced from the transient energy density obtained in the TRPE measurement (see fig. 5.16) and the 2TM simulation of the electron energy redistribution(see fig. 2.7) on Gd(0001).

[19]The influence of the coherent artifact produced by the cross-correlation of the pump and probe beams, can be safely neglected at 80 fs delay since its effect can be traced up to a delay of maximum 50 fs (see

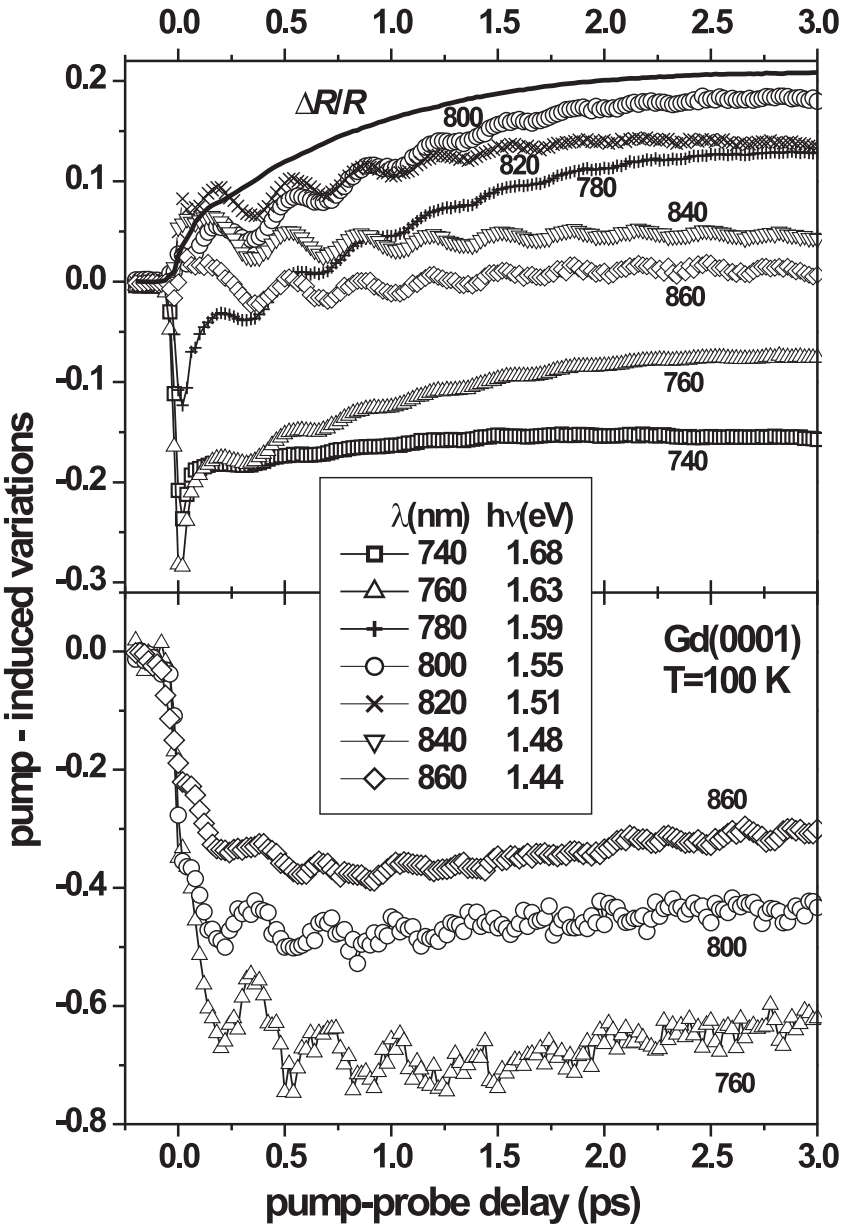


**Figure 5.30:** Laser wavelength dependence of the transient SH fields and of LR signal from Gd(0001)/W(110) at T=100 K. **Upper panel**: The transient linear reflectivity (black solid line) does not change with the laser photon energy owing to its bulk sensitivity. The even SH field behavior reveals a competition between coherent and incoherent components as a function of photon energy. The former ones dominate the dynamics for lower photon energies while the latter ones are governing the higher photon energy spectra. **Lower panel**: The time evolution of the odd SH field exhibits a significant spectral dependence for the initial drop in the transient signal and the amplitude of the oscillatory part *i.e.* both quantities increase with increasing the laser photon energy. Adapted from [119].

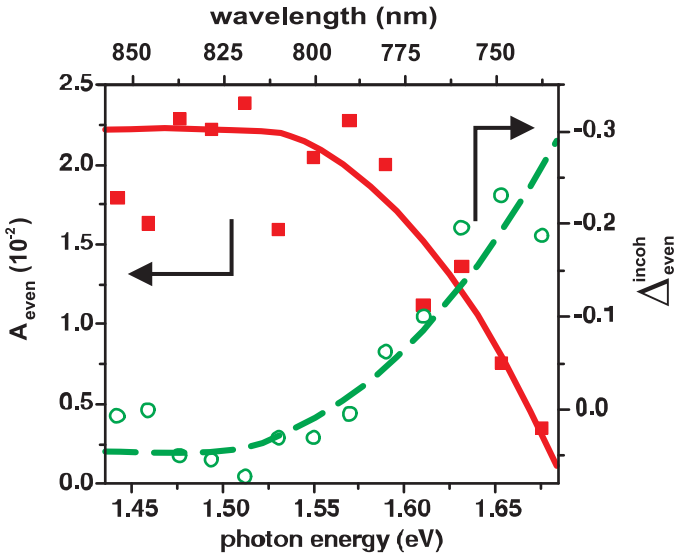


**Figure 5.31:** Photon energy dependence of the coherent (squares) and incoherent (empty circles) components of the transient SH even field measured at 80 fs delay time. Both quantities are normalized to the value of even SH field measured at negative delays. Note the clear opposite trend of the coherent and incoherent contributions as a function of photon energy. The solid and the dashed lines are guides for the eye.

Figure 5.30 (upper panel) shows the spectral dependence of the transient even field $\Delta_{even}$, which exhibits two trends that evolve differently for its coherent and incoherent components. For small photon energies (the 860 and 840 nm data sets) the coherent oscillatory part dominates while for larger photon energies (*e.g.* 740 nm) the incoherent component prevails. These observations are based on (*i*) the lack of the incoherent component signature for the measurements at small photon energies, the transient signal having a pure oscillatory character (*e.g.* 840 nm data set) (*ii*) the appearance of a pronounced incoherent component for larger photon energies whilst the oscillatory fraction decreases gradually as the photon energy is increased. Such a behavior suggests that for small photon energies the excitation energy goes preponderantly into coherent part whereas the opposite holds for larger photon energies. The possible effect of the probe beam (since the pump and probe beams have the same wavelengths) on the excitation and the subsequent dynamics of the system is discussed later in this section.

The competing behavior of the coherent and incoherent parts of the $\Delta_{even}$, that is already observable in the raw SHG data of figure 5.30, is much more clearer seen in figure 5.31. Here we plot the coherent phonon amplitude $A_{even}$ and the incoherent component $\Delta_{even}^{incoh}$ measured at a 80 fs delay in the even SH field for various laser photon energies. Their opposite trend as the laser photon energy increases is clearly distinguishable. For longer wavelengths the incoherent part is close to zero while the coherent one exhibits a maximum and the reversed situation is encountered for smaller wavelengths.

figure 4.9).

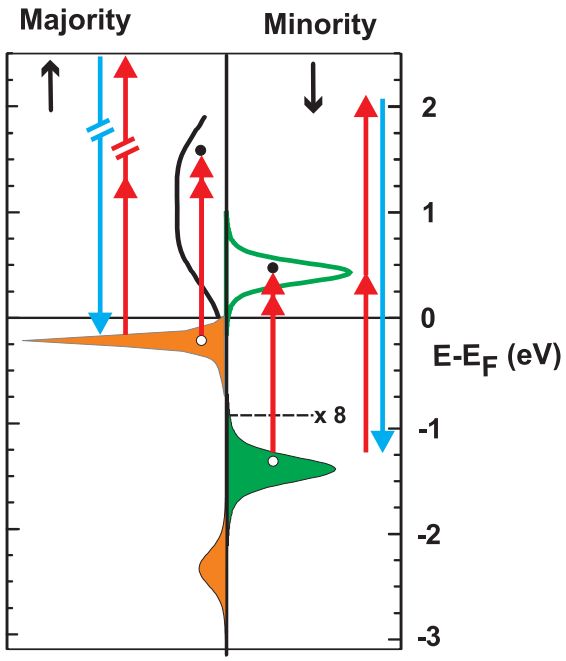


**Figure 5.32:** Schematic spin-resolved electronic structure for Gd(0001) at $\overline{\Gamma}$ point and the main absorption channels for the pump beam at the fundamental frequency depicted by the double-head arrows, that represent the smallest and the largest employed photon energies. The occupied part of the electronic structure is obtained from photoemission measurements [17], the unoccupied surface state component from STS investigations [48] and the unoccupied bulk states from inverse photoemission results [32]. The pump beam excites electrons (filled circle) from bulk to the surface state leaving behind a hole (empty circle), in the minority channel, and majority electrons from surface state to the unoccupied bulk state. Upon increasing the fundamental photon energy (double-head arrows) the absorption in the minority channel is enhanced due to the better energy matching. The optical transitions for the probe SHG process are displayed close to the edges of the diagram. Note that the unoccupied bulk state is measured without spin resolution, but is arises mainly from the unoccupied majority $5d$ bulk state [32].

The spectral behavior of the transient oscillatory $\Delta_{even}$ can be understood by inspecting the schematic spin-resolved electronic structure of Gd(0001) at $\overline{\Gamma}$ point, presented in the figure 5.32. Note that in the following we discuss the excitation process *i.e.* the pump-induced optical transitions depicted in the figure 5.32 by the double-head arrows that represent the lowest and the highest achievable photon energies, respectively. For long wavelengths the laser photon energy does not match the energetic separation in the minority channel *i.e.* between the occupied bulk state and the unoccupied $S^{\downarrow}$ surface state. This is not the case for the majority channel where even the smallest photon energy bridges the gap between the $S^{\uparrow}$ surface state and the unoccupied bulk state. Therefore, for low photon energies the spin-up optical transitions are dominant since the spin-down channel contribution is weak due to the off-resonant spin-down transitions at this photon energy. Consequently, in this energy range the excess charge produced in the surface state

is dominated by the photoexcited holes. In section 5.3 we have explained the excitation of the coherent phonon as being determined by the initially photoexcited excess charge in the surface state, that requires a transient charge redistribution in the surface region in order to be screened. This ultrafast charge redistribution is considered responsible for the excitation of the coherent mode. Thus, according to the proposed excitation mechanism the amplitude of the coherent lattice mode should reflect the magnitude of the photoexcited excess charge in the surface state. Hence for the low photon energy range a considerable amount of photoholes is generated in the surface state (there are very few photoexcited electrons in the spin-down component) that requires a large transient charge redistribution for screening and therefore producing large amplitude of lattice vibrations. Increasing the photon energy, the optical transitions in the minority channel become active and more electrons are excited in the minority surface state. Thus, a reduced amount of excess charge is produced in the surface state that requires a weaker transient charge redistribution. This results in a decreased coherent phonon amplitude which coincides with the experimental observation for the high energy range. Also with increasing photon energy we notice the appearance of a pronounced incoherent component in the transient SHG response. For the highest achievable photon energy one encounters a decrease in the $A_{even}$ over one order of magnitude (see fig. 5.31) whereas the drop in the magnitude of the incoherent contribution is almost three times bigger.

The time evolution of the incoherent part of $\Delta_{even}$ within the first 100 fs is attributed [17, 70, 119] to the relaxation of the highly photoexcited electrons to a thermalized electron bath via inelastic *e-e* scattering. The electron thermalization is achieved by generating cascades of secondary electron-hole pairs which redistribute the energy of the initially excited electron gas (for details see chapter 2). The thermalized electrons are characterized by a common temperature $T_e$ that determines [44, 56] the excitation energy density $U(t) \propto T_e$ residing in the system. According to eq. 2.18 the pump-induced variations in the SHG response are proportional to $\frac{\partial \chi^{(2)}}{\partial T_e}\Delta T_e$ (also to variations produced by lattice temperature, lattice vibrations etc.) where the $\chi^{(2)}$ is the second-order susceptibility tensor. Thus we can consider the incoherent $\Delta_{even}$ at 80 fs (when the electron bath is thermalized) to reflect the initial excitation energy deposited into the system.

In order to explain the spectral dependence of the incoherent $\Delta_{even}$, presented in figure 5.31, we consider the effect of the photoexcited holes and electrons in the surface state components. As mentioned above, at low photon energies the hole generation in the majority surface state dominates over the electron excitation process in the minority channel. The photoexcited holes relax via a symmetric process as for the photoexcited electrons namely hole-hole scattering with generation of secondary hole-electrons pairs close to $E_F$. We can consider that the electrons and holes contribute equally to the energy density $U(t)$ [56, 13], that is responsible for the induced changes of $\Delta_{even}$ at early times (see above). Thus for low photon energies we have mainly the contribution from photoexcited holes to the incoherent $\Delta_{even}$. As long as the amount of photoexcited electrons in the minority channel is reduced, the photoexcited holes contribution to the energy density dominates that is reflected as a relatively constant level in the incoherent $\Delta_{even}$. Increasing the photon energy, more electrons are excited in the minority surface state and their contribution adds to the energy density term $U(t)$, which decreases the magnitude of the $\Delta_{even}^{incoh}$ as can

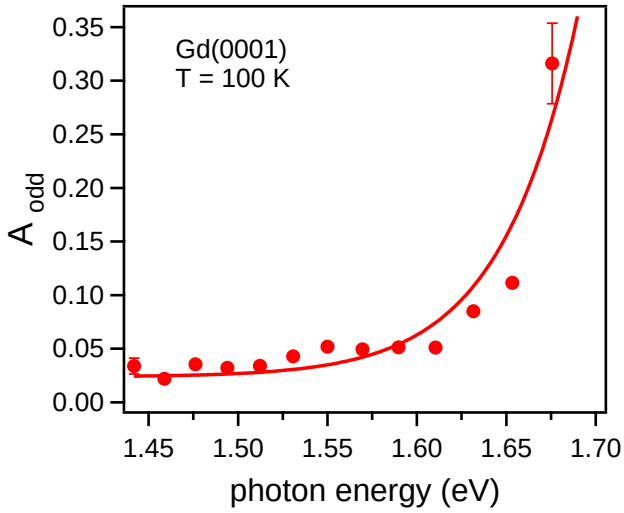


**Figure 5.33:** Spectral dependence of the amplitude of the coherent magnons measured by odd SH field at the Gd(0001) surface for T=100 K. The coherent magnon amplitude increases with increasing laser photon energy. The solid line is a guide for the eye.

be observed in fig. 5.31.

Summarizing this part, the transient behavior of $\Delta_{even}$ upon laser wavelength variation confirms the charge-driven character of the proposed excitation mechanism showing that the amplitude of the coherent oscillations in $\Delta_{even}$ (ascribed to coherent phonons) scales with the photoinduced excess charge in the surface state. The incoherent electron and hole dynamics reflected by the $\Delta_{even}^{incoh}$ at early times, give a measure of the photo-injected energy density in the surface state, that increases with the efficiency of the spin-selective optical transitions in the surface state components.

Now we address the spectral dependence of the transient odd SH field, that is displayed in the lower panel of the figure 5.30. For clarity reasons we show here three exemplary data sets, the other measurements lying in between and following the trend of the plotted dependencies. We observe that the transient $\Delta_{odd}$ shows a pronounced dependence on the laser photon energy in the initial drop at early delays and in the amplitude of the oscillatory component. The abrupt drop within laser pulse duration has been discussed in detail in section 5.2.1 and interpreted as the decrease of the spin polarization at the Gd(0001) surface due to spin-flip scattering of hot electrons among spin-mixed states. The oscillatory component of $\Delta_{odd}$ has been assigned before (section 5.3) to coherent magnons having the same frequency as the coherent phonons measured in $\Delta_{even}$.

The explanation for the spectral dependence of the initial drop in $\Delta_{odd}$ is based on the variations of the spin polarization of the surface state as the photon energy is modified. At low photon energy the spin-up channel is active that excites majority electrons from the surface state to the bulk and consequently the spin polarization of the surface state is reduced. In this photon energy range the spin-down transitions are considered to have a weak contribution due to the photon energy mismatch in the spin-down channel (see

fig. 5.32). Increasing the photon energy, the spin-down channel starts to contribute, due to the better photon energy matching, and minority electrons are photoexcited in the $S^{\downarrow}$ component. Simultaneously majority electrons are promoted from the surface to the bulk state. Both processes are decreasing further the spin polarization of the surface state that is reflected in the measured $\Delta_{odd}$ by an increasing drop for higher photon energies.

Simultaneously with the dynamics of the incoherent part an interesting behavior is developed by the coherent contribution of the odd SH field, that has been earlier ascribed to coherent magnons. As depicted in the figure 5.33 the amplitude of the coherent oscillations of $\Delta_{odd}$ increases with increasing photon energy over one order of magnitude. Such a behavior is intriguing since one expects that the coherent magnon amplitude scales with the amplitude of the coherent phonon which decreases with increasing photon energy (see fig. 5.31). This expectation is based on the proposed excitation mechanism of the coherent phonon-magnon mode, which predicts a coherent magnon amplitude proportional to the magnitude of the lattice displacement via the modulation of the exchange interaction strength $J$ (see fig. 5.24). Thus, according to the excitation model we expect a decreasing amplitude of the coherent magnon with increasing the photon energy, but the opposite trend is observed. One possible explanation is based on the relative phase $\phi$ (see section 5.1) between the even and odd SH fields, whose spectral dependence is displayed in the figure 5.9. In the photon energy range between 1.63 eV and 1.68 eV, the relative phase shows an oscillatory variation from -60 to 80 degrees complemented by a decrease of the magnetic contrast to zero value. The phase variation affects drastically the relative weight of the even and odd SH field contributions to the total SHG response (see fig. 5.6), and implicitly their oscillatory components. Thus, the observed relative phase variations can change also for the oscillatory fractions of the SH fields, that might lead to a significant increase in the coherent magnon amplitude as has been observed.

The spectral region in which the the relative phase exhibits sharp modifications covers the last three points in the dependence of the oscillatory $\Delta_{odd}$ amplitude displayed in figure 5.33. Neglecting these data points we still encounter, for lower photon energy, an increasing trend in the amplitude of the coherent magnons by a factor of two. Thus one can suggest that in the high energy spectral range the three points follow the increasing behavior observed for at low energies but their magnitude is enhanced by a "spectroscopic factor" determined by the value of the relative phase $\phi$.

One check for this tentatively explanation of the oscillatory $\Delta_{odd}$ behavior is to measure the pump-induced variations in the relative phase $\phi$. Unfortunately, with the present experimental setup such a measurement is not possible. However, the spectral dependence of the coherent magnon mode is not completely understood, and for the moment is still an open question that requires further investigations.

Until now we have obtained a general picture describing the encountered dynamics (coherent and incoherent SHG components) based on the photoexcitation effect of the pump pulse only. Since the probe beam has the same wavelength as the pump, it is worthwhile discussing its possible effects on the detected SHG response. One extreme case would be the bleaching of the probe optical transition after a strong pump beam excitation (see section 2.5 for details regarding bleaching). That means that the probe transition is blocked (the material becomes transparent for this optical transition), due to

the occupation by the excited population of the final states for the probe transition, that before excitation were available. This will be reflected in the transient signal as a sharp decrease that would be maintained as long as the electronic population is in a highly excited state *i.e.* within the first hundreds fs [85]. Such a behavior is not observed in the spectral dependence of the nonlinear optical response from Gd(0001) surface: $\Delta_{odd}$ decrease holds for several tens of ps whereas $\Delta_{even}$ exhibits the effect of the cross-correlation in the first 50 fs and starting with 80 fs reflects the pure electron dynamics (see fig. 5.16). An intermediate situation would be when the probe optical transition can evolve but is contributing weakly to the initial excitation of the system. This last situation might be our case and we are aware of its potential implications *e.g.* the probe can contribute to the excitation of additional carriers in the surface state and thus influence the coherent mode and the initial dynamics in the incoherent SH fields. In order to evaluate the presumably effect of the probe beam on the excitation and the subsequent dynamics encountered on Gd(0001), a two-color experiment (different wavelengths for the pump and probe beams) would be required.

#### Conclusion

Pronounced changes in the time-resolved MSHG response from the Gd(0001) surface have been measured upon changing the laser wavelength between 740 nm and 860 nm. The coherent and incoherent components of $\Delta_{even}$ (that reflect the lattice and electron dynamics, respectively) show a competing behavior as the laser photon energy is varied. The coherent part of $\Delta_{even}$ dominates the low energy range whilst at higher photon energies the incoherent $\Delta_{even}$ part prevails. This behavior has been assigned to the relative weight of the spin selective optical transitions via the surface state contributing to the total MSHG signal. The amplitude of the coherent phonons varies over one order of magnitude in the investigated photon energy interval, which is attributed to the different degrees of charge asymmetry excited in the surface state as the laser wavelength is varied. Therefore this result provides a strong support for the proposed excitation mechanism of the coherent phonon-magnon mode as being a charge-driven mechanism. The incoherent part of $\Delta_{even}$ measured at 80 fs pump-probe delay reflects the photo-injected energy density, that increases with increasing photon energy. The behavior of the SH odd field is consistent with the variation of the spin polarization in the surface state that occurs simultaneously with the photoexcited charge redistribution *i.e.* at small photon energies a reduction of the spin polarization is encountered that continuously decreases as the photon energy increases.

### 5.5.2 Temperature dependence

In this part we study the temperature dependence of the time-resolved linear and SHG response from the Gd(0001)/W(110) sample. The idea is (*i*) to check how the temperature-dependent variation of the exchange splitting of the surface state can affect the coherent and incoherent SHG dynamics since this will lead to changes in the resonance condition of the SHG process via the surface state (*ii*) to investigate the possible relaxation pathways of the coherent mode, since elevating the temperature results in an increased electron, phonon and magnon thermal population, which can scatter with the coherent mode and

might modify the relaxation/damping of the coherent excitation.

The temperature dependent study has been performed between 40-400 K at a laser wavelength of 800 nm. The temperature range below the Curie point (293 K for bulk Gd) has been covered in 20 K steps whereas above $T_C$ a lower density data points have been measured. This was due to the much longer measurement times required to resolve the small oscillatory components (one order of magnitude smaller in comparison to low temperature data) of the transient signal. The dependence of the transient SH even $\Delta_{even}$ and odd $\Delta_{odd}$ fields on the temperature are presented in figure 5.34 and 5.35, respectively. For clarity, in figure 5.35, a few representative SH odd field dependencies have been chosen, the other measurements following the observed trend.

We observe pronounced changes in both the coherent and the incoherent components of the MSHG response as the temperature is varied. In $\Delta_{even}$, shown in fig. 5.34, the oscillation amplitude decreases gradually with temperature and simultaneously the pump-induced variations in the incoherent background decrease with increasing temperature. As an exemplary data set for temperatures above the Curie point we have selected the measurement performed at 400 K, that is magnified by a factor of two in figure 5.34. The oscillatory feature, although reduced in amplitude, can be clearly distinguished even at this elevated temperature. Regarding the $\Delta_{odd}$ dependence, shown in figure 5.35, the magnitude of the oscillatory component is decreasing with increased temperature and can be resolved (with a reasonable statistics) up to 200 K. For higher temperatures the noise in $\Delta_{odd}$ increases above the oscillatory amplitude, that hinder an exact determination of the temperature at which the coherent magnon vanishes. In this context we note that an oscillatory pattern is present (one period) for the 240 K data set, but is in the noise level of the transient signal. For the incoherent $\Delta_{odd}$ we observe a temperature-dependent drop at early delay times (from 40% at 40 K to 80% at 240 K), displayed in the inset of the figure 5.35, followed by a levelling to a constant value. Increasing further the temperature the magnetic contrast $\rho$ decreases to zero (see fig. 5.12) and the drop in $\Delta_{odd}$ is approaching -1 value, that is equivalent with a total loss of magnetic ordering. This produces also a higher level of noise and because of this reason the curves for higher temperatures in the vicinity of $T_C$ are left out.

#### Incoherent behavior

In the interpretation of the experimental data we start with the incoherent behavior of the $\Delta_{even}$ and $\Delta_{odd}$ transients. The time evolution (within 0-3 ps interval) of the incoherent part of $\Delta_{even}$ (denoted $\Delta_{even}^{incoh}$ ) reflects [17, 70] the formation of a hot electron distribution via *e-e* scattering and the subsequent energy transfer to the lattice via *e-p* scattering, that leads eventually to a common temperature for the electrons and lattice subsystems. These events correspond to the rapid modifications of $\Delta_{even}$ within the first[20] 100 fs and its monotonous increase and equilibration around 2 ps, respectively. This behavior, presented in sections 5.3 and 5.4 at T=90 K, is observed also here as plotted in the figure 5.34. Elevating the temperature, the absolute value of the pump-induced change in $\Delta_{even}^{incoh}$

[20] As pointed out in the preceding section, the pump and probe cross-correlation pattern extends up to 50 fs (see figure 4.9), and thus the later time delays reflect the real dynamical behavior of the system.

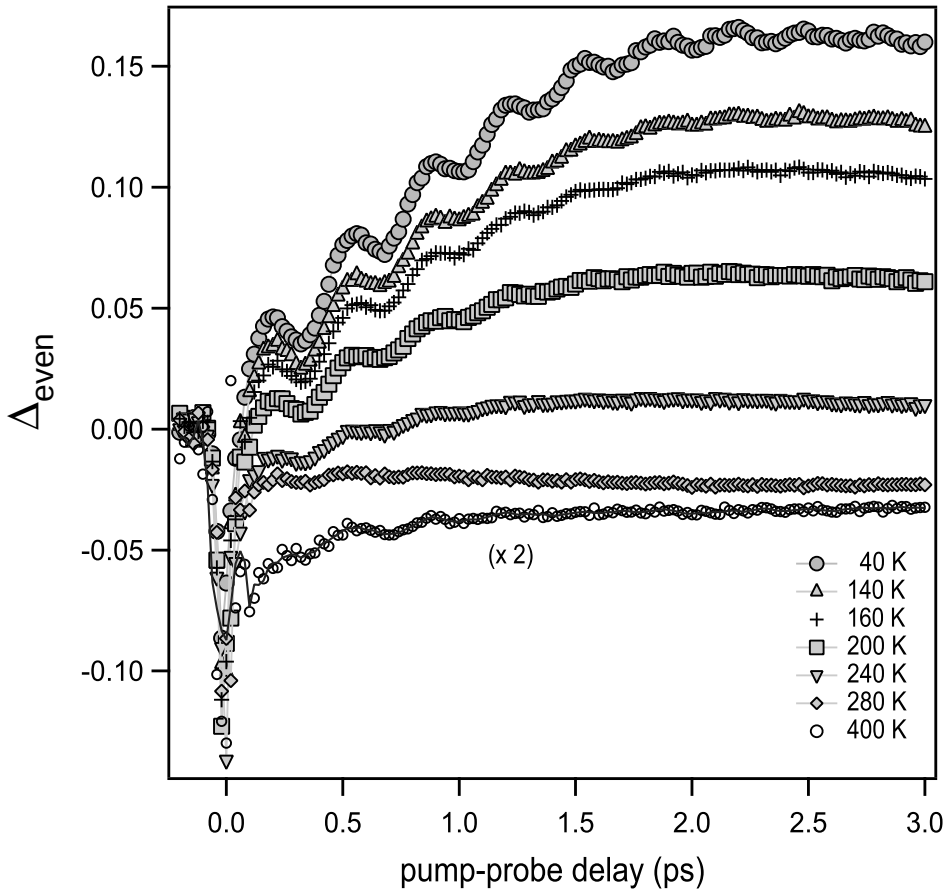


**Figure 5.34:** The pump-induced variations in even SH field for various temperatures from a 20 nm Gd(0001) film. The measurements covered the 40–400 K temperature range and representative data sets are presented. As an example for the measured scans above Curie point (293 K), the measurement performed at 400 K is displayed (for clarity magnified by a factor of two).

shows a gradual decrease, which are quantified at 3 ps pump-probe delay. We will come back to these results further below.

The incoherent part of the $\Delta_{odd}$ depicted in the figure 5.35, shows also significant changes with temperature. In the low temperature range the temporal evolution of $\Delta_{odd}$ is rather monotonous, with the initial drop and the levelling off to a constant value (around 1.5 ps). At T=100 K, the equilibrium spin polarization is recovered on a hundreds of picosecond time scale due to spin-lattice relaxation, as has been shown in section 5.2.2. The magnitude of the initial decrease in $\Delta_{odd}$ as a function of temperature, plotted in the inset of fig. 5.35, shows a gradual decrease with elevating temperature. As suggested by the solid line, the drop in $\Delta_{odd}$ seems to follow a M(T) behavior, reaching a -1 value (total loss of magnetic ordering) around 290 K (extrapolating the M(T) curve), that is close to Curie point of 293 K. The initial drop observed in $\Delta_{odd}$ has been attributed (see section 5.2.1) to the spin-flip scattering of the hot electrons among spin-mixed states. Increasing the temperature

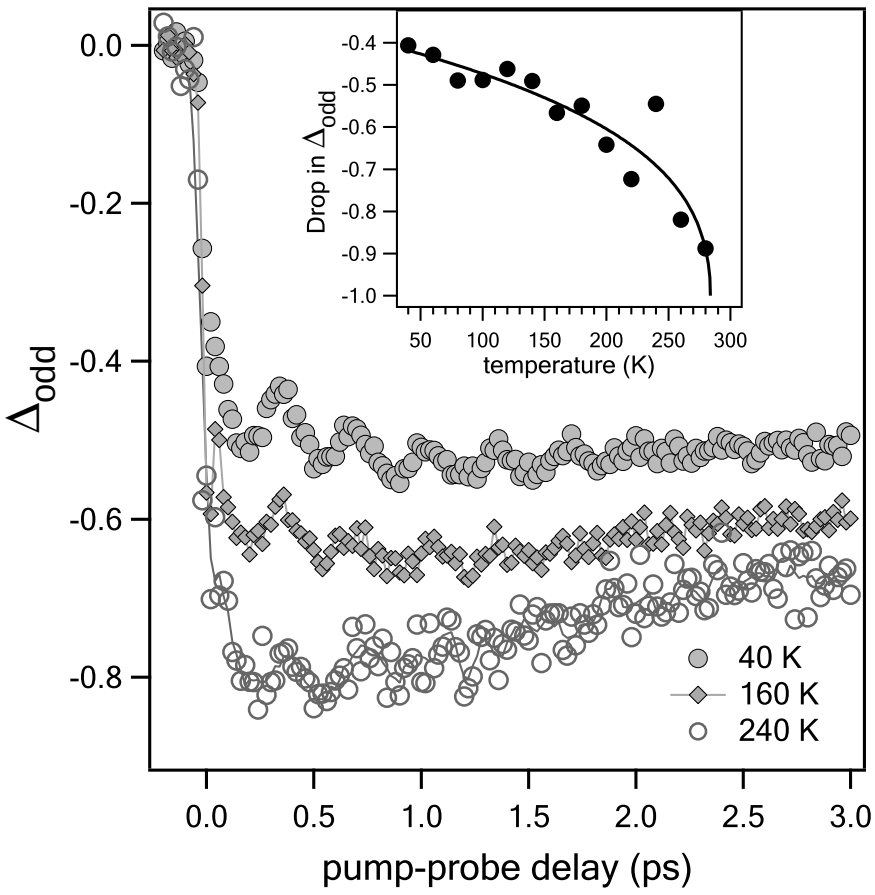


**Figure 5.35:** The pump-induced variations in odd SH field for several selected temperatures measured simultaneously with the data presented in figure 5.34. In the inset the measured drop in $\Delta_{odd}$ close to zero delay is plotted versus temperature. The solid line in the inset is a guide for the eye.

the amount of spin-mixed states is enhanced [36]. Thus, the increased drop in $\Delta_{odd}$ at early times, as the temperature is elevated, is explained by the increased phase space for spin-flip scattering provided by the higher density of spin-mixed states.

Coming back to the transient even SH field behavior, we have considered the saturation of $\Delta_{even}^{incoh}$ to a maximum level around 2 ps delay, as reflecting the *e-p* equilibration. Since here we are interested in the effect of *e-p* equilibration on the SHG dynamics we monitor the temperature-dependent behavior of the maximum value of $\Delta_{even}^{incoh}$ at a pump-probe delay of 3 ps. Hence, this is our criterion in interpreting the temperature-dependent profile of the incoherent $\Delta_{even}$. This is displayed in the left panel of the figure 5.36. Here we observe up to 100 K a constant level followed by a major decrease to 280 K and a relatively constant value (within the error bars) at $T_C$ and higher. In the same figure (right panel) we plot the variation of the surface state exchange splitting as a function of

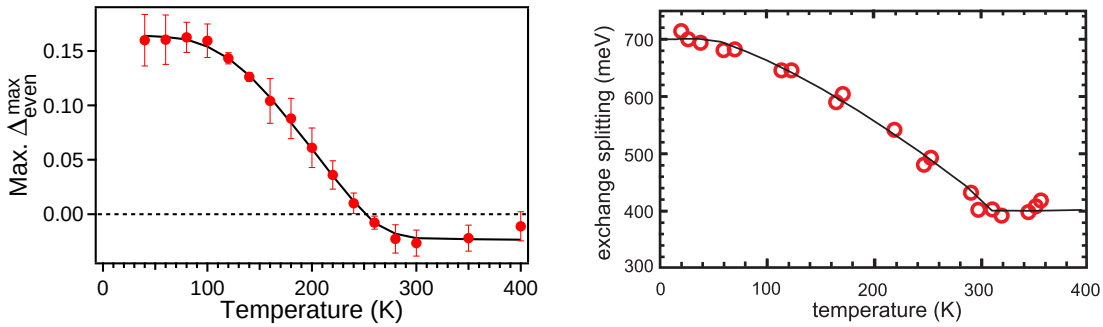


**Figure 5.36: Left**: The dependence of the maximum value of pump-induced variations in the incoherent $\Delta_{even}$ as a function of temperature. The dotted line indicates the zero level. Note the negative value for temperatures starting with 260 K. **Right**: The variation of the exchange splitting $\Delta_{ex}$ of the Gd(0001) surface state with the temperature as measured with STS by Bode *et al.* [33]. In both panels the solid lines are guide for the eye.

temperature, as was measured with scanning tunnelling spectroscopy (STS) by Bode *et al.* [33]. As noticed, the temperature dependence of $\Delta_{even}^{max}$ and of the surface state $\Delta_{ex}$ exhibit a few similarities. We observe nearly constant levels in both dependencies covering the same temperature intervals *i.e.* from low temperature to 100 K and from $T_C$ to higher temperatures (360 K for $\Delta_{ex}$ and 400 K for $\Delta_{even}^{max}$). Also we know that the SHG process evolves resonantly enhanced via the surface state, and thus any change (binding energy, broadening etc.) of the latter one will affect sensitively the SHG response. Hence, these facts suggest that the $\Delta_{ex}$ of the surface state might be related to the observed dynamics of $\Delta_{even}^{max}$.

Considering the electronic structure of Gd(0001) surface plotted in fig. 5.32, we see that a decreased $\Delta_{ex}$ due to temperature increase affects mainly the efficiency of the optical transitions in the minority channel. The transitions in the majority channel are less affected due to the energetically broad final state of the optical transition and due to smaller change in binding energy of the majority surface state [34, 33]. At *low* temperature and for the employed photon energy of 1.55 eV, the transitions in both majority and minority channels contribute, and photoexcited electrons and holes are excited in the surface state whose thermalization (and subsequent cooling to the lattice) produce the observed changes in $\Delta_{even}$ (see the preceding section). Increasing the temperature to 100 K the exchange splitting remains nearly constant [30] and thus a constant level of $\Delta_{even}^{max}$ is observed (see fig. 5.36). Above 100 K the $\Delta_{ex}$ gradually decreases *i.e.* $S^{\downarrow}$ shifts to lower binding energies, which means that the laser photon energy matches better the energetic separation in the minority channel, that enhances the excitation probability of the minority electrons in the surface state.

As pointed out in the previous section, an increased population of electrons (and holes) increases the energy density into the system that decreases the magnitude of $\Delta_{even}$. The same interpretation holds also here, but now the increased electron population is determined by the shift of the spin-down surface state and not because of the increased photon energy. The decrease of $\Delta_{even}^{max}$ continues as long as the $\Delta_{ex}$ decreases *i.e.* up to the Curie

point. Above $T_C$, $\Delta_{ex}$ is constant [33] (up to the highest investigated temperature of 360 K ) and is reflected as a constant level of the $\Delta_{even}^{max}$. However, their absolute changes upon temperature increasing are different with $\Delta_{ex}$ that reduces by roughly 50 % while $\Delta_{even}^{max}$ decreases by more than one order of magnitude. That means there is no linear relationship between these quantities, which suggests either a nonlinearity between $\Delta_{ex}$ and the carriers excitation probability or there is another process that contributes to the $\Delta_{even}^{max}$ behavior.

Summarizing, by considering the qualitative similarities of the $\Delta_{even}^{max}$ and the $\Delta_{ex}$ of the surface state and accounting for the resonance enhancement of the SHG process via the surface state, we could explain the temperature-dependent variation of $\Delta_{even}^{max}$ as a changing carriers excitation probability in the surface state due to the temperature-dependent shift of the surface state components *i.e.* a decreasing exchange splitting of the surface state.

### Coherent behavior

In the following we continue with the presentation of the behavior of the coherent phonon-magnon mode upon temperature variation. The oscillatory component of the transient SH fields has been obtained after removing the incoherent background in an identical manner with the procedure presented in section 5.3. The resulting amplitudes of the oscillatory $\Delta_{even}$ and $\Delta_{odd}$ are plotted in the figure 5.37. We observe that the phonon and magnon amplitudes[21] exhibit a rather similar trend versus temperature, although the coherent magnon data shows a higher scattering due to lower signal to noise ratio of the $\Delta_{odd}$. The oscillatory feature of the magnon could be resolved up to a temperature of 200 K. The equivalent temperature behavior of the phonons and magnons give us an indication about the coupling strength of these quasiparticles. The measured amplitude of the coherent phonon mode is decreasing with increasing temperature over one order of magnitude and, remarkably we could resolve it even above Curie point up to 400 K. The latter observation demonstrates the presence of a residual exchange splitting of the surface state above $T_C$ since the excitation of the coherent phonon-magnon mode is intrinsically connected with the presence of an exchange-split surface state (see Y overlayer experiment in section 5.3).

The overall decrease of the amplitude of the coherent phonons and magnons as the temperature is elevated is ascribed to a variation of their excitation probability with the temperature. Since the excitation of the phonon-magnon mode is connected with the presence of the exchange-split surface state (see section 5.3), a variation of the exchange splitting will influence the excitation and the subsequent dynamics of the coupled quasiparticles. Upon temperature increase the exchange splitting of the surface state decreases from 0.7 eV at 20 K to roughly 0.4 eV at the Curie point and remains constant at this value above $T_C$ up to 360 K (the highest investigated temperature) [33].

The excitation of the phonon-magnon mode depends on the amount of photoexcited electrons and holes produced in the surface state (see the wavelength dependence in the preceding section) by the pump pulse optical transitions, which evolve via the surface

[21] As mentioned in section 5.3 when refer to the coherent phonon and magnon amplitudes we meant the amplitude of the oscillatory features in the transient SH fields and not the real *e.g.* amplitude of lattice vibrations produced by the coherent phonon motion that can be measured only in time-resolved X-ray experiments.

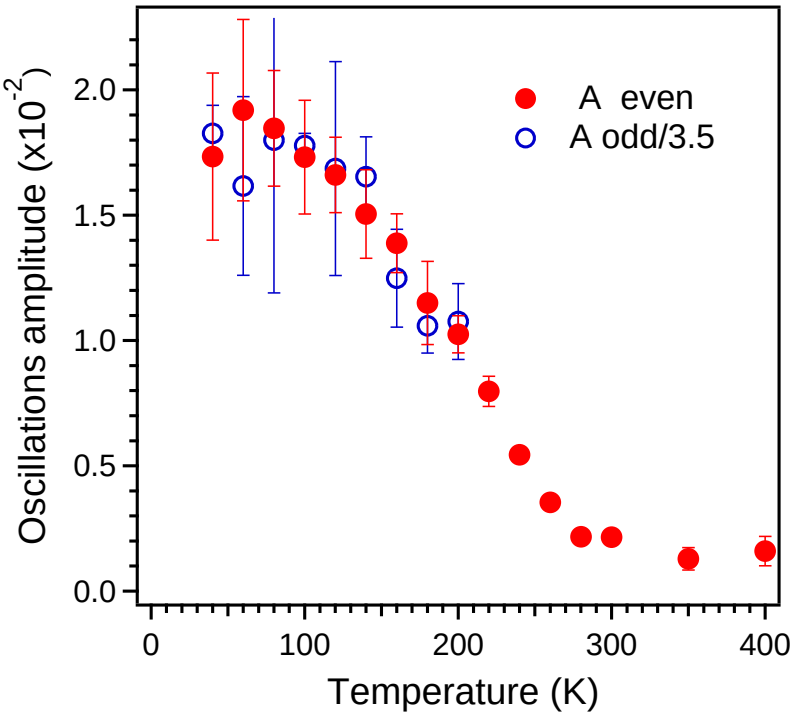


**Figure 5.37:** The amplitude of the coherent phonons (filled circles) and the scaled amplitude of magnons (empty circles) as a function of temperature increase. Note the variation over one order of magnitude of the phonon amplitude and its finite values above $T_C$.

state. Referring now to the spin-resolved DOS at the Gd(0001) surface showed in fig. 5.32 we can explain the temperature dependence as follows. At *low* temperatures and a laser photon energy of 1.55 eV the optical transitions in both channels are active but are dominated by the majority transitions, as has been explained in the previous section. Thus, a selective hole creation in the surface state that is not balanced by the photoexcited electrons, requires a transient charge redistribution for screening in the surface region, that displaces the surface layer from equilibrium position and produces the observed oscillation amplitude. As the temperature increases, both surface state components shift towards $E_F$ *i.e.* the exchange splitting decreases. Having in mind that the optical transitions in the majority channel have a weak spectral dependence due to the energetically broad final state (see preceding section), the temperature increase will produce, gradually, a better fulfillment of the SHG resonance condition in the minority channel *i.e.* a better laser photon energy matching between the spin-down bulk and surface state. Thus, as the temperature is varied, the majority channel gives a rather constant[22] contribution

[22] As shown in section 5.1, modelling the SHG response with a double resonance scheme the contribution from majority channel has been found to be small in comparison to the contribution of the minority channel to the total resonance condition. Thus the overall temperature induced variations of the weak contribution of the majority channel can be considered constant with regard to the minority channel contribution to the excitation process.

to the excitation process while the contribution from minority channel increases as the photon energy matches better the energetic separation between the bulk and the surface state. Increasing contribution of the minority channel results in an increasing amount of photoexcited electrons in the $S^{\downarrow}$ surface state that balances the photo-generated holes in the surface state. Thus a weaker charge redistribution is necessary, that produces a smaller lattice displacement and therefore a smaller coherent phonon and magnon (up to the temperature where can be resolved) amplitude. According to our explanation the excitation probability and consequently the phonon amplitude is varying with the decreasing exchange-splitting of the surface state. Above $T_C$ the $\Delta_{ex}$ is constant up to the highest studied temperature of 360 K [33] and we can use this fact to check our explanation. Indeed we observe a constant coherent phonon amplitude (see fig. 5.37) that confirms the availability of the proposed explanation.

Another experimental support for this interpretation is provided by the dependence of the total SHG yield versus temperature. As shown in figure 5.38, the SHG intensity increases in two times as the temperature is elevated showing the typical behavior of the SHG resonance enhancement (see fig. 3.2) as suggested also by the lorentzian fit of the measured data. Assuming that, mainly, the shift of the $S^{\downarrow}$ surface state is responsible for the SHG enhancement (majority channel has been considered to have a weaker contribution), than the above proposed picture is confirmed. The figure 5.38 shows that the resonance maximum is achieved in the range 220 K to 260 K followed by a signal decrease to the initial level, which indicates less fulfillment of the SHG resonance condition. Hence, above 260 K the amount of unbalanced charge starts to increase again which according to the excitation mechanism will increase the coherent mode amplitude. We do not observe this feature and it is most likely due to the increased thermal population that scatters with the coherent mode, that will be in detail discussed later in this section. Thus the above results support the proposed model of a transient excitation probability with the temperature-dependent shift of the surface state, the latter one being reflected in the resonance enhancement of the SHG process.

Summarizing this part, upon temperature increase the amplitude of the coherent phonons and magnons decreases, that is ascribed to a temperature-dependent excitation probability of the surface state population. The latter one is determined by the initial amount of photoexcited electrons and holes in the surface state, that varies with the exchange splitting of the surface state for a constant laser photon energy.

#### Relaxation of the coherent phonon-magnon mode

Regarding the damping of the coherent phonon-magnon mode various scattering processes might contribute. As has been shown in chapter 2, elastic and inelastic scattering events are responsible for the decay of a coherent mode. Elastic scattering leads to a loss of the coherence with no energy transfer, as is the case for scattering with defects [75]. Inelastic scattering determines changes in the momentum and energy of the involved scattering partners, this process being known as decay or energy relaxation (see chapter 2 for details).

Evaluation of the relaxation time of the coherent phonon-magnon mode can be done according to Matthiessen's rule [135] as the sum of the scattering rates determined by the

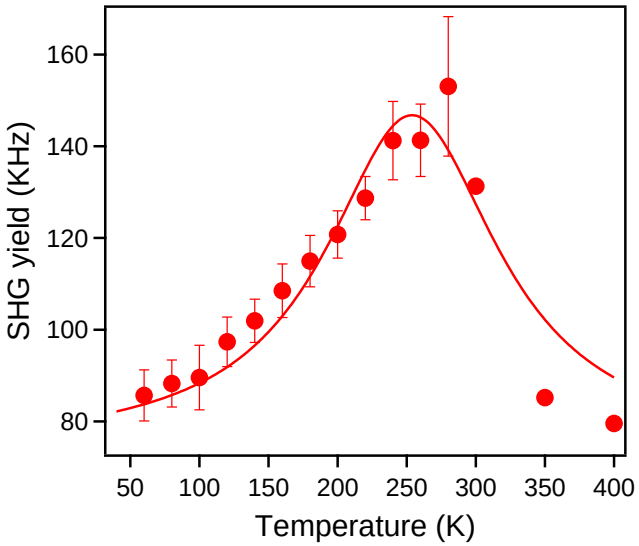


**Figure 5.38:** The variation of the total SHG yield (the solid circles) as a function of temperature. As suggested by the lorentzian fit (the solid line) of the data, the SHG process encounters a resonance enhancement as the temperature is elevated, due to the decrease of the surface state exchange splitting (for details see text). The maximum enhancement of the SHG signal is reached around 250 K.

total inelastic and elastic scattering events that contribute:

$$\frac{1}{\tau} = \frac{1}{\tau_e} + \frac{1}{\tau_i} \tag{5.11}$$

where the $\tau^{-1} = \Gamma$ defines the scattering rate. In time-domain measurements one can determine $\tau$ as the decay time of the oscillatory components of the time-resolved signal.

For the case of coherent phonons on semimetals and semiconductors [76, 77] the dominant decay mechanism has been identified to be the phonon-phonon scattering or the *anharmonic decay* (see chapter 2 and figure 2.10). This decay process, that accounts for the anharmonic corrections of the vibrational potential, describes (in the first order) the decay of an optical phonon of energy $\hbar\Omega$ decays in two acoustical phonons with opposite wavevectors and energy $\hbar\Omega/2$. In the case of metals, has been shown by Hase *et al.* [64] that the same phonon-phonon scattering mechanism plays also the major role in the coherent phonon decay with a weak influence of the coherent phonon-electron scattering.

The case of the coupled phonon-magnon mode on Gd(0001) is more complex in terms of the decay process since we have an additional degree of freedom namely the magnon subsystem. Moreover, Gd is a metal that implies an efficient scattering of the coherent mode with electrons. The latter process might be enhanced at the surface due to the laser resonant absorption in the surface state. Thus, several processes might contribute to the decay of the coherent phonon-magnon mode, and presumably with different relative weights. Therefore, identification and quantification of their contribution in not a trivial task. However, the present temperature-dependent study could demonstrate the presence of a few relaxation channels that are described in the following.

It is worthwhile mentioning the possible scattering events that might influence the decay of the coherent mode for Gd case. The coherent phonons and magnons might scatter with thermal phonons and magnons as well as with defects. Also, the coherent phonon-magnon mode can decay through excitation of an electron-hole pair via phonon-electron

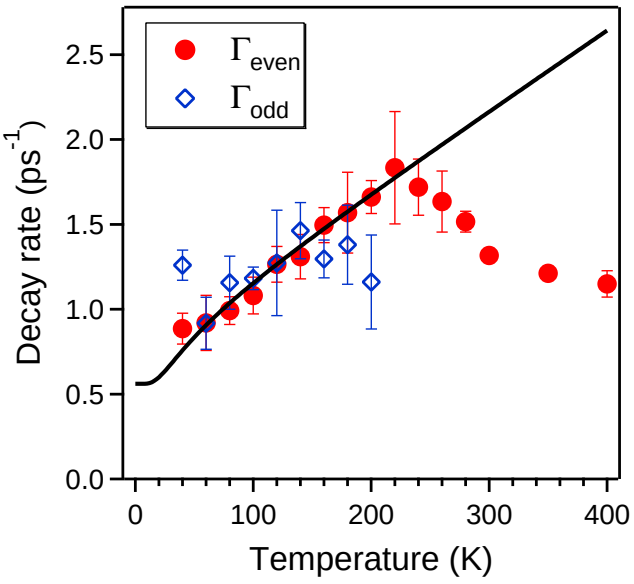


**Figure 5.39:** Temperature-dependent evolution of the decay rate for the coherent phonons (filled circles) and magnons (empty diamonds). Note the non-monotonous behavior of the coherent phonon decay rate, that changes its tendency around 220 K. A fit (the solid line) according to eq. 5.12 which accounts for the scattering of the coherent phonons with electrons and thermal phonons describes well the data at lower temperatures but gives a monotonous increase of the scattering rate over the whole temperature range.

and magnon-electron interaction. Thus one can write the relation 5.11 for the total scattering rate under the form:

$$\Gamma = \Gamma_{cp} + \Gamma_{cm} = \Gamma_{cp(cm)-e} + \Gamma_{cp(cm)-p} + \Gamma_{cp(cm)-m} + \Gamma_{cp(cm)-def} \tag{5.12}$$

where the $\Gamma_{cp}$ and $\Gamma_{cm}$ denote the scattering rates for the coherent phonons and magnons, respectively, each consisting of terms describing the scattering with electrons, thermal phonons, thermal magnons and with defects. As will be shown later, one can separate these contribution accounting for their temperature dependent behavior: an elevated temperature increases the thermal electron and phonon population described by Fermi-Dirac and Bose-Einstein distribution functions, respectively.

The behavior of the decay rate of the coherent phonon-magnon mode versus temperature is presented in figure 5.39. The decay rate $\Gamma$ is deduced from the damping time $\tau$ obtained by fitting the oscillatory SH fields with the expression 5.8. Upon elevating the temperature, the decay rate for phonons monotonously increases up to 220 K where a turning point in its behavior is encountered. The decay rate for magnons has a significantly increased error bars due to the lower signal to noise ratio of the odd SH field. Within the error bars of the magnon data we can say that we observe a constant decay rate over the temperature interval where the coherent magnons contribution can be resolved. Owing to the better signal to noise ratio detected for coherent lattice mode, we focus in the following on the coherent phonon behavior.

The decay rate of the coherent phonon shows a linear increase with temperature up to 220 K where an interesting feature is observed namely the decay rate starts to decrease *i.e.* the decay time increases although the amount of scattering partners (phonons, magnons, electrons) increase. Accounting for the scattering with thermal phonons the decay rate should exhibit a linear behavior [76] with increasing the temperature. Since the excitation of the coherent mode is due to a resonant absorption in the surface state, which means a significant amount of photoexcited carriers in the surface region are involved, we consider also

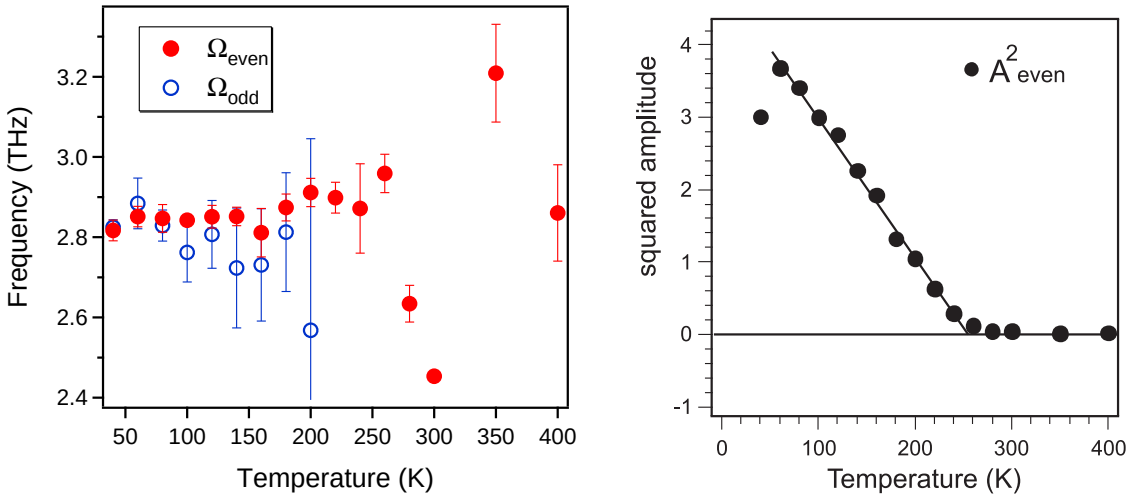


**Figure 5.40:** The dependence of the coherent phonons (filled circles) and magnons (empty circles) frequency versus temperature. Note the drop in the coherent phonon frequency as the temperature approaches the Curie point.

the scattering events of the coherent phonon with electrons. The temperature-dependent distribution functions of electrons and phonons render the scattering probability with the coherent phonon because they account for the increased electron and phonon population with temperature. Thus we can evaluate the contribution of the electrons and thermal phonons to the total scattering rate of the coherent phonon as [64, 76]:

$$\Gamma = \Gamma_{cp-p} \cdot \left(1 + \frac{2}{e^{\frac{\hbar\Omega}{2k_BT}} - 1}\right) + \Gamma_{cp-e} \cdot \left(1 + \frac{2}{e^{\frac{\hbar\Omega}{2k_BT}} + 1}\right) \tag{5.13}$$

where the terms on the right-hand side denote the decay rate of an optical phonon of energy $\hbar\Omega$ into two acoustic phonons of energy $\hbar\Omega/2$ and into an electron-hole pair, respectively. In the last term of eq. 5.13 the effect of a hot electron distribution is not included for simplicity. The terms $\Gamma_{cp-p}$ and $\Gamma_{cp-e}$ in the above equation account for the scattering probability of the coherent phonon with thermal phonons and electrons, respectively. Fitting the measured decay rate of the coherent phonon with the above expression up to a temperature of 220 K one obtains a good description of experimental data (the solid line in fig. 5.39). Using a coherent phonon frequency of 2.9 THz in expression 5.13 the scattering rates $\Gamma_{cp-p}$=0.17 ps$^{-1}$ and $\Gamma_{cp-e}$=0.35 ps$^{-1}$ ( that are the only fitting parameters) are obtained. As deduced from the values of the scattering rates the electron-coherent phonon collision events are more frequent than phonon-phonon scattering. Considering only these two scattering channels the decay rate would continue to increase with increasing temperature, as can be noticed in figure 5.39. Instead, we observe a decreasing of the scattering rate which is tentatively assigned to the effect of the coherent magnon decoupling. We shall explain the decay scenario in the following.

As the temperature of the system is elevated the scattering of the coherent mode with electrons, phonons and magnons increases. Analogous to the coupled oscillators system

the coupled phonon-magnon mode oscillates with a common (normal) frequency of 2.9 THz until one oscillator is decoupled (the magnon). The excitation energy residing initially in the coupled system is conducted now to the coherent phonon only. Moreover, the additional decay channels active for the coherent magnon (thermal magnon, phonon, electron), that were acting on the coupled mode as a whole, are now silent. A release of one oscillator should be accompanied by non-monotonous changes in frequency and energy of the remaining oscillator. We observe such a frequency modification in the temperature range where the magnon signature in the transient signal vanishes (see left panel of figure 5.40). At the same temperature of 260 K we notice a change in the energy of the coherent phonon oscillator $E \propto A^2$ [160] (see eq. 5.10), as can be seen in right panel of figure 5.40. Note, that above 260 K the energy is not zero but is finite small due to the reduced amplitude in this temperature range (see fig. 5.37).

These two observation might explain the observed decreasing of the decay rate. However, in order to confirm these proposals, higher density of data points in the vicinity of $T_C$ are required and measured with a better statistics. For a thorough understanding of the decay rate of the coherent mode also a theoretical input would be valuable.

### Conclusion

Temperature-dependent measurements of the MSHG signal from the Gd(0001) surface have been performed between 40 and 400 K. The incoherent and coherent components of the MSHG response revealed the existence of various decay channels that exhibit a complex interplay and affect the dynamics of the electron, lattice and spin subsystems. The observed changes with temperature in the incoherent $\Delta_{even}$, evaluated at electron-phonon equilibration time of 3 ps, resemble qualitatively the temperature-dependent variation of the exchange splitting of the surface state. Based on this observation, a model has been proposed in which the temperature-dependent shift of the $S^{\downarrow}$ surface state results in a various levels of photoexcited electron densities, that are responsible for the variation of the incoherent $\Delta_{even}$. The incoherent $\Delta_{odd}$ is mainly affected by the temperature increase in the sudden drop exhibited at early delay times. Its increasing value with the temperature increase has been attributed to higher density of spin-mixed states available for electronic spin-flip scattering. Regarding the dynamics of the coherent phonon-magnon mode, the coherent magnon could be resolved up to 200 K while the coherent phonon has been measured over the entire investigated temperature range. The coherent phonon amplitude varies over one order of magnitude as the temperature is increased that is explain by a changing excitation probability with reducing the exchange splitting of the surface state. We observe the coherent phonons also above $T_C$ that proves the existence of an exchange-split surface state despite the loss of long-range magnetic ordering. The decay rate of the coherent phonon exhibits a non-monotonous behavior with temperature, that is ascribed to the combined effect of scattering with thermal phonons and electrons and presumably to the coherent magnon decoupling.

### 5.5.3 Conclusions

Systematic study of the incoherent and coherent MSHG response from the Gd(0001) surface has been performed by varying the laser wavelength and the static temperature of the system. Investigating the photon energy range between 1.44 and 1.68 eV, we observe significant changes of the MSHG response. A complex spectral behavior of the even SH field is observed, that is determined by the competition between the coherent and incoherent SHG components as the photon energy is varied. This behavior has been ascribed to the various levels of photoexcited carriers in the surface state, that produces (*i*) the spectral behavior of the coherent phonon mode and (*ii*) their thermalization (of the initially excited electrons and holes) is reflected in the incoherent part. Thus, the wavelength-dependent measurements gives evidence for a charge-driven excitation mechanism of the lattice and spin coherence. These results emphasize the cental role of the exchange-split surface state in the SHG process from Gd(0001) surface, that causes the high spectral sensitivity due to the spin selective optical transitions via the surface state components. Measurements within the temperature interval 40 K to 400 K show gives a further support for a charge-driven excitation mechanism of the coherent phonon-magnon mode. The amplitude of the coherent phonon could be traced well above Curie point, that indicate the presence of a residual exchange-split surface state above $T_C$ in agreement with the literature [33, 36], and confirming the spin-mixing behavior of Gd(0001) on ultrafast time scales (see section 5.2.1). At low temperatures the main decay channels of the coherent phonon-magnon mode are the scattering with the electrons and thermal phonons. The scattering with electrons gives the major contribution to the total decay rate. In the high temperature range (T$>$ 200K) the total decay rate decreases, which is tentatively ascribed to the effect of the coherent magnon decoupling.

## 5.6 Coupled coherent phonon-magnon mode: the effect of film thickness and morphology changes

Here we investigate the effects of the reduced film thickness and of morphological modifications of the Gd(0001)/W(110) films on the dynamics of the linear and nonlinear optical response. Lowering the film thickness, of particular interest is the possibility of excitation and detection of interface phonon modes. Also a reduced thickness lowers the phase space for the relaxation of the photoexcited electrons, that results in higher energy densities residing into the system[23], which can influence both the incoherent and coherent SHG components. The second part of the present section is devoted to the results obtained upon modification of film morphology *i.e.* from a layer-by-layer mode to three-dimensional islands and its effect on the coherent and incoherent dynamics of the SHG response.

[23] Assuming a negligible energy transport out of the excited region by non-equilibrium electrons *i.e.* ballistic transport (see chapter 2).

### 5.6.1 Film thickness effects

Nominal film thicknesses between 15Å (≈5 ML) and 200Å (≈67 ML) have been studied with the laser tuned at a wavelength of 800 nm and at a sample temperature of 30 K. Lower thicknesses are not investigated due to the vanishing magnetic contrast (*e.g.* for the 15Å film the contrast is 0.5%) and the lack of a well developed surface state[24]. The preparation of films with lower thickness has been done following our standard procedure (see chapter 4) used for growing epitaxially thin Gd(0001) films on the W(110) substrate. This consists in depositing gadolinium at room temperature on the W(110) substrate followed by annealing to a temperature situated below the threshold temperature at which the film splits into islands [121]. The structural ordering of the films has been checked by LEED. The film thickness has been monitored by a quartz microbalance and additionally we have used the reduced Curie temperature [136] of the lower thickness films as a criterion for the thickness calibration. The resulting error in the thickness reading is evaluated at ≈10%. The finite-size scaling law[25], that quantifies the change in the Curie temperature with thickness variation reads [136]:

$$\frac{T_C(\infty) - T_C(d)}{T_C(\infty)} = c \cdot d^{-\lambda} \tag{5.14}$$

where $T_C(\infty)$ and $T_C(d)$ the bulk and the reduced Curie temperature, respectively, $d$ is the film thickness, $\lambda$ is the critical exponent related with the range of magnetic ordering, $c$ is a phenomenological constant. For Gd the bulk Curie temperature is $T_C(\infty)$=293 K and for Gd(0001) film thicknesses in the range of 60–70 ML (≈200 Å) the reduced Curie temperature $T_C(d)$ tends asymptotically to $T_C(\infty)$ [136].

First results showing the transient behavior of the even and odd SH fields for various thicknesses are displayed in figure 5.41 and 5.42, respectively. Regarding the $\Delta_{odd}$ behavior, we show the measurements for thicknesses above 50Å since below this thickness the magnetic contrast is reduced close to zero value (see figure 5.43) and consequently a high level of noise is present, that hinders any attempt to retrieve the coherent and incoherent components of the signal. As the thickness is varied we observe in both transient SH fields a rich dynamics that involves the incoherent and coherent fractions of the SHG response. Referring to the transient even SH field displayed in fig. 5.41, we notice the presence of an oscillatory component even for the lowest thickness *i.e.* 15Å, with the amplitude increasing with increasing thickness. The pump-induced variations in the incoherent $\Delta_{even}$ increase their absolute value with thickness, seems to saturate around 100Å and simultaneously change their time-dependent profile. The behavior of $\Delta_{odd}$ plotted in figure 5.42 shows also interesting features upon changing the thickness. The initial drop at early times reaches the -1 value for the 50Å film, that reflects a total loss of spin polarization, and is followed by a rapid relaxation to an intermediate constant level. Such behavior is not observed for larger thicknesses, for which the initial drop scales inverse proportionally with the thickness and the time-dependent profile is the usual one, as observed earlier (see fig. 5.21).

[24] According to STS measurements [33] on Gd(0001), a well developed exchange split surface state is present for film thickness bigger than 4 ML ≈ 12Å

[25] The finite-size scaling law is determined by the different exchange coupling acting on the surface and bulk atoms due to their different coordination number. As a function of thickness their ratio is changing and consequently the $T_C$.

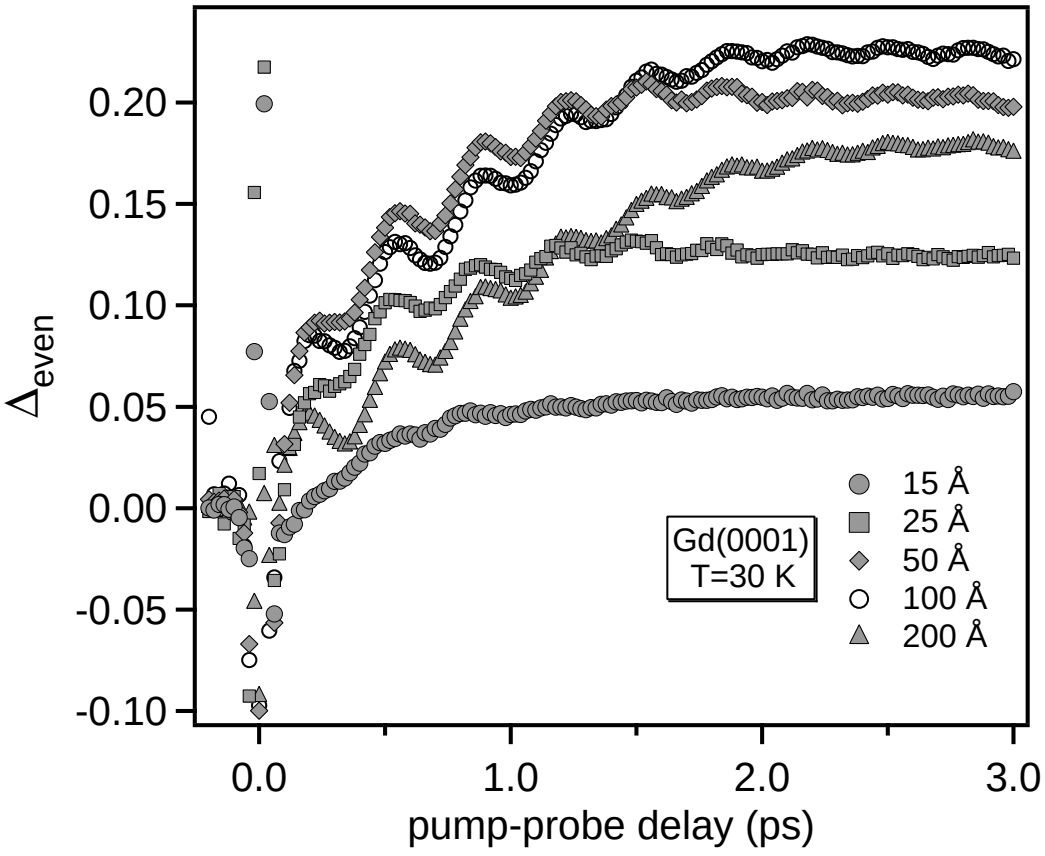


**Figure 5.41:** Pump-induced variations in the even SH field measured at T=30 K on epitaxially grown Gd(0001)/W(110) films with various thicknesses. Notice the presence of oscillatory component even for the lowest investigated thickness of ≈5 ML Gd.

The oscillatory component of $\Delta_{odd}$ resembles the opposite trend of that encountered in $\Delta_{even}$ namely amplitude is larger for low thickness and decreases with increasing the film dimensions.

Another important piece of information regarding the system modification with thickness is provided by the SHG signal and the magnetic contrast. Their behavior versus film thickness is displayed in the figure 5.43. Within the scattering of the data points we observe a rather constant SHG yield and simultaneously an increase by more than one order of magnitude for the magnetic contrast. The constant level of the SHG signal, that is resonantly enhanced via the surface state (see the preceding sections), can be related to the exchange splitting of the surface state, which remains constant as the Gd(0001) film thickness increases [33]. The behavior of the magnetic contrast indicates a better magnetic ordering at the surface as the thickness increases or reflects the effect of an increased bulk magnetization on the surface magnetic ordering. An additional explanation is that the MSHG response is sensitive to the bulk magnetization, which increases with the film

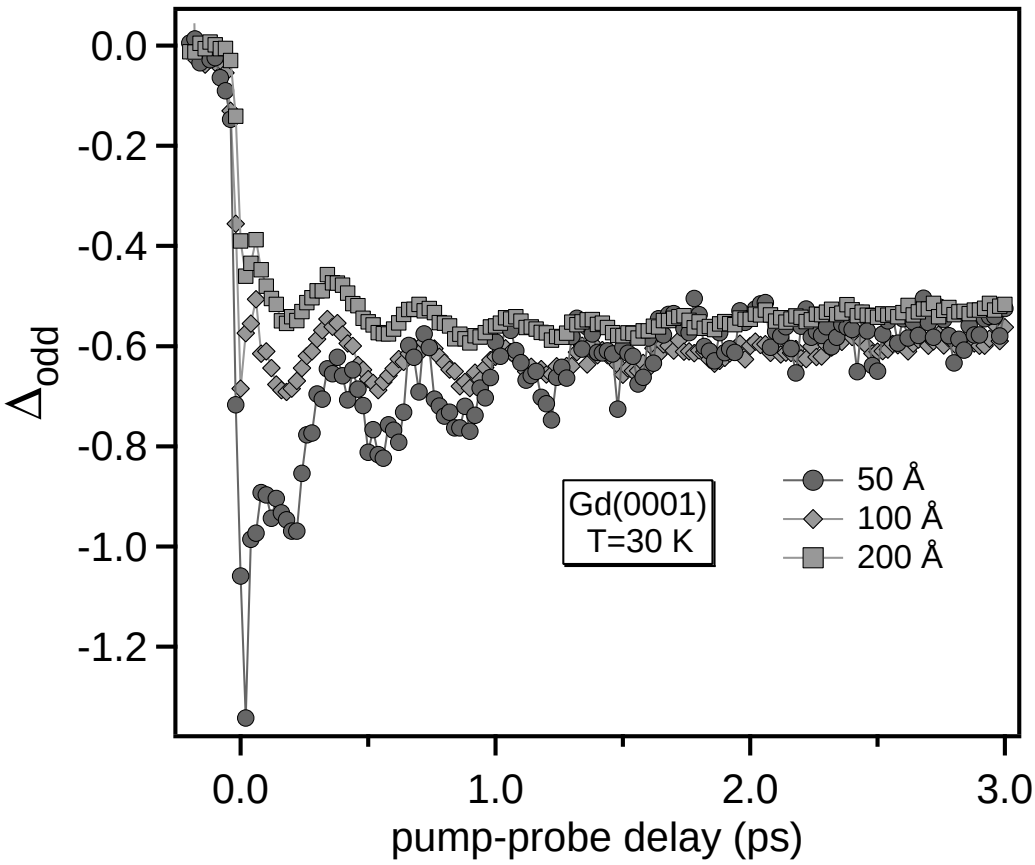


**Figure 5.42:** Pump-induced variations in the odd SH field measured at T=30 K on epitaxially grown Gd(0001)/W(110) films with various thicknesses. We do not show here the measured data for 15Å and 25Å because of the high level of noise (due to the vanishing magnetic contrast).

thickness. Such an intriguing possibility is discussed later in this section.

In order to get quantitative information about the oscillatory component of the SHG signal, we have separated the coherent and incoherent fractions of the signal using the procedure presented in section 5.3. The resulting variations in the amplitude, frequency and decay time of the coherent lattice and spin excitations with the film thickness are displayed in figure 5.44. One of the first observations is the opposite trend of the coherent phonons and magnons amplitude *i.e.* upon increasing the film thickness the phonon amplitude increases in approximately five times while the magnon amplitude decreases in roughly three times. The second observation is the appearance of a saturation behavior in the amplitudes of lattice vibrations around 100Å film thickness, as suggested by the dashed line in the top panel of fig. 5.44. A similar saturation behavior is observed for this thickness also in the pump-induced variations of the incoherent $\Delta_{even}$ (see fig. 5.41). Regarding the frequency of the coupled quasiparticles (plotted in the central panel of fig. 5.44), no major changes (within the error bars) of the 2.9 THz frequency value measured

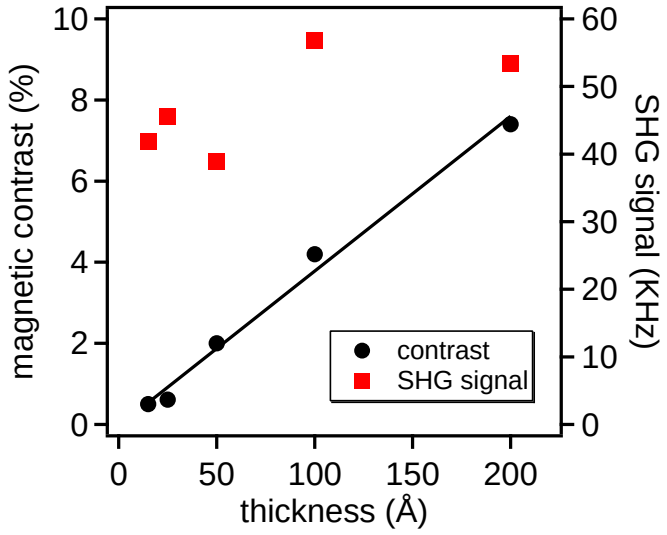


**Figure 5.43:** The variation of the SHG signal and of the magnetic contrast with the Gd(0001) film thickness, measured at a temperature of 30 K. The solid line is a guide for the eye.

on 20 nm films are observed upon varying the film thickness. Also no other frequencies have been observed that would indicate the presence of phonon (magnon) modes located at the interface. The decay time (bottom panel of fig. 5.44) shows a slight increase with increasing thickness (from 1 ps to 1.4 ps) for the phonon mode while for the magnon is centered around a value of 1.2 ps (within the error bars).

### Discussion

Before we start any discussion regarding the experimental results, we point out that owing to the preliminary character of these measurements we cannot formulate strong conclusions and rather we indicate some possible interpretations that are subject of future investigations. However, although the presented data are first measurements, the main trends in their dynamics are already discernible.

We address in the first place the oscillatory components of the transient even and odd SH fields. As pointed out earlier, the signature of the coherent phonon can be resolved down to a thickness of 5 ML, as can be seen from the top panel of figure 5.44. Increasing the thickness the coherent lattice amplitude increases in five times up to a rather constant[26] value that is maintained for thicknesses above 100Å . Simultaneously the coherent phonon decay time increases slightly with thickness to a value of 1.4 ps (see bottom panel of fig. 5.44). These observations suggest that the decay process of the coherent lattice motion becomes weaker as the thickness grows. In a simple picture, no change in the oscillatory behavior of the coherent mode is expected by changing the film thickness due to its localization at the surface. In reality, the underlying bulk of the film can exhibit

[26]Here a higher density of measured data points would be helpful in order to check the constant level.

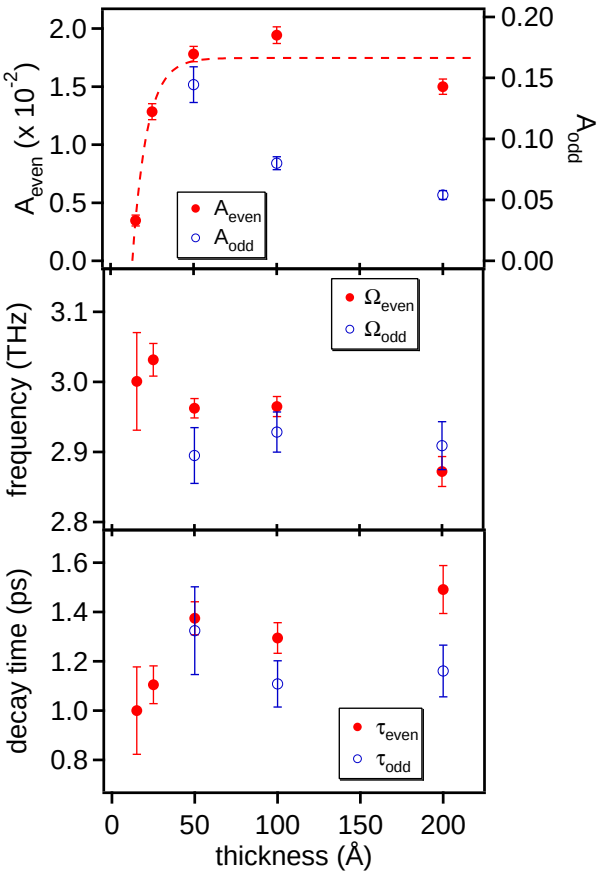


**Figure 5.44:** The amplitude, frequency and the decay time of the oscillatory component of the MSHG transients (from fig. 5.41 and 5.42), measured for various Gd(0001) film thicknesses at T= 30 K. The dashed line in the top panel is a guide for the eye indicating a saturating behavior exhibited by the coherent phonon amplitude.

various degrees of defects that affect the long-range crystalline ordering and consequently the film surface also. Thus a possible explanation of the phonon mode behavior relies on the strain that is build-up in the film due to the film-substrate lattice mismatch. It has been shown [146, 147] that the presence of strain can change the binding energies of surface states. In our case this will affect the excitation probability of the coherent mode (see the preceding section) and the SHG resonance condition. However, STS measurements [33, 34] reveal a well developed surface state starting with 4 ML Gd(0001) film and no changes in its binding energies for bigger thicknesses. Also we do not observe significant changes in the SHG yield as a function of thickness, that would indicate a modification of the SHG resonance due to a change in the energetic positions of the surface state. Thus we can neglect in this context the effect of strain on the Gd(0001) surface electronic structure. On the other hand, an earlier work shows [24] that starting with 4 ML the induced strain in the Gd(0001) film is reduced to ≈75% of its initial value and is totally released after

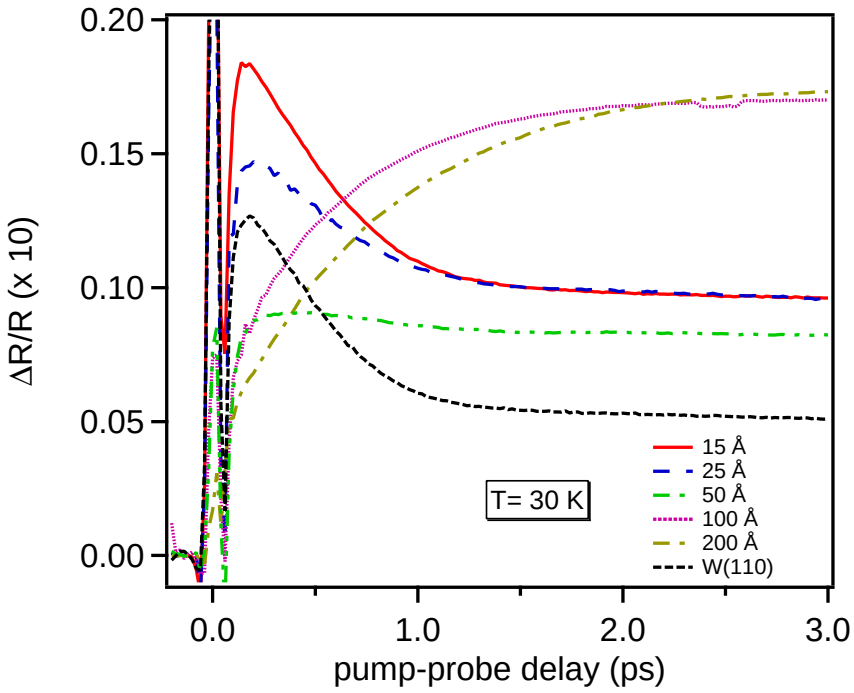


**Figure 5.45:** The pump-induced changes in the linear reflectivity measured from Gd(0001) films with different thicknesses and from the clean W(110) substrate, at T= 30 K. Note the radical change in the time-dependent profile in ΔR/R for the 100Å data set with respect to lower thicknesses. The transient linear reflectivity is measured simultaneously with the SHG response.

≈30 ML. This thickness fits well with the observed thickness interval in the figure 5.44 where the amplitude of the coherent phonon becomes constant. Thus one can consider the structural defects or dislocations produced by the strain presence and strain release in the Gd(0001) film, to explain the lower amplitude and decay time of the phonon mode at low thicknesses via the elastic scattering of the coherent mode with defects.

Another potential candidate is the Gd-W interface contribution to the total SHG response, that can interfere constructively or destructively with the surface part of the nonlinear polarization, according to their mutual phase relationship. As mentioned in chapter 4, we have selected the 20 nm film thickness as the typical thickness for our experiments, since for this film dimension the interface should have no or a negligible contribution to the SHG response based on the optical penetration depth $\delta \approx 20$ nm. Thus for lower thicknesses the film-substrate interface should contribute. One experimental indication that the interface plays a role in the SHG process comes from the pump-induced variations in linear reflectivity plotted in figure 5.45. In the same figure we have plotted for comparison also the transient linear reflectivity measured on clean W(110) substrate. Since LR is bulk sensitive within the optical penetration depth, it is probing the whole Gd film, and for thicknesses smaller than the skin depth is sensitive also to the tungsten substrate. This is apparent for film thicknesses up to 50Å for which the signature of the substrate

can be clearly distinguished *i.e.* similar shapes of the transient profiles. For the 100Å film we observe a totally changed time-dependent profile, that closely resembles the one of the 200Å film thickness. Fitting the LR measurements (not shown for clarity) with a model function accounting for the relative contributions of the substrate and Gd film to the transient LR, we obtained a W:Gd ratio ranging from ≈1:10 to ≈1:40 for the thickness range from 50Å to 100Å, respectively. Thus we can say that in the thickness range 50Å to 100Å the substrate contribution to the LR signal is strongly reduced and above 100Å is very small[27]. For thicknesses ranging from 50Å to 15Å, for which the substrate is contributing to the transient LR, we observe a gradual decrease in the oscillatory and incoherent SHG components as the thickness decreases (see fig. 5.44 and fig. 5.41). Thus one can consider a Gd-W interface contribution to the SHG response that might interfere (partial) destructively with the surface contribution (coherent and incoherent) to explain the observed decreasing in the coherent and incoherent SHG fractions.

Regarding the transient $\Delta_{odd}$ behavior, plotted in fig. 5.42, we observe an interesting feature for the 50Å film thickness. At early delay time the initial drop in $\Delta_{odd}$ reaches[28] -1 value, that is equivalent to a total loss of spin polarization of the surface state. We have explained in section 5.2.1 the initial drop of $\Delta_{odd}$ as being determined by the hot electrons spin-flip scattering among spin-mixed states. This proposed demagnetization mechanism describes very well the encountered $\Delta_{odd}$ behavior for the wavelength- and temperature-dependent data in the preceding sections. Here we cannot use it to explain the measured data since decreasing the thickness neither the density of spin-mixed states nor the population of hot electrons increases. In principle one can utilize the same argument of interface contributions, that are active up to 50Å and diminish as the thickness grows. This point is supported also by the different time-dependent profiles of $\Delta_{odd}$ for the 50Å thickness in comparison with the 100Å and 200Å measurements. Also we cannot exclude the effect of the relative phase between the SH fields (see section 5.1), that has been shown to change with the film thickness [127, 132]. However, based on the actual experimental input we cannot make any statements and this point requires further investigations.

Finally we discuss the possibility that the SHG technique might be sensitive to the bulk magnetization. This possibility arises from the measured behavior of the magnetic contrast $\rho$ versus thickness (see fig. 5.43) *i.e.* a monotonous increase of $\rho$ with increasing thickness. Increasing the thickness of a ferromagnetic film results in an increased value of the total magnetic moment of the specimen. But how can a bulk property can be detected by the SHG, which is considered to be a surface sensitive technique?

As shown in chapter 3, for centrosymmetric media and within electric-dipole approximation the nonlinear source of the SHG signal is constrained at surfaces and interfaces where the inversion symmetry is broken. In the nonlinear polarization expression (see eq. 3.19 and 3.20) one can account for higher order terms describing electric quadrupole and magnetic dipole contributions, that are bulk sensitive. These are usually small, but when large bulk volumes are involved their contribution can be of comparable magnitude with the surface contribution. If this is also the case for the higher thicknesses Gd(0001) films,

[27] For the 200Å Gd film the W:Gd ratio is ≈1:80

[28] Actually, the are two data points below -1 value, which are explained by the increased noise level due to the low magnetic contrast of ≈2%.

at this point, is difficult to judge, since separating the surface and bulk contributions to the SHG response is a complex task [100, 117]. Nevertheless, measurements of the polarization dependence from the Gd(0001) sample for various MSHG geometries might help in this respect [117]. In short, the bulk magnetization can be in principle reflected in the SHG response but further measurements are necessary in order to clarify this issue.

### 5.6.2 Morphology effects

In this part we present the effect of a changed Gd(0001) film morphology on the time-resolved nonlinear optical response. Morphology changes refer to the transformation of a smooth film to a three-dimensional(3D) islands structure, upon annealing to high temperatures [121]. Of special interest here is the evolution of the coherent phonon-magnon mode on the 3D Gd islands.

As mentioned in chapter 4, the morphology of the Gd(0001) film can be modified by employing annealing temperatures above a certain threshold limit, for which the film is transformed from the initial layer-by-layer growth mode to a 3D islands film. The critical temperature at which the transition flat film-3D island takes place, has been investigated by Aspelmaier *et al.* [121] for various Gd(0001) film thicknesses. Their results are summarized in the figure 4.3, where the critical annealing temperature is displayed for Gd(0001) film thicknesses ranging from 5 ML to 100 ML. For the preparation of the Gd(0001) islands structure we followed the threshold temperature diagram reported in this work.

For illustration of this structural transformation, STM pictures from literature are reproduced in figure 5.46. Here the effect of different annealing temperatures on a 11 ML Gd(0001)/W(110) film is showed. We see that annealing to a temperature (here 530 K) below the threshold limit of reference [121], a smooth film is obtained showing monoatomic steps whereas annealing to 710 K (above the threshold limit), the film breaks up in 3D islands of quasi-hexagonal shape sitting on top of 1 ML Gd, that covers the substrate. Thus the morphology of the Gd(0001) film changes upon annealing to temperatures above the critical limit, from a smooth film to 3D islands lying on one Gd layer (Stranki-Krastranov-like mode).

As a representative example for the transition from a layer-by-layer to a islands film upon annealing to higher temperatures, we have selected a 50Å ($\approx$ 16 ML) thick Gd(0001) film. According to the critical temperature diagram (see fig. 4.3), the flat Gd(0001) film is obtained after annealing to 550 K while for temperatures higher than 750 K the film is transforming to islands. For this film dimension, and upon annealing to 800 K, we encounter the most pronounced changes in the oscillatory part of $\Delta_{even}$. Also starting with this thickness the interface contribution to the SHG response becomes weaker (see previous subsection). Moreover, STM measurements covering this thickness range are available in literature [33, 34, 123], that render useful information regarding the islands size and shape.

First results showing the time-resolved nonlinear magneto-optical response from a smooth Gd(0001) film and from a three-dimensional islands film, are displayed in the upper and the lower panel of figure 5.47, respectively. The measurements are performed on a 50Å Gd(0001) film at a sample temperature of 30 K and with the laser tuned to 800 nm. The changed morphology affects the SHG response in two ways. First, the period of oscilla-

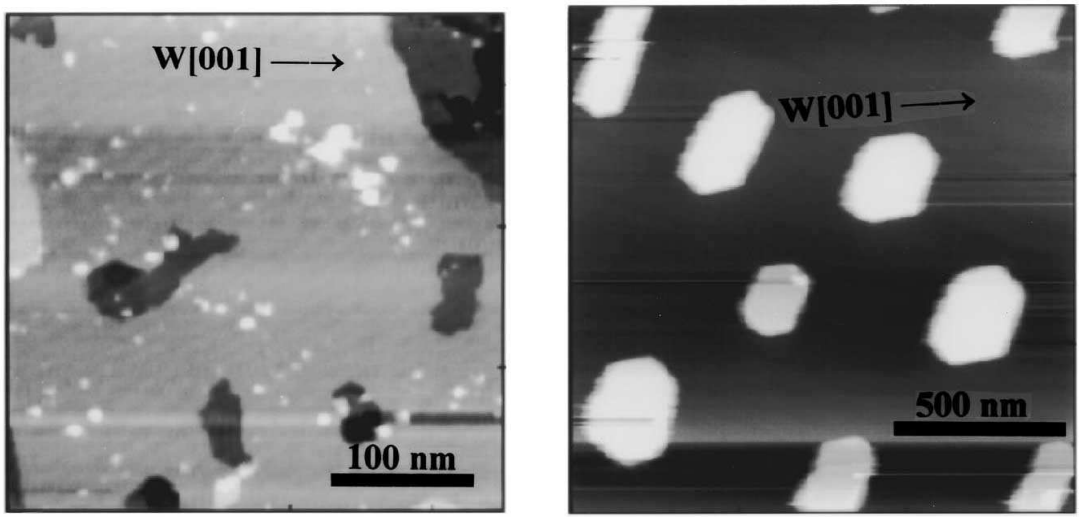


**Figure 5.46:** STM (scanning tunnelling microscopy) measurements of a 11 ML Gd(0001)/W(110) film. **Left:** A smooth and flat gadolinium film obtained after annealing to 530 K. **Right:** Different morphology is obtained upon annealing to 710 K: one can observe 3D islands on top of a completely closed Gd monolayer. From [123].

tions in $\Delta_{even}$ becomes smaller *i.e.* higher frequency, whilst the oscillatory component of the transient odd SH field is not observable anymore. Also the oscillations in $\Delta_{even}$ are much longer lived in comparison with the flat film, with a very clear oscillatory pattern even at 5 ps pump-probe delay. Second, the incoherent part of the transient $\Delta_{even}$ and $\Delta_{odd}$ is changing its time-dependent profile and simultaneously showing considerably lower pump-induced variations.

Since an interesting change in the measured frequency of the coherent phonon mode is encountered, we focus on the oscillatory behavior of the SH response. The coherent and incoherent parts of $\Delta_{even}$ have been separated utilizing the procedure presented in the section 5.3. The resulting oscillatory fraction $\Delta_{even}^{osc}$ is displayed in figure 5.48. Here we observe an oscillatory period of 220 fs, that corresponds to a frequency of 4.5 THz, and simultaneously the presence of a weak beating pattern. The latter observation suggests that more oscillatory modes are involved. In order to obtain the values of the involved frequencies we have Fourier transformed the oscillatory data from fig. 5.48 with the result plotted in figure 5.49. The Fourier transformation reveals the presence of three frequency modes in the oscillatory part of $\Delta_{even}$. There is a high amplitude mode centered at 4.5 THz that dominates the frequency spectrum, together with smaller amplitude peaks at 3 THz and 10 THz. The 3 THz mode represents the coherent phonon measured on the flat film, that is accompanied by two unknown frequency modes. The 4.5 THz mode is very long lived as can be seen in fig. 5.48, while the 10 THz mode has a short lifetime accounting for its broad width in the frequency spectrum. For a quantitative evaluation of the parameters (amplitude, frequency, decay time) of the oscillatory $\Delta_{even}$, we have utilized an extended version of the fit function 5.8, that consists of three exponentially damped oscillatory modes. The obtained fit (the solid line in the figure 5.48) shows a good

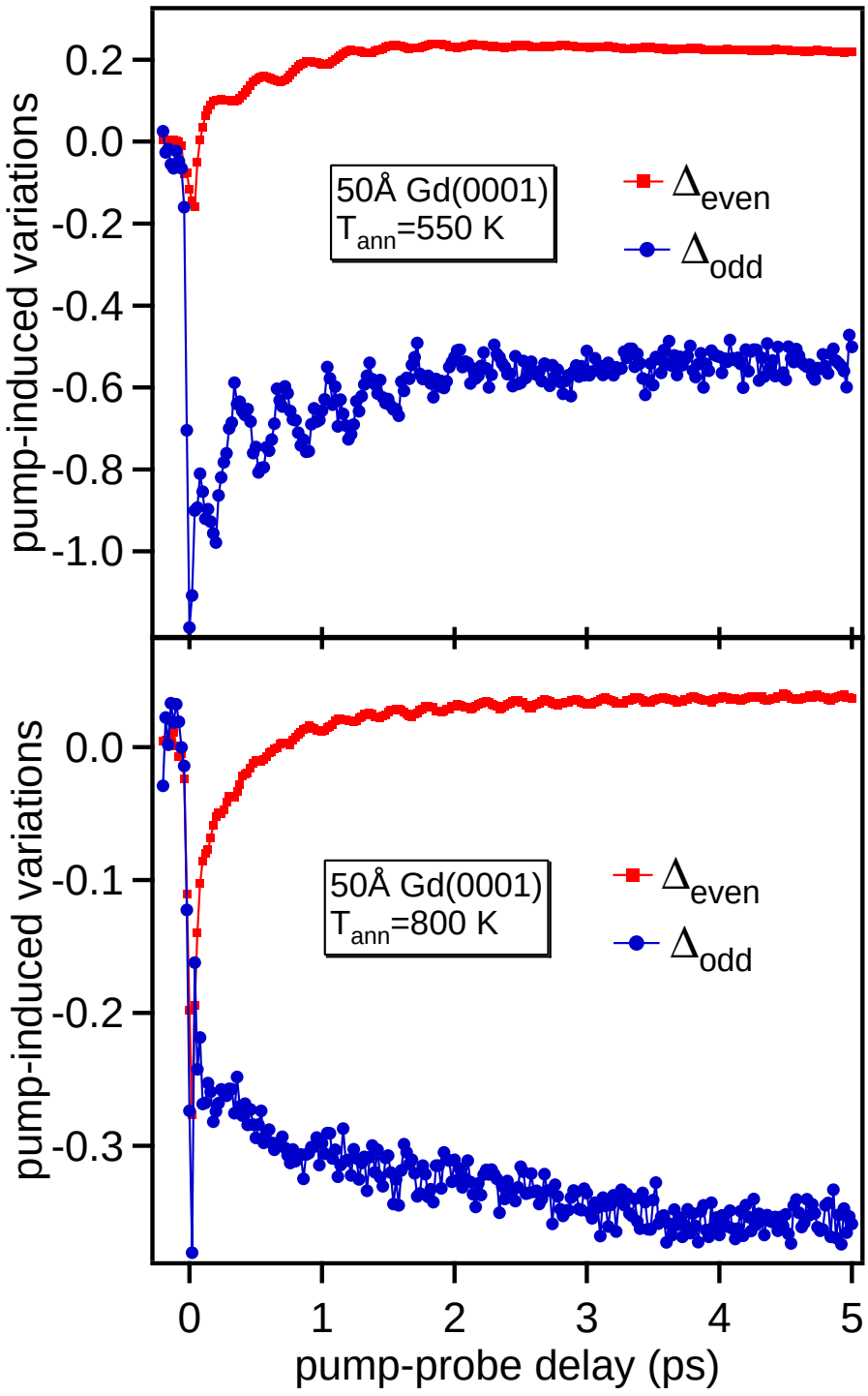


**Figure 5.47:** The pump-induced variations in the SH fields, for a 50Å Gd(0001) film, measured for two different annealing temperatures. Annealing to 800 K produces a change in the period of the oscillatory component of $\Delta_{even}$ while the oscillations in $\Delta_{odd}$ cannot be resolved anymore. Also the time-dependent profile of the incoherent components of the SH fields is changed.

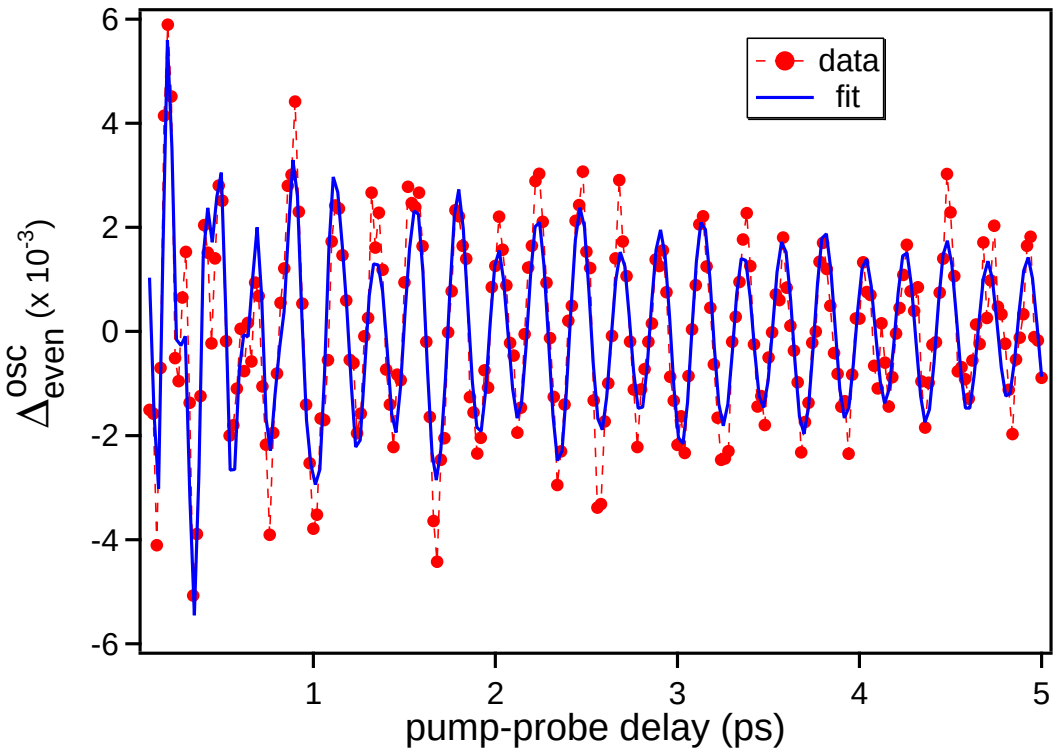


**Figure 5.48:** The oscillatory component of the $\Delta_{even}$ measured from a 50Å Gd(0001) island film (the lower panel of figure 5.47). The solid line represents a fit according to an extended version of eq. 5.8, which accounts for the damped oscillatory motion of the three modes. Note the beating structure of the oscillatory fraction that is clearer in the fit curve.

reproducibility of the measured oscillatory data. The extracted fit parameters are listed in the table 5.1.

As already discernable from the raw data, the 4.5 THz mode is the longest lived mode with ≈8 ps decay time, followed by the 3 THz mode with ≈2.5 ps lifetime and the short lived 10 THz mode with ≈0.5 ps. For a clearer picture of the time evolution of the encountered frequency modes we have performed, in addition, a time-frequency analysis of the oscillatory $\Delta_{even}$ data. For this a Wigner transformation [161, 162] of the time-domain os-

| | Frequency (THz) | Decay time (ps) | Amplitude |
|---|---|---|---|
| Mode 1 | 3±0.01 | 2.48±0.6 | 0.0013±0.0002 |
| Mode 2 | 4.47±0.002 | 7.8±1.4 | 0.0027±0.00015 |
| Mode 3 | 10±0.036 | 0.46±0.08 | 0.0011±0.0006 |

**Table 5.1:** The parameters of the oscillatory fraction of $\Delta_{even}$ displayed in the figure 5.48 deduced by fitting the data with a model accounting for three oscillatory damped motions (extension of eq. 5.8).

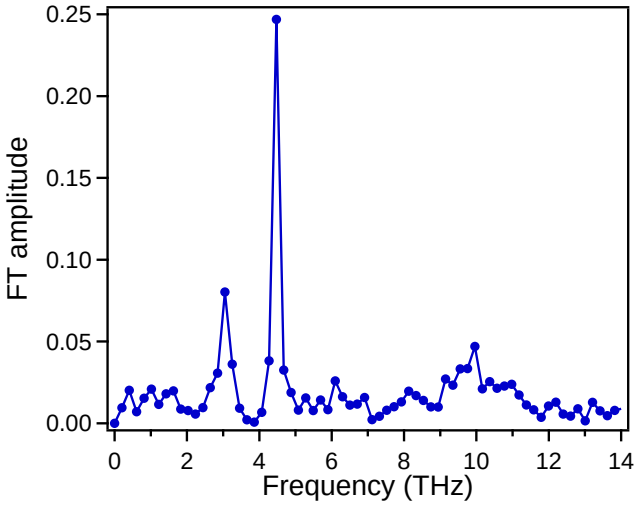


**Figure 5.49:** Fourier transformation of the oscillatory signal displayed in figure 5.48. Beside the 3 THz mode that is measured on the flat film, for the islands film two new oscillatory modes appear at 4.5 THz and 10 THz. The latter one has a broad spectral feature which means a short lifetime in the time-domain.

cillatory signal has been performed resulting in a 2D time-frequency representation plotted in figure 5.50. The Wigner transformation is similar with the short-time Fourier transform in the sense that the time-domain signal is frequency-analyzed within an adjustable temporal window (here a Gaussian) that is sliding along the time scale. This method renders the instantaneous frequency value and its modifications in the time. Now one can distinguish very clearly (see fig. 5.50) the short lived 10 THz mode and the beating pattern having the frequency of ≈1.45 THz, that corresponds to the frequency difference between the 4.5 THz and 3 THz modes. Also the dominating oscillatory mode *i.e.* 4.5 THz, exhibits an interesting feature of increasing amplitude along the pump-probe delay with the maximum level achieved after the other two modes have decayed.

### Discussion

Again we have to mention that the above presented measurements (as well as the thickness-dependent study from preceding subsection) are in an incipient stage and more detailed investigation are required. Therefore, based on the actual experimental input, we present our actual understanding and no strong conclusions can be drawn.

As we have seen above, changing the morphology of the Gd(0001) film to 3D islands, results in the appearance of two additional frequencies, besides the 3 THz mode, in the oscillatory even SH field. The question that arises is how the changed morphology can explain the presence of these higher frequency modes. STM pictures of the Gd(0001) film after annealing above the the critical temperature, show 3D islands of (quasi)hexagonal shape (see fig. 5.46) with lateral dimensions in the range of hundreds of nm sitting on top of 1 ML gadolinium that fully covers the W(110) substrate [123, 33].

The appearance of the 3 THz mode, although with one order of magnitude smaller amplitude compared to the flat film, is attributed to the excitation of the surface coherent phonon mode on top of the 3D islands in an identical manner as for the layer-by-layer films. This interpretation is based on the well-developed surface state present at the islands surface that resembles the same characteristics as for the flat film [33]. Also the

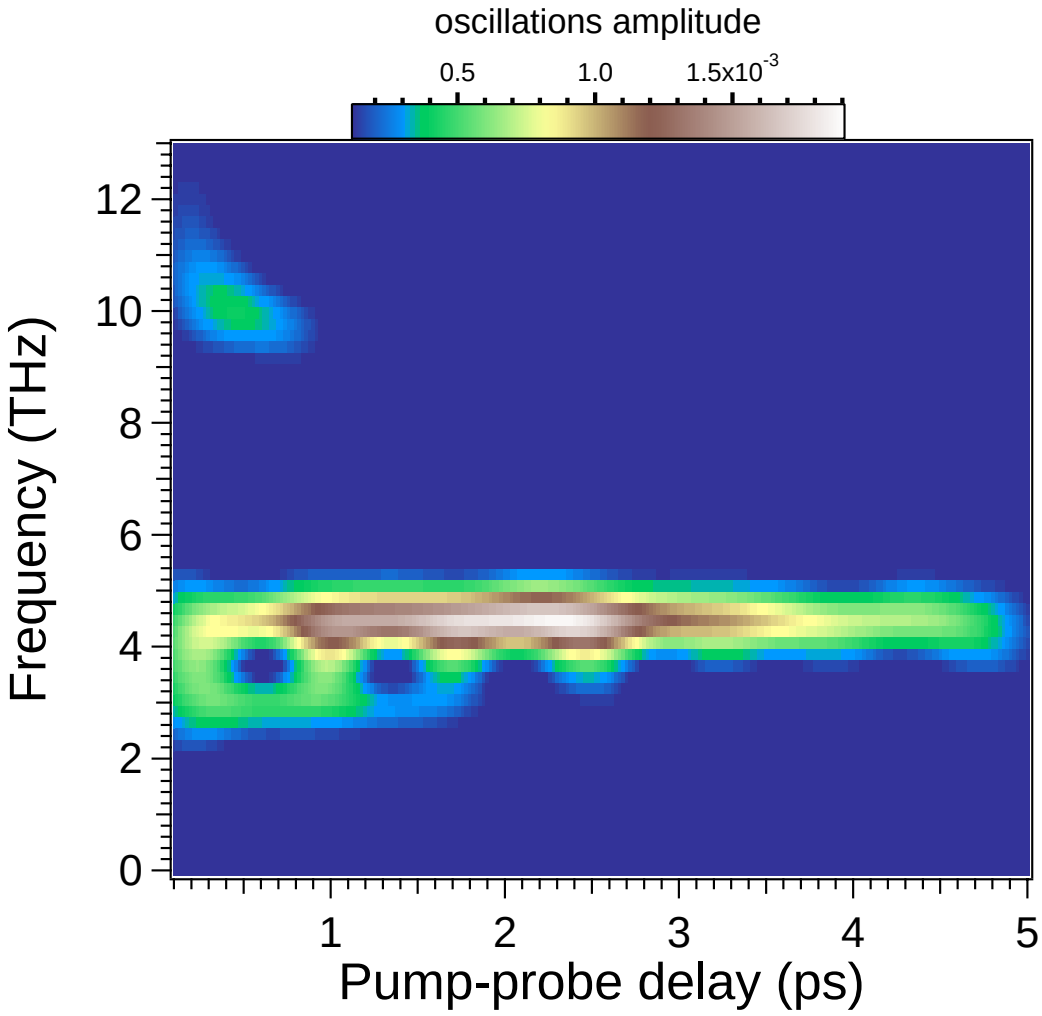


**Figure 5.50:** Wigner transformation of the oscillatory $\Delta_{even}$ signal (see fig. 5.48) measured on the Gd(0001) islands film. The short lived mode at 10 THz and the beating pattern at 1.45 THz are well discernable. Also a gradual increase of the amplitude of the 4.5 THz mode along pump-probe delay is observed.

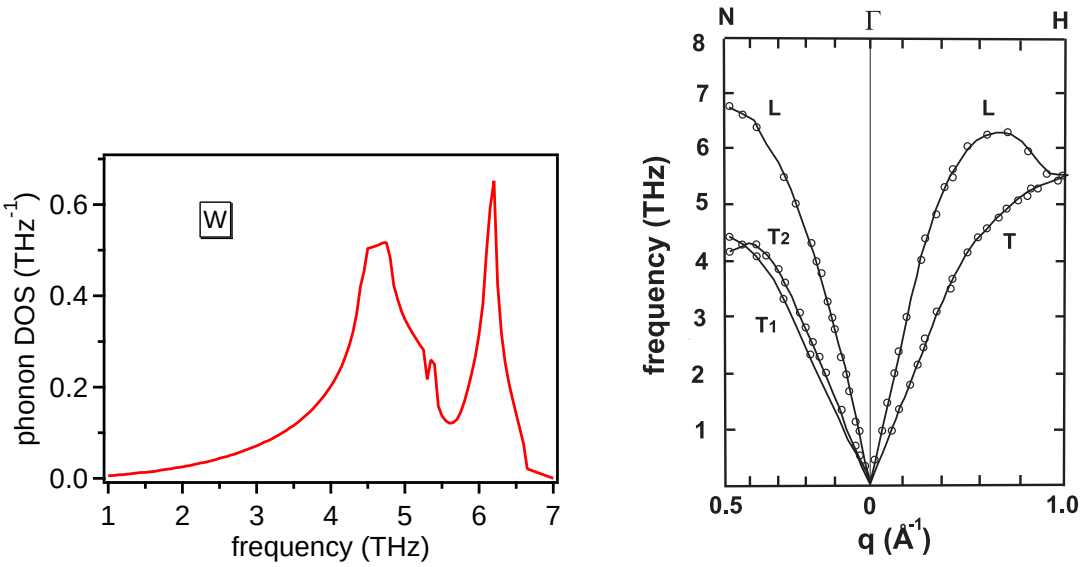


**Figure 5.51:** On the left the phonon density of states for tungsten at room temperature obtained by fitting the measured [163, 164] phonon dispersion curves, displayed on the right, with a third nearest-neighbor Born-von Karman model [165]. L and T stand for the transversal and longitudinal phonon branches, respectively, while $T_1$ and $T_2$ denote two transversal phonon modes that are almost degenerate and cross at $q$=0.45 phonon wavevector [163].

islands size can sustain collective lattice motion without producing the confinement of the phonon mode that would change its frequency. The lower amplitude of the phonon mode might originate from the increased roughness present on top of the Gd islands and thus an enhanced coherent phonon-defect scattering can take place. The presence of the coherent phonon mode should be accompanied by a coherent spin excitation (see section 5.3), but no oscillatory pattern could be resolved in the transient $\Delta_{odd}$. This is most likely due to the reduced excitation probability of the coupled quasiparticle (one order lower amplitude of the phonon mode) and due to the relatively low signal to noise ratio of the odd SH field (see fig. 5.47).

One possible explanation of the 4.5 THz mode is related with the presence of the above mentioned gadolinium monolayer among the 3D islands. One can suggest that the Gd atoms forming the single monolayer situated among the islands are vibrationally excited that results in a coherent vibration of the Gd-W bond. There are a few experimental observations that point to this interpretation. First of all, based on the surface/interface sensitivity of the SHG process, this oscillatory mode should be constrained to spatial regions where the inversion symmetry is broken. For the 5 ML Gd(0001) film (the lowest investigated thickness in the present work) prepared in a layer-by-layer growth mode we measure the oscillatory feature at 3 THz but no other modes are observed (see fig. 5.41). Investigating the bare W(110) substrate with time-resolved SHG no oscillatory feature could be observed. Moreover, the SHG measurement geometry is p-P (p-polarized input fundamental and output second-harmonic, respectively), which means that the infrared-active vibrational modes can be excited and detected with the dipole moments oriented

along the $x$ and $z$ axes (see figure 3.4), where $z$ is normal to the surface.

Inspecting the phonon density of states for tungsten, displayed in the figure 5.51, we notice the presence of two peaks concentrated around 4.5 THz and 6 THz in the phonon DOS spectrum. The pronounced peaks in the phonon DOS correspond to the measured [163, 164] phonon frequencies at N point in the tungsten Brillouin zone with 4.40(5) THz frequency for a transversal phonon and 6.75(1) THz frequency for the longitudinal branch. As noticed, the frequency of the transversal mode exhibits a very good agreement with the measured frequency of the oscillatory $\Delta_{even}$ of 4.5 THz. This intriguing observation give rise to several questions. How a transversal *bulk* phonon mode that belongs to tungsten can explain the oscillatory feature measured on Gd(0001)/W(110) system by a *surface sensitive* technique? And why the 4.5 THz mode could not be detected on the bare tungsten, if it has a surface character ? Moreover, why a phonon mode that is at edge of the Brillouin zone q=0.5 $Å^{-1}$ can be measured since with optical techniques is well known that only phonon modes with q≈0 can be detected? All these questions are to be investigated in detail by more systematic studies that beside time-resolved SHG should involve also surface sensitive techniques like Auger spectroscopy and/or surface imaging like STM. Regarding the origin of the short lived 10 THz mode is, as well as the 4.5 THz mode, for the moment an open question that requires further studies.

As an outlook to future work regarding these interesting higher frequency phonon modes observed for the modified Gd(0001) film morphology, polarization dependent measurements *i.e.* for both pump and probe beams, are necessary in order to investigate the excitation mechanism and the symmetry of the coherent phonon motion. Also the bare substrate should be subject to a polarization-dependent study in order to check for a potential tungsten surface mode. An important verification of the above proposed model for the 4.5 THz mode would be the preparation [166] and investigation of a single monolayer of Gd on the W(110) substrate.

### 5.6.3 Conclusions

First results regarding the effect of the film thickness and the changed morphology on the electron, lattice and spin dynamics of the Gd(0001) system, have been presented. Varying the film thickness between 15Å and 200Å the frequency of the coherent phonon-magnon mode remains unchanged at a value of ≈ 2.9 THz, which emphasizes the surface character of the coherent mode. An increased amplitude and decay time of the coherent phonon is observed by increasing the film thickness up to 100Å followed by a levelling to a constant value. Two possibilities have been discussed: the scattering of the phonon mode with defects produced by the Gd-W lattice mismatch induced strain and the destructive interference between surface and interface contributions to the SHG response. For the 50Å film thickness a total loss of spin polarization is encountered at early delay time followed by a rapid relaxation within 1.5 ps to a constant level. The origin of this interesting observation is unclear for the moment and necessitates further investigations. Upon changing the morphology of the smooth Gd(0001) films to 3D islands by annealing to higher temperatures, two higher frequency modes at 4.5 THz and 10 THz have been detected in the oscillatory part of $\Delta_{even}$. Simultaneously no oscillatory feature in the transient odd SH field could be resolved, presumably due to the lower amplitude of the coherent phonon mode at 3 THz

(there is a coupled phonon-magnon mode at 3 THz) and the lower statistics of the $\Delta_{odd}$. Also there is no magnon at a frequency of 4.5 THz in the magnon dispersion curves at $\Gamma$ point (see fig. 5.20). The origin of the higher frequency modes is unclear and further studies are necessary. On a speculative level the coherent vibration of the Gd-W bond has been discussed as a potential explanation of the 4.5 THz mode.

## 5.7 Conclusions and outlook

In this chapter the laser-induced dynamics of the ferromagnetic thin films of Gd(0001)/W(110) under an UHV environment has been investigated by means of time-resolved linear optical and nonlinear magneto-optical techniques.

Before the investigation of the dynamic properties of the system, a detailed study of the static response has been performed. A major result has been obtained from the spectral dependence of the SHG yield, magnetic contrast and of the relative phase between the even and odd second-harmonic fields. Their spectral evolution give evidence for the resonance enhancement of the SHG process via the exchange-split surface state of Gd(0001).

One of the first question we have addressed is the laser-induced magnetization dynamics on Gd(0001) by measuring the time evolution of the spin polarization and the exchange-splitting of the exchange-split surface state. Upon laser excitation the spin polarization of the surface state drops to 50% of the equilibrium value within the first 100 fs after excitation. Simultaneously the exchange splitting remains constant despite of the highly excited electron population in the sample. The latter observation shows that the surface magnetization of Gd(0001) does not follow the electronic temperature as was the case for the itinerant ferromagnetic systems [84, 82]. The combined observation of a decreasing spin polarization and a constant exchange splitting, lead us to the conclusion that, in Gd(0001), on the ultrafast time scale the spin-mixing behavior prevails over the Stoner behavior. The latter conclusions helps us to identify the elementary spin-scattering mechanism responsible for the optically-induced magnetization reduction in Gd(0001) namely the spin-flip scattering of hot electrons among spin-mixed states. In order to fulfill the angular momentum conservation the spin-flip events are accompanied by emission/absorption of magnons that involve the $5d$ magnetic moments and presumably also the $4f$ moments. The proposed demagnetization mechanism is particularly efficient in the case of Gd due to the strong electron-magnon coupling. The magnetization is recovered on a longer time-scale with a time constant of $\approx 150$ ps, that has been ascribed to the effect of spin-lattice interaction.

In this context, a useful check of the suggested demagnetization model can be made by employing photon energies that can excite and probe the $4f$ electrons, that have a binding energy around -9 eV. As an example are the UV and XUV light sources provided by free-electron laser or the high-harmonics generated in the rare gas cells. Also a time-resolved x-ray circular magnetic dichroism (XMCD) experiment would provide information about the dynamics of the orbital ($5d$) and spin magnetic ($4f$) moments. Another issue that should be investigated is whether the observed ultrafast demagnetization is surface specific or it evolves also in the bulk of the ferromagnetic Gd(0001). For this purpose a time-resolved MOKE experiment would help to settle this issue.

The next investigated subject has been the new and exciting phenomenon of coupled coherent phonon and magnon on the Gd(0001) surface, that evolves at a frequency of 2.9 THz. The excitation of this coupled quasiparticle is attributed to the asymmetric excitation of the surface state components which results in an ultrafast transient charge redistribution at the surface that sets the surface ions in an oscillatory motion. The lattice vibration modulate the exchange interaction strength $J$ between nearest neighbors and consequently the magnetic moments oscillate at the same frequency as the lattice. The observed coherent phonon-magnon mode on the Gd(0001) surface represents a novel phonon-magnon interaction that relies not on the spin-orbit coupling (it is very weak in Gd) but on the dynamical variation of the exchange interaction. The proposed excitation mechanism of the phonon-magnon mode has been verified by measuring the binding energy of the occupied surface state that oscillates with the same frequency as the coupled quasiparticle. As a remark, the present study of the coherent optical phonon encountered on the metal surface of Gd(0001) represents the first time measurements of a coherent optical lattice mode on a metal.

Further insight in the physics of the coupled phonon-magnon mode has been acquired by studying its dependence on the laser wavelength and the temperature of the system. Upon changing the laser photon energy between 1.48 eV and 1.68 eV, we assist at a competition between the electron and coherent lattice dynamics that is ascribed to the relative weight of the optical transitions via the surface state components. These measurements confirm and emphasize the central role played by the exchange-split surface state in the excitation of the coherent-phonon mode. The temperature dependent study shows that the excitation probability of the coupled mode depends on the exchange splitting of the surface state. The major decay channels of the coupled coherent phonon-magnon mode have been identified as the scattering with electrons and with the thermal phonons (anharmonic decay). Decreasing of the total scattering rate of the coherent phonon starting with 200 K remains an open question that requires further studies. As potential candidate in explaining this behavior the decoupling of the coherent magnon at elevated temperatures has been discussed.

As an additional check of the surface character of the coherent mode we have performed a thickness dependent study and the effect of a changed film morphology has been investigated. Down to 5 ML of Gd(0001) film thickness the coherent oscillations are resolvable with no change in the oscillatory frequency, which confirms the surface localization of the coherent phonon mode. Modifying the morphology of the smooth film to three-dimensional islands on top of 1 ML of Gd(0001), we notice the presence of two additional oscillatory modes at a frequency of 4.5 THz and 10 THz. The former one is tentatively assigned to the Gd-W bond vibration and the latter one is of an unclear origin. Further measurements are necessary in order to clarify the origin of the higher frequency modes, that should be accompanied by STM measurements performed on a film prepared in identical conditions, which would give exact information about the morphology of the investigated film.